



Volume 4

Issue 2

ISSN 2949-0561 (Online)

Electrochemical Materials and Technologies



Ural Federal
University

named after the first President
of Russia B.N. Yeltsin



Institute
of High Temperature
Electrochemistry

of Ural Branch
of Russian Academy of Science



Electrochemical Materials and Technologies

eISSN: 2949-0561, <http://elmattech.ru/>

Peer reviewed open access journal

Distributed for free

Established in 2022/Published four times per year

2025, Volume 4, Issue 2

This issue is published on 27/06/2025

Founded and published by Ural Federal University and Institute of High Temperature Electrochemistry UB RAS

19 Mira St., Yekaterinburg, 620002, Russia

20 Akademicheskaya St., Yekaterinburg, 620990, Russia

Editorial Board

Editor-in-Chief

Dr. Denis A. Osinkin, Institute of High Temperature Electrochemistry UB RAS; Ural Federal University, Yekaterinburg, Russia

Associate Editor

Ph.D. Oksana R. Rakhmanova, Institute of High Temperature Electrochemistry UB RAS; Ural Federal University, Yekaterinburg, Russia

Editors

Ph.D. Elena G. Kalinina, Institute of metal physics UB RAS, Russia

Ph.D. Vadim I. Popkov, Ioffe Institute, Saint Petersburg, Russia

Ph.D. Nikolay V. Lyskov, Federal Research Center for Problems of Chemical Physics and Medical Chemistry, Chernogolovka, Russia

Ph.D. Daniel A. Macedo, Federal University of Paraiba, João Pessoa, PB, Brazil

Ph.D. Vladislav A. Kolotygin, CIC EnergiGUNE, Vitoria-Gasteiz, Spain

Ph.D. Muhammad Bilal Hanif, Comenius University in Bratislava, Slovakia

D.Sc. Prof. Vladislav A. Sadykov, Boreskov Institute of Catalysis, Novosibirsk, Russia

D.Sc. Prof. Irina V. Piir, Institute of Chemistry Komi SC, Syktyvkar, Russia

D.Sc. Prof. Julia A. Baimova, Institute for Metals Superplasticity Problems, Ufa, Russia

D.Sc. Prof. Yalan Liu, Institute of High Energy Physics, Chinese Academy of Sciences, Beijing, China

D.Sc. Prof. Panagiotis E. Tsiakaras, University of Thessaly, Volos, Greece

Ph.D. Prof. Sudip Ghosh, Indian Institute of Engineering Science & Technology, Shibpur, Howrah, India

D.Sc. Prof. Liu Yang, School of Materials Science and Engineering, Henan Normal University, Xinxiang, China

Copyeditor

Ms. Anna V. Khodimchuk, Institute of High Temperature Electrochemistry UB RAS

Technical Editor

Ph.D. Ekaterina P. Antonova, Institute of High Temperature Electrochemistry, Ekaterinburg, Russian Federation

Scientific Illustrator

Ph.D. Kseniya A. Abramova, Institute of High Temperature Electrochemistry UB RAS

Сетевое издание «Electrochemical Materials and Technologies». Распространяется бесплатно.

Свидетельство о регистрации СМИ: Эл № ФС 77-84010 от 30.09.2022 г.

Соучредители: ФГАОУ ВО Уральский федеральный университет имени первого Президента России Б.Н. Ельцина, ФГБУН Институт высокотемпературной электрохимии Уральского отделения Российской академии наук

Адрес редакции: 620990, Свердловская обл., г. Екатеринбург, ул. Академическая, стр. 20, корп. М., к. 205, elmattech@urfu.ru

Дата выхода номера: 27.06.2025

Table of Contents

20254051 / ARTICLE

Natalia Tarasova, Ekaterina Abakumova, Tamara Kuznetsova

Oxygen-ionic transport in the novel Ca-doped complex oxides based on BaLaInO_4

20254052 / ARTICLE

Dmitry Zakiryanov

Structure and dynamics of molten calcium chloride: *ab initio* simulations

20254053 / ARTICLE

Vladislav Sadykov, Ekaterina Sadovskaya, Nikita Ereemeev, Elena Pikalova

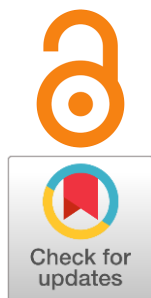
Details on oxygen surface exchange mechanism over $\text{Pr}_{1.6}\text{Ca}_{0.4}\text{Ni}_{1-y}\text{Cu}_y\text{O}_{4+\delta}$ solid oxide fuel cell/electrolyzer air electrodes

20254054 / FOCUS REVIEW

Elena Pikalova

Progress in infiltration technology applied to air electrodes with proton-conducting electrolyte backbones

Oxygen-ionic transport in the novel Ca-doped complex oxides based on BaLaInO₄

Natalia Tarasova^{a*}, Ekaterina Abakumova^a, Tamara Kuznetsova^aReceived: 11 March 2025
Accepted: 3 April 2025
Published online: 10 April 2025DOI: [10.15826/elmattech.2025.4.051](https://doi.org/10.15826/elmattech.2025.4.051)

Electrochemical energy sources are part of the new energy sector due to their high efficiency and cost effectiveness. Solid oxide fuel cells are an excellent example of these devices. They are made from a variety of materials, including ceramics. Oxygen ion conductive ceramics can be used as the electrolyte material. In this work, the isovalent doping of the barium sublattice by calcium ions has been carried out for the first time. The effect of doping on the structure and electrical conductivity was investigated. Doping leads to an increase in conductivity values compared to the matrix composition. The greatest increase in conductivity was observed for the composition with low dopant concentration.

keywords: BaLaInO₄, layered perovskite, Ruddlesden-Popper structure, oxygen-ionic conductivity

© 2025, the Authors. This article is published in open access under the terms and conditions of the Creative Commons Attribution (CC BY) license (<http://creativecommons.org/licenses/by/4.0/>).

1. Introduction

One of the most important problems of the 21st century is the threat of global warming due to the large amount of CO₂ emissions from energy production from fossil fuels [1–4]. The development of environmentally friendly and resource-saving hydrogen energy can help solve the environmental problem. The environmentally friendly energy sources are fuel cells, which are an electrochemical current source that works by converting the energy of chemical reactions of the fuel into electrical energy. This is very promising both from the point of view of the availability of energy resources and from the point of view of environmental protection [5–9].

There are several types of fuel cells used in hydrogen energy. Fuel cells, for example, can be classified according to their operating principle and the type of electrolyte material used. There are fuel cells with a polymer-electrolytic membrane (PEMFC), solid oxide fuel cells

(SOFC), alkaline fuel cells (AFC), phosphoric acid fuel cells (PAFC) and fuel cells with molten carbonate (MCFC) [10–11]. Solid-state electrolytes (SSE) are a promising class of energetic materials in which specific groups of ions can be induced to diffuse through a crystalline matrix. Solid electrolytes have a number of advantages, including non-flammability and high thermal and chemical stability. SE form the basis for clean energy conversion and storage technologies such as fuel cells, electrocatalysts, and solid-state batteries. Therefore, optimizing their ion transport properties is crucial for energy and sustainable development.

As a result, SOFCs have a number of advantages over other types of fuel cells, including 60–80 % higher conversion efficiency, longer lifetime, etc. [12]. At the same time, when using SOFC, fewer pollutants are released into the environment, and they do not require catalysis by precious metals. SOFCs can operate on various types of fuel, such as hydrocarbons, coal gas, biomass, hydrogen, and synthesis gas [13]. While SOFCs are independent of pure hydrogen supplies, since hydrocarbons can be fed into the fuel cell and converted

^a: Institute of High-Temperature Electrochemistry UB RAS, Ekaterinburg 620066, Russia

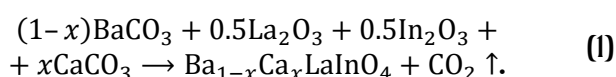
* Corresponding author: Natalia.Tarasova@ihte.ru

into a hydrogen-rich stream through internal thermochemical processes [13, 14]. The study of solid oxide fuel cells requires the synthesis and study of new materials with oxygen-ion and proton properties. Complex BaLaInO₄-based oxides with high ionic conductivity values can be used as electrolytes in SOFCs.

Materials with a perovskite structure characterized by the general formula ABO_3 receive a significant share of attention for use as SOFC conductors [15, 16]. However, new classes of ionic conductors with a perovskite-related structure, such as perovskite-BaLaInO₄ layered materials [17–20], are attracting increasing attention. In contrast to classical perovskites, layered RP-structures have a space between the layers. Due to this structural characteristic, layered perovskites need to be studied more intensively. The compositions Ba_{1-x}Ca_xLaInO₄ ($x = 0.05, 0.1, 0.15$) were obtained. The effect of doping on the structure and electrical conductivity was investigated.

2. Experimental

The solid solution Ba_{1-x}Ca_xLaInO₄ ($x = 0, 0.05, 0.1$ and 0.15) was obtained by thoroughly grinding La₂O₃, In₂O₃, BaCO₃ and CaCO₃ in an agate mortar according to the stoichiometric coefficients. The weighed portions of pre-dried oxides and carbonates powders were taken on a Sartorius ACCULAB ALC-210d4 analytical scale (Sartorius Weighing Technology GmbH, Germany). The powder blends were annealed in a Nabertherm furnace after grinding. The initial annealing temperature was set at 800 °C. The total annealing range was 800–1300 °C. The chemical reaction according to the stoichiometric coefficients led to the solid solution Ba_{1-x}Ca_xLaInO₄ ($x = 0, 0.05, 0.1$ and 0.15):



The phase composition was controlled by X-ray phase analysis using a Bruker Advance D8 diffractometer (Bruker, Billerica, MA, USA). The parameters for the X-ray were a step of 0.01 ° and a speed of 0.5 °/min. XRD measurements were carried out at a controlled room temperature. In order to investigate the new solid solution Ba_{1-x}Ca_xLaInO₄, a structure refinement was carried out by means of the Rietveld method. The Rietveld method was carried out in the FullProf program. Calculation of bond lengths, analysis and visualization of the structure are performed in the VESTA program.

The morphology of the solid-phase solution Ba_{1-x}Ca_xLaInO₄ ($x = 0.05, 0.1, 0.15$) on the sintered tablets was studied using a Vega 3 Tescan scanning electron

microscope (SEM) coupled with an energy-dispersive X-ray spectroscopy (EDS) system.

The conductivity of the compositions Ba_{1-x}Ca_xLaInO₄ ($x = 0, 0.05, 0.1$ and 0.15) was measured using a Z-1000P impedance-meter (Elins, Russia). Frequencies were in the range of 100 Hz to 1 MHz. Bulk resistance was calculated from impedance spectra using Zview software fitting (Scribner Associates Inc., Southern Pines, NC). For this measurement, a 10 mm diameter tablet was sintered at a temperature of 1300 °C for 24 hours. Platinum paste was used as electrodes and applied in a thin layer on the tablet. The platinum electrodes were annealed at 1000 °C for 3 hours. The investigations were carried out from 1000 to 200 °C with a cooling rate of 1 °/min under dry air or dry Ar. The dry gas (air or Ar) was prepared by circulating the gas through P₂O₅ ($p_{H_2O} = 3.5 \cdot 10^{-5}$ atm).

3. Results and discussions

Phase attestation of solid solution Ba_{1-x}Ca_xLaInO₄ carried out using the XRD method. It was shown that the compositions at dopant concentrations $0 \leq x \leq 0.15$ were single phase and belonged to the space group $I4/mmm$ (tetragonal symmetry). XRD patterns of Ba_{0.9}Ca_{0.1}LaInO₄ composition are presented in Figure 1. In contrast, the matrix composition BaLaInO₄ has orthorhombic symmetry ($Pbca$ space group). It is obvious that the introduction of the dopant led to a change in the local structure and an increase in the symmetry. However, in order to gain a more accurate understanding of the effect of doping on the structure, a structural analysis of the samples was carried out and the bond lengths were determined. As can be seen from Figure 2, the Ba_{0.9}Ca_{0.1}LaInO₄ sintered sample is a densely packed round agglomerates of 20–40-micron particles. The lattice parameters and unit cell volume for the compositions are presented in Table 1. Table 2 shows the bond length values for the compositions. R -factors for the new solid solution Ba_{1-x}Ca_xLaInO₄ are shown in Table 3. As can be seen, doping with smaller ionic radii ($r_{Ba^{2+}} = 1.47 \text{ \AA}$; $r_{Ca^{2+}} = 1.18 \text{ \AA}$ [21]) leads to the decrease in the lattice parameters. However, the redistribution of bond lengths occurs in a more complex manner. The average bond length $\langle Ba/Ca/La-O \rangle$ decreases with the introduction of the dopant and continues to decrease as its concentration increases. The average bond length $\langle In-O \rangle$ also decreases with the introduction of calcium, but an increase in calcium concentration leads to an increase in this bond length. It is obvious that such a redistribution of bond lengths ultimately leads to a change in the tilt angle of the polyhedra and a general increase in the symmetry of the structure. The possible reason for these changes is the appearance of different

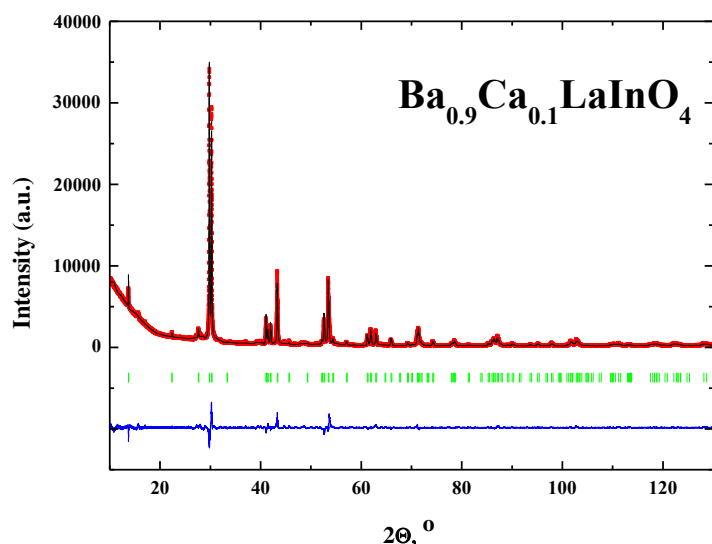


Figure 1 Refinement of the XRD for the composition $\text{Ba}_{0.9}\text{Ca}_{0.1}\text{LaInO}_4$. **Figure 2** SEM image of the $\text{Ba}_{0.9}\text{Ca}_{0.1}\text{LaInO}_4$ ceramic sample.

Table 1 – The lattice parameters and unit cell volume for obtained compositions.

Lattice parameters	BaLaInO_4	$\text{Ba}_{0.95}\text{Ca}_{0.05}\text{LaInO}_4$	$\text{Ba}_{0.9}\text{Ca}_{0.1}\text{LaInO}_4$	$\text{Ba}_{0.85}\text{Ca}_{0.15}\text{LaInO}_4$
a , Å	12.932(3)	4.176(6)	4.175(7)	4.174(6)
b , Å	5.906(0)	4.176(6)	4.175(7)	4.174(6)
c , Å	5.894(2)	12.925(3)	12.907(7)	12.889(1)
V , Å ³	450.19(5)	225.470(9)	225.07(4)	224.63(1)

Table 2 – The bond lengths values for obtained compositions.

Bond lengths (Å)	BaLaInO_4	$\text{Ba}_{0.95}\text{Ca}_{0.05}\text{LaInO}_4$	$\text{Ba}_{0.9}\text{Ca}_{0.1}\text{LaInO}_4$	$\text{Ba}_{0.85}\text{Ca}_{0.15}\text{LaInO}_4$
<Ba/Ca/La–O1>	2.815(2)	2.800(1)	2.796(3)	2.796(8)
<Ba/Ca/La–O2>	2.864(0)	2.433(2)	2.383(4)	2.303(4)
<Ba/Ca/La–O>	2.839(6)	2.616(6)	2.589(8)	2.550(1)
<In–O1>	2.141(3)	2.088(3)	2.087(9)	2.087(3)
<In–O2>	2.180(2)	2.164(1)	2.210(3)	2.279(6)
<In–O>	2.162(2)	2.126(2)	2.149(1)	2.183(4)

Table 3 – R -factors for the new solid solution $\text{Ba}_{1-x}\text{Ca}_x\text{LaInO}_4$.

R -factors	$\text{Ba}_{0.95}\text{Ca}_{0.05}\text{LaInO}_4$	$\text{Ba}_{0.9}\text{Ca}_{0.1}\text{LaInO}_4$	$\text{Ba}_{0.85}\text{Ca}_{0.15}\text{LaInO}_4$
Chi2	2.13	2.96	2.70
R_p	4.3	5.0	4.6
R_{wp}	3.4	3.7	3.0
R_{exp}	4.02	4.70	4.04
Chi2 (Bragg contrib.)	2.122	2.731	2.67
Bragg R -factor	2.031	2.64	2.91

natural ions in the cationic sublattice ($\text{Ca}^{2+} \rightarrow \text{Ba}^{2+}$).

The electrical conductivity values were obtained using the impedance spectroscopy method in the atmospheres with controlled humidity ($p\text{H}_2\text{O}$) and oxygen partial pressure ($p\text{O}_2$). The Nyquist plots are shown in Figures 3 for the composition $\text{Ba}_{0.9}\text{Ca}_{0.1}\text{LaInO}_4$ as an example of typical plots. All obtained Nyquist plots contain two semicircles (Figure 3 a). The small semicircle

starting from zero coordinates (high-frequency semicircle) corresponds to the resistivity of the grain volume of polycrystalline sample.

This is proven by the small capacitance value $\sim 10^{-12}$ F/cm. The large semicircle (low frequency semicircle) corresponds to the resistivity of the grain boundaries with a capacitance value $\sim 10^{-9}$ F/cm. The conductivities were calculated from the resistivity values

taken at the intersection of the high-frequency semicircle with the abscissa axis. The influence of temperature and oxygen partial pressure on the Nyquist plot is shown in Figures 3 b and 3 c respectively. The temperature dependencies of the conductivity obtained under dry air ($p_{O_2} = 0.21$ atm) and dry Ar ($p_{O_2} \sim 10^{-5}$ atm) are shown in Figure 4. As can be seen, the introduction of calcium ions into the barium sublattice leads to an increase in the conductivity values compared to the matrix composition.

The comparison of the conductivity values obtained under dry air and dry Ar conditions (Figure 5) shows the changes in the proportion of oxygen-ionic transport with varying temperature and calcium concentration. The conductivity nature under dry Ar (i.e. at lower oxygen partial pressure) is predominantly oxygen-ionic. The proportion of oxygen transport (oxygen-ion transport numbers) is defined as the ratio of oxygen-ion conductivity to total conductivity:

$$t_{O^{2-}} = \frac{\sigma^{Ar}}{\sigma^{air}} \quad (2)$$

At the high temperature (900 °C), the oxygen ionic transport numbers are the same for all Ca-doped

compositions and are ~ 40 %. As the temperature decreases, the values of the oxygen ionic transport numbers change. They increase up to ~ 60 % for the composition with $x = 0.05$ and decrease up to ~ 20 % for the compositions with $x = 0.10$ and 0.15. The oxygen ionic transport numbers are ~ 20 % over the whole temperature range.

The fact that the values of the oxygen ionic transport coefficients change with the variation of the calcium content is very interesting. Calcium doping of the barium sublattice does not lead to the formation of oxygen defects in the anionic sublattice. Instead, fragments Ba–O–Ca (at "low" doping concentrations) and Ca–O–Ca (at "high" doping concentrations) appear in the structure at the sites of the matrix fragment Ba–O–Ba.

It can be assumed that the transport of oxygen is facilitated in the case of its bonding with atoms of different nature Ba–O–Ca, which leads to an increase in the ionic component of the conductivity (case of composition with $x = 0.05$) due to the increase in the proportion of mobile oxygen ions. An increase in calcium concentration can lead to the appearance of Ca–O–Ca fragments in the structure and to a decrease in oxygen transport.

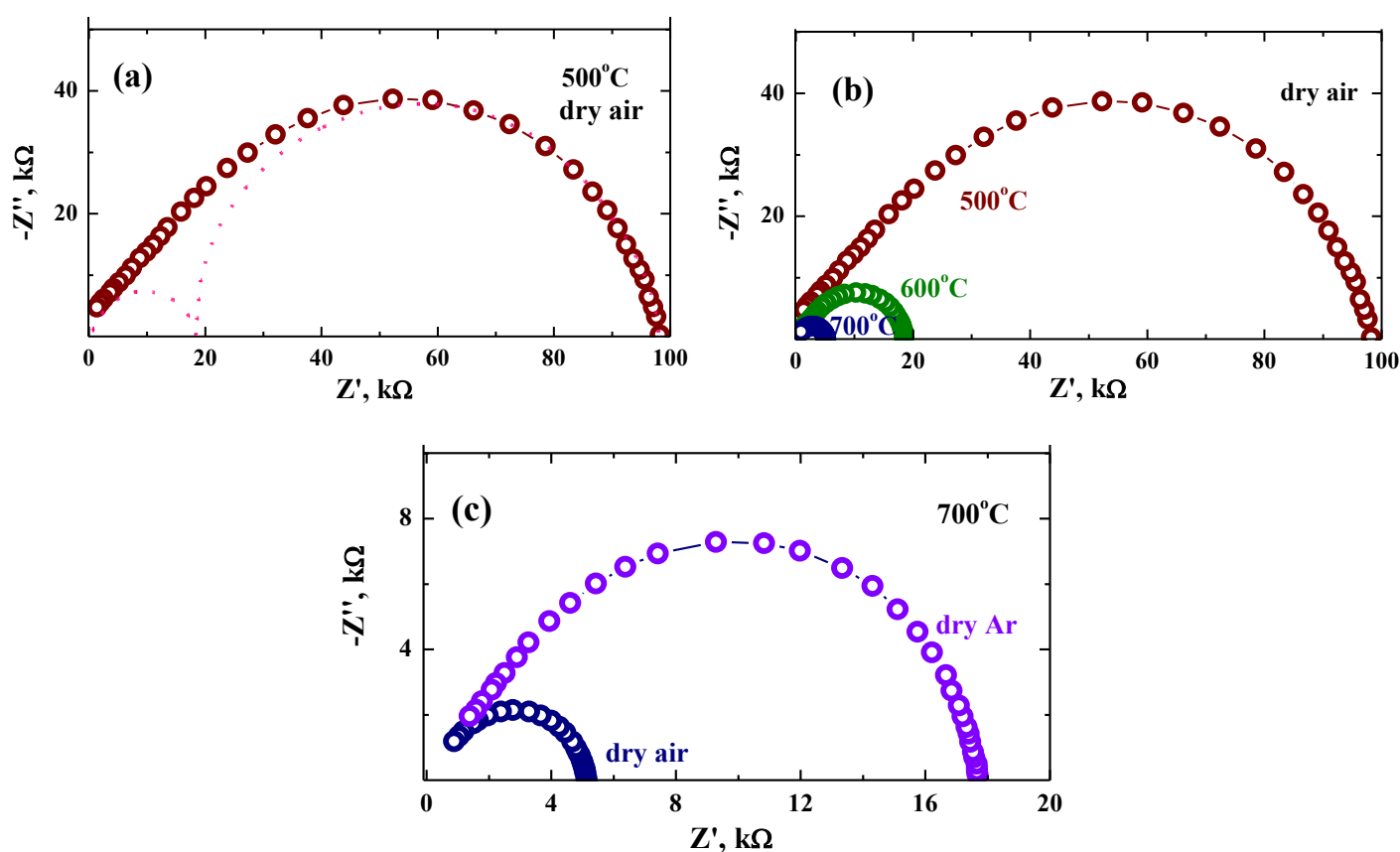


Figure 3 The Nyquist plots for the composition $Ba_{0.9}Ca_{0.1}LaInO_4$ obtained at 500 °C in dry air (a), at 500, 600 and 700 °C in dry air (b) and at 700 °C in dry air and dry Ar (c).

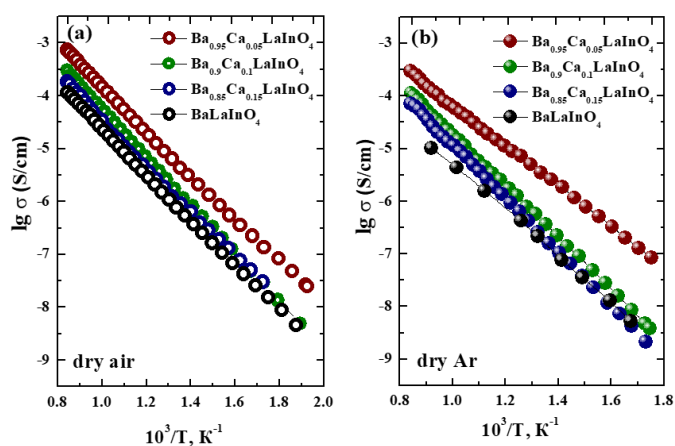


Figure 4 The temperature dependencies of conductivity for investigated compositions obtained at dry air (a) and dry Ar (b).

These considerations can also explain the concentration dependencies of the oxygen-ionic conductivity (Figure 6 a). As can be seen, calcium doping leads to an increase in conductivity values with respect to the matrix composition. At the same time, the composition with the lowest doping concentration ($x = 0.05$) has the highest conductivity values. Further increase in calcium concentration leads to a decrease in conductivity values. In other words, the "high" calcium concentration (the appearance of Ca–O–Ca fragments) is one of the possible reasons for the decrease in conductivity. However, the concentration dependence of the total conductivity, which is the sum of the ionic and electronic components of the conductivity, has the same shape (Figure 6 b).

Accordingly, increasing the dopant concentration leads to a decrease not only in the oxygen ionic conductivity but also in the total conductivity. Calcium doping is accompanied by a decrease in unit cell parameters and unit cell volume, i.e., a decrease in migration volume. Not only does the proportion of mobile oxygen ions decrease, but also the mobility of the oxygen ions as a whole also decreases.

Therefore, calcium doping of barium sublattice of layered perovskite $BaLaInO_4$ up to ~ 0.9 order of magnitude for total conductivity and up to ~ 1.5 orders of magnitude for oxygen-ionic conductivity (at low temperatures for $Ba_{0.9}Ca_{0.1}LaInO_4$ composition). The introduction of higher calcium concentrations ($x > 0.05$) leads to a decrease in both total and oxygen-ion conductivity. Figure 7 shows a comparison of Ca^{2+} doped compounds by isovalent substitution and acceptor substitution relative to undoped $BaLaInO_4$. It is clear that isovalent doping increases conductivity relative to undoped, but acceptor doping increases conductivity more significantly, as can be seen from Figure 7.

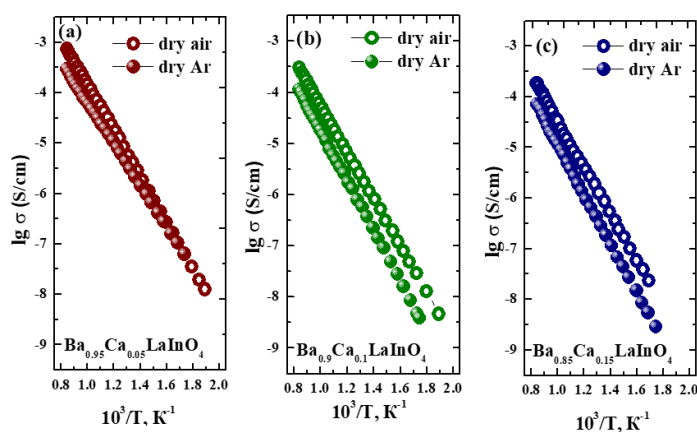


Figure 5 The temperature dependencies of conductivity for compositions $Ba_{0.95}Ca_{0.05}LaInO_4$ (a), $Ba_{0.9}Ca_{0.1}LaInO_4$ (b), $Ba_{0.85}Ca_{0.15}LaInO_4$ (c).

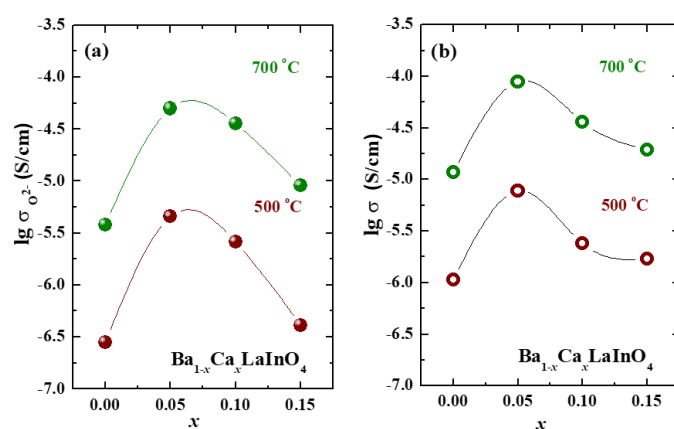


Figure 6 Concentration dependencies of oxygen-ionic (a) and total (b) conductivities.

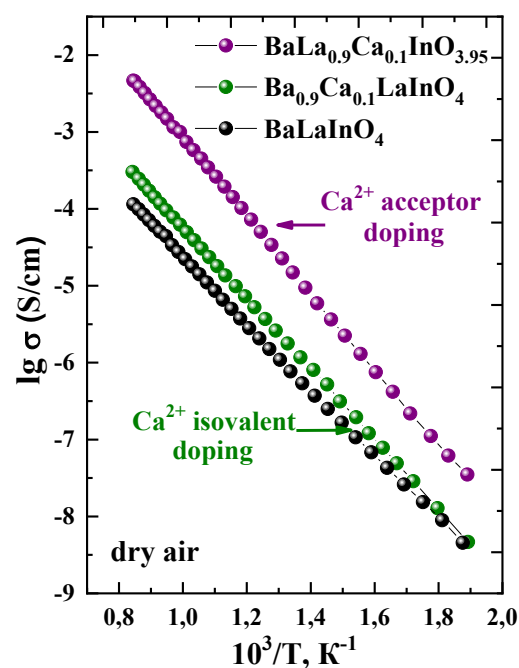
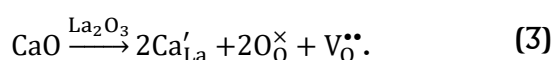


Figure 7 Comparison of compounds doped with Ca^{2+} by means of isovalent doping and acceptor doping [22] is relatively undoped $BaLaInO_4$.

From the point of view of the principles of solid state chemistry, point defects do not occur with isovalent doping. While acceptor doping creates oxygen vacancies and changes the oxygen non-stoichiometry. The quasi-chemical reaction of this process is described by Equation 3. A significant increase in conductivity due to acceptor doping can be explained by the appearance of oxygen vacancies in the structure and an increase in interlayer space, as mentioned [22]. At the same time, for isovalent doping, the increase in conductivity is only due to an increase in interlayer space, which is confirmed by the calculation of bond lengths.



4. Conclusions

The calcium-doped layered perovskites $\text{Ba}_{1-x}\text{Ca}_x\text{LaInO}_4$ ($x = 0.05, 0.1, 0.15$) were obtained for the first time. The effect of doping on the structure and electrical conductivity was investigated. Doping causes the symmetry change from *Pbca* (for matrix composition) to *I4/mmm* (for doped composition). The average bond lengths metal–oxygen decrease with the introduction of calcium. The introduction of calcium ions into barium sublattice leads to the increase in the conductivity values compared with the matrix composition. The greatest increase in conductivity (up to ~ 0.9 order of magnitude for total conductivity and up to ~ 1.5 orders of magnitude for oxygen-ionic conductivity) is observed for the composition with small dopant concentration.

Funding

This research had no external funding.

Acknowledgments

None.

Author contributions

Natalia Tarasova: Conceptualization; Funding acquisition; Methodology; Visualization; Writing – Original draft; Writing – Review & Editing.

Ekaterina Abakumova: Funding acquisition; Methodology; Visualization; Writing – Original draft.

Tamara Kuznetsova: Funding acquisition; Methodology; Visualization; Writing – Original draft.

Conflict of interest

The authors declare no conflict of interest.

Additional information

Tarasova Natalia, Orcid: [0000-0001-7800-0172](https://orcid.org/0000-0001-7800-0172);
Scopus Author ID: [37047923700](https://scopus.com/authid/detail.url?authorID=37047923700);

Abakumova Ekaterina, Orcid: [0000-0002-6102-6461](https://orcid.org/0000-0002-6102-6461);
Scopus Author ID: [57699973300](https://scopus.com/authid/detail.url?authorID=57699973300);

Kuznetsova Tamara, Orcid: [0009-0000-5062-184X](https://orcid.org/0009-0000-5062-184X);
Scopus Author ID: [57752091200](https://scopus.com/authid/detail.url?authorID=57752091200).

Institute's website: https://ihte.ru/?page_id=3106
Institute of High Temperature Electrochemistry of
the Ural Branch of the Russian Academy of Sciences,



References

- Shu DY, Deutz S, Winter BA, Baumgärtner N, The role of carbon capture and storage to achieve net-zero energy systems: trade-offs between economics and the environment, *Ren. Sust. Ener. Rev.*, **178(6396)** (2023) 113246. <https://doi.org/10.1016/j.rser.2023.113246>
- Davis SJ, Caldeira K, Matthews HD, Future CO₂ emissions and climate change from existing energy infrastructure, *Science*, **329(5997)** (2010) 1330–1333. <https://doi.org/10.1126/science.1188566>
- Tyquin E, Weeks CS, Mehta A, Newton C, Delivering an energy export transition: Impact of conflicting and competing informational contexts on public acceptance of Australia's hydrogen export industry, *Int. J. Hydrogen Energy*, **61** (2024) 226–237. <https://doi.org/10.1016/j.ijhydene.2024.02.185>
- Krause J, Yugo M, Samaras Z, Edwards S, et al., Well-to-wheels scenarios for 2050 carbon-neutral road transport in the EU, *J. Clean. Prod.*, **443** (2024) 141084. <https://doi.org/10.1016/j.jclepro.2024.141084>
- Younas M, Shafique S, Hafeez A, Javed F, et al., An overview of hydrogen production: current status, potential, and challenges, *Fuel*, **31615** (2022) 123317. <https://doi.org/10.1016/j.fuel.2022.123317>
- Singh M, Zappa D, Comini E, Solid oxide fuel cell: Decade of progress, future perspectives and challenges, *Int. J. Hydrogen Energy*, **46(54)** (2021) 27643–27674. <https://doi.org/10.1016/j.ijhydene.2021.06.020>
- Xu Q, Guo Z, Xia L, He Q, et al., A comprehensive review of solid oxide fuel cells operating on various promising alternative fuels, *Energy Conversion and Management*, **253** (2022) 115175. <https://doi.org/10.1016/j.enconman.2021.115175>
- Peng J, Huang J, Wu X, Xu Y, et al., Solid oxide fuel cell (SOFC) performance evaluation, fault diagnosis and health control: A review, *Journal of Power Sources*, **505** (2021) 230058. <https://doi.org/10.1016/j.jpowsour.2021.230058>
- Parente C, Teixeira F, Cerdeira J, 'Stakeholders' perceptions of hydrogen and reflections on energy transition governance, *Energy. Sustain. Soc.*, **14** (2024) 1–19. <https://doi.org/10.1186/s13705-023-00429-w>

10. Vansh M, Siddharth S, Mudit KB, Mohit V, Comparative study and analysis between Solid Oxide Fuel Cells (SOFC) and Proton Exchange Membrane (PEM) fuel cell – A review, *Materials today: Proceedings*, **47(10)** (2021) 2270–2275. <https://doi.org/10.1016/j.matpr.2021.04.203>

11. Norby T, Widerøe M, Glöckner R, Larring Y, Hydrogen in oxides, *Dalton Transactions*, **19** (2004) 3012–3018. <https://doi.org/10.1039/B403011G>

12. Syafkeena N, Affandi M, Osman N, Short review on global trends in SOFC scenario and future perspective, *Materials today: Proceedings*, **66(10)** (2022) 3981–3984. <https://doi.org/10.1016/j.matpr.2022.04.824>

13. Kong W, Han Zh, Lu S, Gao X, A novel interconnector design of SOFC, *Int. J. Hydrogen Energy*, **45(39)** (2020) 20329–20338. <https://doi.org/10.1016/j.ijhydene.2019.10.252>

14. Sahli Y, Moussa HB, Zitouni B, Optimization study of the produced electric power by SOFCs, *Int. J. Hydrogen Energy*, **44(39)** (2019) 22445–22454. <https://doi.org/10.1016/j.ijhydene.2018.08.162>

15. Matsuzaki K, Saito K, Ikeda Y, Nambu Y, et al., High Proton Conduction in the Octahedral Layers of Fully Hydrated Hexagonal Perovskite-Related Oxides, *J. Am. Chem. Soc.*, **146(27)** (2024) 18544–18555. <https://doi.org/10.1021/jacs.4c04325>

16. Fop S, Dawson JA, Fortes AD, Ritter C, McLaughlin AC, Hydration and ionic conduction mechanisms of hexagonal perovskite derivative, *Chemistry of Materials*, **33(12)** (2021) 4651–4660. <https://doi.org/10.1021/acs.chemmater.1c01141>

17. Tarasova N, Animitsa I, Galisheva A, Medvedev D, Layered and hexagonal perovskites as novel classes of proton-conducting solid electrolytes: A focus review, *Electrochem. Mater. Technol.*, **1** (2022) 20221004. <https://doi.org/10.15826/elmattech.2022.1.004>

18. Tarasova N, Galisheva A, Animitsa I, Korona D, et. al., Protonic transport in layered perovskites $\text{BaLa}_n\text{In}_n\text{O}_{3n+1}$ ($n = 1, 2$) with Ruddlesden-Popper structure, *Appl. Sci.*, **12(8)** (2022) 4082. <https://doi.org/10.3390/app12084082>

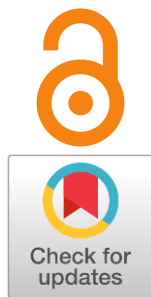
19. Tarasova N, Animitsa I, Galisheva A, Pryakhina V, Protonic transport in the new phases $\text{BaLaIn}_{0.9}\text{M}_{0.1}\text{O}_{4.05}$ ($M = \text{Ti}, \text{Zr}$) with Ruddlesden-Popper structure, *Solid State Sciences*, **101** (2020) 106121. <https://doi.org/10.1016/j.solidstatesciences.2020.106121>

20. Tarasova N, Galisheva A, Animitsa I, Anokhina I, Novel mid-temperature $\text{Y}^{3+} \rightarrow \text{In}^{3+}$ doped proton conductors based on the layered perovskite BaLaInO_4 , *Ceramics International*, **48(11)** (2022) 15677–15685. <https://doi.org/10.1016/j.ceramint.2022.02.102>

21. Shannon RD, Revised effective ionic radii and systematic studies of interatomic distances in halides and chalcogenides, *Acta Cryst. A*, **32** (1976) 751–767. <https://doi.org/10.1107/S0567739476001551>

22. Tarasova N, Galisheva A, Animitsa I, Korona D, Incorporation and conduction of protons in Ca, Sr, Ba-doped BaLaInO_4 with Ruddlesden-Popper structure, *Materials*, **12(10)** (2019) 1668–1682. <https://doi.org/10.3390/ma12101668>

Structure and dynamics of molten calcium chloride: *ab initio* simulations

Dmitry Zakiryanov^{a*}Received: 6 May 2025
Accepted: 10 June 2025
Published online: 17 June 2025DOI: [10.15826/elmattech.2025.4.052](https://doi.org/10.15826/elmattech.2025.4.052)

Structure and transport properties of CaCl_2 -based melts attract attention due to prospective applications in the field of energy storage and transport, including green technologies. Most effort was aimed at mixed binary and ternary compositions, while pure CaCl_2 melt was investigated in less detail. In this paper, molten CaCl_2 was simulated using the *ab initio* molecular dynamics approach. Due to the relatively high duration of the simulation run, both static and dynamic properties were obtained. It was found that preferential Ca coordination cases are $[\text{CaCl}_7]$ and $[\text{CaCl}_6]$. Dynamic properties including vibrational density of states and cation-anion lifetimes show that the structure of the melt does not exhibit stable units. Self-diffusion coefficients calculated from mean squared displacements are in a good agreement with available experimental data.

keywords: molten salt, local structure, calcium chloride, vibrational spectra

© 2025, the Authors. This article is published in open access under the terms and conditions of the Creative Commons Attribution (CC BY) license (<http://creativecommons.org/licenses/by/4.0/>).

1. Introduction

Melts based on calcium chloride are considered promising for green energy applications as both heat storage and heat transfer fluids [1–4]. Key features of these melts, including thermal stability, heat capacity, and thermal conductivity, meet the needs of concentrated solar power plants. Due to strict “structure → properties” causing, the local structure of CaCl_2 -based melts attracts particular attention. The molecular dynamics approach serves here as a convenient method for studying local structure in sufficient detail, avoiding experimental challenges connected with high-temperature measurements. However, the accuracy of molecular dynamic simulations strongly depends on the underlying method for the evaluation of the potential energy. Among commonly used approximations, the density functional theory (DFT) [5, 6] is one of the most reliable. In recent years, machine learning interatomic potentials

(MLIPs) [7, 8] became a versatile tool for studying both local structure and transport properties, providing a combination of *ab initio* accuracy and computational efficiency. To date, a comprehensive series of studies on CaCl_2 -MCl ($M = \text{Li}, \text{Na}, \text{K}$) was made with *ab initio* molecular dynamics (AIMD) or MLIPs for CaCl_2 -LiCl [9], CaCl_2 -NaCl [10–12], CaCl_2 -KCl [13, 14]. In [10], CaCl_2 -NaCl *ab initio* simulation run was only 2.42 ps, which resulted in a noisy radial distribution function and a large uncertainty in self-diffusion coefficients. In our opinion, the time of 2.42 ps is too short for estimation of any transport properties. Considering the local structure, Ca–Cl coordination numbers were found to be 6.27...5.96 for the temperature range of 783...1173 K. On the other hand, in [11, 12] the authors used MLIPs and obtained better statistics. In terms of Ca coordination, MLIP results concur closely with raw *ab initio*, predicting coordination numbers within the range of 6.1...5.7 and the corresponding maxima of the radial distribution function at 2.65...2.70 Å. Also, six-fold Ca pattern takes place in CaCl_2 -KCl [13] as well as in more complex mixtures with alkali chlorides [15, 16].

^a: Institute of High-Temperature Electrochemistry UB RAS, Ekaterinburg 620066, Russia

* Corresponding author: dmitryz.ihte@gmail.com

The current study is devoted to the structure and dynamics of CaCl_2 melt. Properties of a pure melt are less covered by simulation studies. In [17], Bu et al. simulated CaCl_2 using *ab initio* molecular dynamics with the PBE functional [18]. They showed that the dispersion correction hugely improves the accuracy of density predictions, although agreement with experimental data is not perfect. It is valuable that not only the average Ca–Cl coordination number was derived, but also a probability of different coordination cases as well. The authors showed that the structure exhibits the following units, from highest to lowest probability: $[\text{CaCl}_6]$, $[\text{CaCl}_7]$, $[\text{CaCl}_5]$, $[\text{CaCl}_8]$. Transport properties were not analyzed, probably because of a relatively short simulation time. Among other studies, classical molecular dynamics by Umesaki [19] reveals the Ca–Cl coordination number of 5.8 with the Ca–Cl separation of 2.70...2.76 Å. Finally, direct experimental data obtained using neutron diffraction [20] gives somewhat different values: the coordination number of 2.78 ± 0.03 and the interionic distance of 5.4 ± 0.3 .

In the present study, we deliver a more complete list of molten CaCl_2 properties by extending the duration of the *ab initio* molecular dynamics simulation. This allowed us to compute not only static properties, but comprehensive details on structure dynamics as well.

2. Methods

For the needs of our study, at least several tens of picoseconds are required to be simulated. On the one hand, the pair potential could produce reliable results once proper fitting was performed. However, the development of a pair potential model is beyond the scope of this study since a pair model is generally less accurate compared to *ab initio*, although less expensive. Despite the time demands, the density functional theory was employed. The PBE [18] functional was used. The D3 dispersion correction [21] was applied, as such correction improves the limitations of the density functional theory [22, 23]. We used CP2K code [24] for calculations. Atoms were described through the double-zeta polarizable basis sets [25] combined with matching pseudopotentials by Goedecker, Teter, and Hutter [26]. The cutoff of the integration grid was chosen to be 600 Ry, while the number of levels for multi-grid was 5.

It is known that PBE-D3 approach has limited accuracy for CaCl_2 simulations [17]. In order to test this method further, the AIMD simulation of CaCl_2 molecule was performed. We found that the vibrational spectrum of the simulated molecule exhibits peaks at 6, 34 and 284 cm^{-1} . The peak at 6 cm^{-1} is probably a translational mode. Peaks at 34 and 284 cm^{-1} are Cl–Ca–Cl bending and

Ca–Cl symmetric stretching vibrations, correspondingly. They are in a good agreement with the study [27] made using the gold-standard CCSD(T) approximation, where these frequencies were found to be 37 and 284 cm^{-1} . Unfortunately, the asymmetric stretching vibration was not detected since the initial configuration of the molecule was symmetrical. In Figure 1, it can be seen that the motion of chlorine ions is symmetric. Also, the average Ca–Cl separation of 2.47 Å obtained in the simulation is in excellent agreement with CCSD(T) result of 2.47 Å.

The ensemble was formed by 30 calcium and 60 chlorine atoms. A molecular dynamic cell was set to match the experimental density of 1.98 g/cm^3 [28], which corresponds to cell lengths of $14.08 \times 14.08 \times 14.08 \text{ Å}$ for our case. The periodic boundary conditions were applied. Constant-volume constant-temperature simulations at $T = 1300 \text{ K}$ were performed for 65440 steps with a time step of 2 fs. The first 15000 steps were considered as structure optimization time interval. In subsequent analysis, only the last 50440 steps were used which corresponds to $\sim 101 \text{ ps}$.

To calculate structural and transport properties, we used standard algorithms that are summarized in [29]. Beyond standard approaches, a special treatment of ion pair lifetimes was performed [30]. Also, the vibrational density of states was calculated using ion velocities, as described in [31]; for this purpose, the TRAVIS software [32] was used. Partial charges were calculated using software by Yu and Trinkle [33]. Simulations were performed on a single-node 10-core CPU.

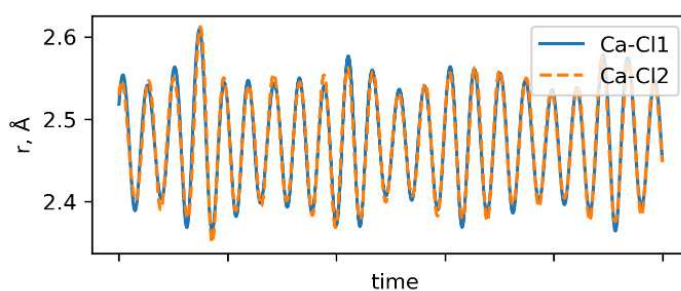


Figure 1 The Ca–Cl separations depending on time for the CaCl_2 molecule. For convenience, only a part of the trajectory is presented.

3. Results and discussions

3.1. Local structure details

In Figure 2, radial distribution functions are presented. It is seen that the positions of the global maxima conform charge ordering. Bader charge analysis [33] showed that partial charges of Ca and Cl are 1.55 and -0.775 , respectively. The closest separation of 2.7 Å is

observed for Ca–Cl pair. Chlorine ions are separated by 3.6 Å. Finally, the maximum of Ca–Ca distribution is at 4.6 Å. These values are in a good agreement with AIMD results by Bu et al. [17], where Ca–Cl, Cl–Cl and Ca–Ca distances were 2.700, 3.646 and 4.703 Å, respectively. A summary of coordination radii and coordination numbers is given in Table 1.

In the case of Cl–Cl radial distribution function, there is a local maximum at 5.3 Å. An illustrative interpretation is given in Figure 3. This maximum is produced by chlorine ions that are separated by Ca in between (for example, by those denoted as 1 and 3 in Figure 3). The global maximum at 3.6 Å is due to “neighboring” ions.

For Ca–Cl, Cl–Cl, and Ca–Ca distributions, coordination numbers are 6.7, 10.7 and 11.3, respectively. Interestingly, in [17] Ca–Cl coordination number was found to be 5.7. It can be assumed that the lower coordination number stems from the lower density of 1.889 g/cm³ used in the cited study.

Coordination numbers are time and spatially averaged values. In order to provide a probability

distribution for certain Ca–Cl coordination cases, an additional analysis was performed. The results are presented in Figure 4.

It is seen that the most probable groupings are [CaCl₇] and [CaCl₆], while [CaCl₈] and [CaCl₅] are less frequent.

The angular distribution functions obtained for Cl–Ca–Cl angles are presented in Figure 5. Unsurprisingly, probability maxima shift towards lower angles in a row [CaCl₅] → [CaCl₆] → [CaCl₇] → [CaCl₈]. In the distributions, the high-angle minor maxima correspond to the cases when chlorine ions are “opposite” like it was shown by ions 1 and 3 in Figure 3.

Table 1 – Local structure details.

Pair	<i>n</i>	<i>r</i> , Å
Ca–Cl	6.7	2.7
Cl–Cl	10.7 ^a	3.6
Ca–Ca	11.3	4.6

^a – the cutoff of 4.9 Å was used.

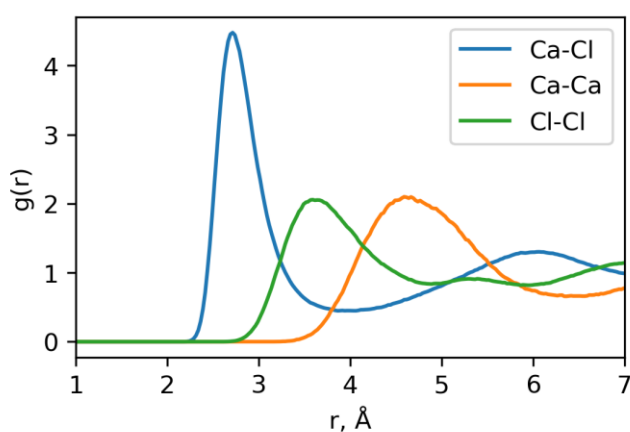


Figure 2 Radial distribution functions.

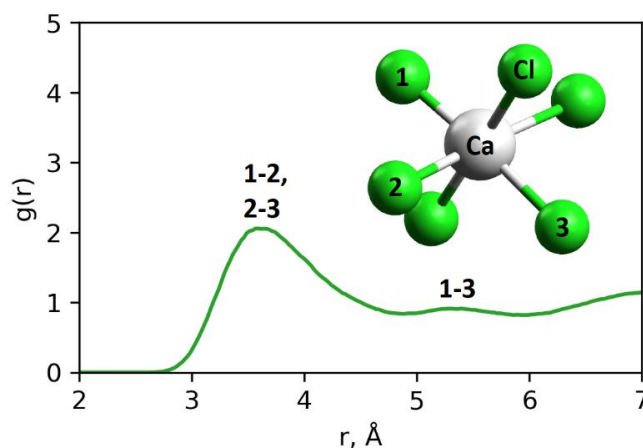


Figure 3 On the explanation of the 2nd maximum of Cl–Cl distribution.

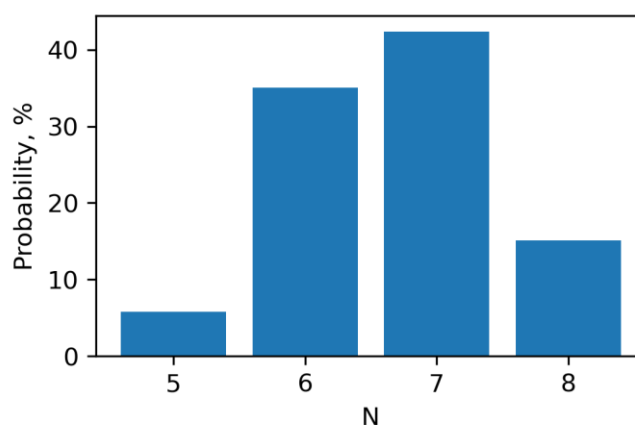


Figure 4 Probability distribution for *N* in [CaCl_{*N*}] groupings.

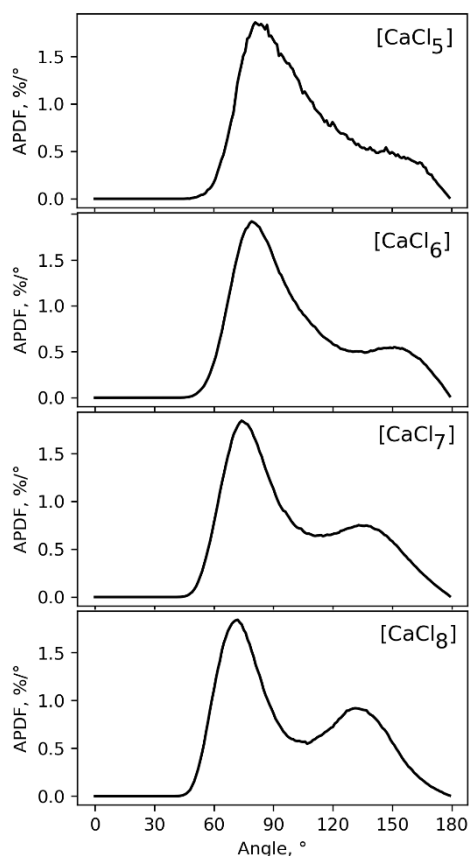


Figure 5 Angular probability distribution functions (APDF) for Cl–Ca–Cl angles.

3.2. Vibrational density of states

In order to detect bond vibrations, the vibrational density of states (VDOS) was calculated. In Figure 6, VDOS for Ca and Cl ions are presented. Both spectra exhibit a smooth distribution across the entire range, lacking pronounced peaks. It is worth noting that Ca spectrum shows an increased intensity near 220 cm^{-1} , which could be attributed to weak Ca–Cl bond vibrations.

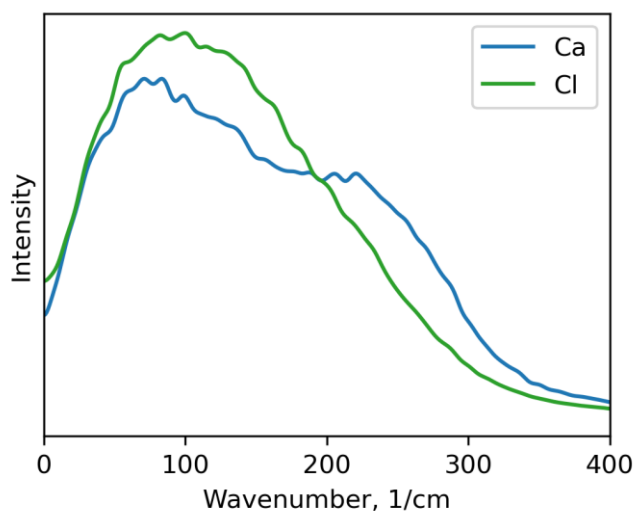


Figure 6 The vibrational density of states.

3.3. Self-diffusion coefficients

Self-diffusion coefficients (SDCs) were obtained from mean-squared displacements of ions. Due to the sufficient length of simulation run, SDCs can be calculated with a low error margin. At $T = 1300$ K, $D_{Ca} = 2.75 \cdot 10^{-9}$ m^2/s and $D_{Cl} = 3.73 \cdot 10^{-9}$ m^2/s . For comparison, the experimental temperature dependence obtained by Bockris et al. [34] gives the values of $3.54 \cdot 10^{-9}$ and $6.15 \cdot 10^{-9}$ m^2/s , respectively. On the other hand, the Ca diffusion coefficient was measured to be $1.67 \cdot 10^{-9}$ m^2/s ($T = 1221$ K) in another experimental study [35], which is notably lower compared to [34]. It can be stated that the reference data exhibit uncertainty, and our results lie between available reference values.

3.4. Ca–Cl lifetimes

In Section 3.1., instantaneous information on the local structure was presented. However, it is of great interest to investigate how stable this structure is. A convenient way to assess stability is to calculate the cation-anion bond lifetime. Here, we used an algorithm proposed in [30]. The calculated lifetime of Ca–Cl pair was found to be 2.14 ps, which is comparable to the cation-anion lifetimes in alkali halides [30]. Therefore, at $T = 1300$ K, the structure binding is relatively weak. It should be noted that for lower temperatures, Ca–Cl lifetime would be longer. Taking into account VDOS described in Section 3.2, the lifetime of 2.14 ps correspond to ~ 9 periods of chlorine ion oscillation at average. Let us propose an explanation for such a low lifetime. Despite the high formal charge of Ca, the potential energy surface apparently exhibits no pronounced local minima: due to competition between neighboring calcium ions, potential energy barriers are low. Therefore, the thermal fluctuation, which allows chlorine ions to move from one cation to another, could be small as well. One can expect that Ca–Cl lifetime would increase drastically if CaCl_2 is mixed with alkali chloride(s). In this case, a potential energy surface would become less uniform: for chlorine ions, local minima near Ca are preferential compared to minima formed with single-charged cation.

4. Conclusions

We performed *ab initio* molecular dynamics of molten CaCl_2 for ~ 100 ps. Despite the fact that the density functional theory is a relatively accurate approach, inherent limitations lead to minor disagreement in the prediction of CaCl_2 density, as was shown in [17]. For that reason, we used the experimental density for our calculations. Due to the high duration of molecular dynamic simulation, we gained sufficient statistic and calculated both instantaneous and dynamic properties.

The key findings of this study are as follows. The structure of molten CaCl_2 at 1300 K does not exhibit highly stable units, as was shown by lifetime calculation. In terms of spatial arrangement, Ca is most commonly surrounded by 7 or 6 chlorine ions, although 5- and 8-coordinated cases are possible as well. We emphasize that $[\text{CaCl}_M]$ units discussed in this paper are no more than instantaneous local coordination cases and not separate structures. These statements were supported by vibrational densities of states, where no strong vibrational bands were found. Finally, self-diffusion coefficients calculated in this study lie between available experimental data, which both supports our findings and enriches data on the transport properties of molten calcium chloride.

Supplementary materials

No supplementary materials are available.

Funding

This research had no external funding.

Acknowledgments

None.

Author contributions

Dmitry Zakiryanov: Conceptualization; Data curation; Formal Analysis; Writing – Original draft.

Conflict of interest

The authors declare no conflict of interest.

Additional information

Dmitry Zakiryanov ORCID:
<https://orcid.org/0000-0003-2649-7871>

References

- Li Y, Xu X, Wang X, Li P et al., Survey and evaluation of equations for thermophysical properties of binary/ternary eutectic salts from NaCl, KCl, MgCl_2 , CaCl_2 , ZnCl_2 for heat transfer and thermal storage fluids in CSP, *Solar Energy*, **152** (2017) 57–79. <https://doi.org/10.1016/j.solener.2017.03.019>
- Tian H, Wang W, Ding J, Wei X, Thermal performance and economic evaluation of NaCl– CaCl_2 eutectic salt for high-temperature thermal energy storage, *Energy*, **227** (2021) 120412. <https://doi.org/10.1016/j.energy.2021.120412>
- Du L, Ding J, Tian H, Wang W, et al., Thermal properties and thermal stability of the ternary eutectic salt NaCl– CaCl_2 – MgCl_2 used in high-temperature thermal energy storage process, *Applied Energy*, **204** (2017) 1225–1230. <https://doi.org/10.1016/j.apenergy.2017.03.096>

- Jacob R, Sergeev D, Yazhenskikh E, Müller M, Evaluation of the calcium chloride-calcium fluoride system for high temperature thermal energy storage, *Journal of Energy Storage*, **72** (2023) 108521. <https://doi.org/10.1016/j.est.2023.108521>
- Jones RO, Density functional theory: Its origins, rise to prominence, and future, *Reviews of Modern Physics*, **87** (2015) 897–923. <https://doi.org/10.1103/revmodphys.87.897>
- Geerlings P, De Proft F, Langenaeker W, Conceptual Density Functional Theory, *Chemical Reviews*, **103** (2003) 1793–1874. <https://doi.org/10.1021/cr990029p>
- Deringer VL, Caro MA, Csányi G, Machine Learning Interatomic Potentials as emerging Tools for Materials Science, *Advanced Materials*, **31** (2019) 1902765. <https://doi.org/10.1002/adma.201902765>
- Behler J, Perspective: Machine learning potentials for atomistic simulations, *The Journal of Chemical Physics*, **145** (2016) 170901. <https://doi.org/10.1063/1.4966192>
- Xie Y, Bu M, Zhang Y, Lu G, Effect of composition and temperature on microstructure and thermophysical properties of LiCl– CaCl_2 molten salt based on machine learning potentials, *Journal of Molecular Liquids*, **383** (2023) 122112. <https://doi.org/10.1016/j.molliq.2023.122112>
- Rong Z, Pan G, Lu J, Liu S, et al., Ab-initio molecular dynamics study on thermal property of NaCl– CaCl_2 molten salt for high-temperature heat transfer and storage, *Renewable Energy*, **163** (2020) 579–588. <https://doi.org/10.1016/j.renene.2020.08.152>
- Gegentana N, Cui L, Zhou L, Du X, Deep Potential Molecular Dynamics Systematic Study of Microstructure and Thermophysical Properties of NaCl– CaCl_2 Molten Salt System across Phase Transition Temperature, *Journal of Thermal Science*, **33** (2024) 2245–2258. <https://doi.org/10.1007/s11630-024-2054-5>
- Gegentana N, Cui L, Zhou L, Du X, A deep potential molecular dynamics study on the ionic structure and transport properties of NaCl– CaCl_2 molten salt, *Ionics*, **30** (2023) 285–295. <https://doi.org/10.1007/s11581-023-05265-8>
- Bu M, Liang W, Lu G, Yu J, Local structure elucidation and properties prediction on KCl– CaCl_2 molten salt: A deep potential molecular dynamics study, *Solar Energy Materials and Solar Cells*, **232** (2021) 111346. <https://doi.org/10.1016/j.solmat.2021.111346>
- Xie Y, Bu M, Lu G, Local structure and thermophysical property prediction for CaCl_2 –KCl molten salt with machine learning potentials, *Materials Today Communications*, **41** (2024) 110243. <https://doi.org/10.1016/j.mtcomm.2024.110243>
- Luo X, Ling C, Xu T, Liu W et al., Thermophysical property and micro-structure of the molten NaCl–KCl– CaCl_2 salt at high temperature by FPMD simulation, *Solar Energy Materials and Solar Cells*, **288** (2025) 113630. <https://doi.org/10.1016/j.solmat.2025.113630>
- Xie Y, Bu M, Lu G, Insights into CaCl_2 –NaCl–KCl molten salt: A machine learning approach to unraveling structure and properties, *Journal of Energy Storage*, **102** (2024) 114156. <https://doi.org/10.1016/j.est.2024.114156>
- Bu M, Liang W, Lu G, Yu J, Static and dynamic ionic structure of molten CaCl_2 via first-principles molecular dynamics simulations, *Ionics*, **27** (2020) 771–779. <https://doi.org/10.1007/s11581-020-03852-7>

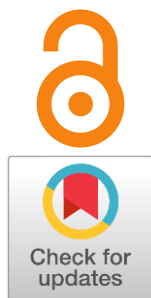
18. Perdew JP, Burke K, Ernzerhof M, Generalized gradient approximation made simple, *Physical Review Letters*, **77** (1996) 3865–3868. <https://doi.org/10.1103/physrevlett.77.3865>
19. Umesaki N, Structural characterization of molten calcium chloride by molecular dynamics simulation, *AIP Conference Proceedings*, **256** (1992) 561–562. <https://doi.org/10.1063/1.42392>
20. Biggin S, Enderby JE, The structure of molten calcium chloride, *Journal of Physics C Solid State Physics*, **14** (1981) 3577–3583. <https://doi.org/10.1088/0022-3719/14/25/006>
21. Grimme S, Antony J, Ehrlich S, Krieg H, A consistent and accurate *ab initio* parametrization of density functional dispersion correction (DFT-D) for the 94 elements H-Pu, *The Journal of Chemical Physics*, **132** (2010) 154104. <https://doi.org/10.1063/1.3382344>
22. Grimme S, Hansen A, Brandenburg JG, Bannwarth C, Dispersion-Corrected Mean-Field electronic structure Methods, *Chemical Reviews*, **116** (2016) 5105–5154. <https://doi.org/10.1021/acs.chemrev.5b00533>
23. Goerigk L, A comprehensive overview of the DFT-D3 London-Dispersion correction, in: Elsevier eBooks, 2017: pp. 195–219. <https://doi.org/10.1016/b978-0-12-809835-6.00007-4>
24. Kühne TD, Iannuzzi M, Del Ben M, Rybkin VV et al., CP2K: An electronic structure and molecular dynamics software package - Quickstep: Efficient and accurate electronic structure calculations, *The Journal of Chemical Physics*, **152** (2020) 194103. <https://doi.org/10.1063/5.0007045>
25. VandeVondele J, Hutter J, Gaussian basis sets for accurate calculations on molecular systems in gas and condensed phases, *The Journal of Chemical Physics*, **127** (2007) 114105. <https://doi.org/10.1063/1.2770708>
26. Goedecker S, Teter M, Hutter J, Separable dual-space Gaussian pseudopotentials, *Physical Review. B, Condensed Matter*, **54** (1996) 1703–1710. <https://doi.org/10.1103/physrevb.54.1703>
27. Koput J, *Ab Initio* Prediction of the Potential Energy Surface and Vibration-Rotation Energy Levels of CaCl₂, *Journal of Physical Chemistry A*, **112** (2008) 2743–2746. <https://doi.org/10.1021/jp711785p>
28. Janz GJ, Thermodynamic and transport properties for molten salts: correlation equations for critically evaluated density, surface tension, electrical conductance, and viscosity data, *Journal of Physical and Chemical Reference Data*, **17** (1988) 309.
29. Porter T, Vaka MM, Steenblik P, Della Corte D, Computational methods to simulate molten salt thermophysical properties, *Communications Chemistry*, **5** (2022) 69. <https://doi.org/10.1038/s42004-022-00684-6>
30. Zakiryanov D, The refined determination of the ion pair lifetimes in ionic liquids, *Computational and Theoretical Chemistry*, **1210** (2022) 113646. <https://doi.org/10.1016/j.comptc.2022.113646>
31. Thomas M, Brehm M, Fligg R, Vöhringer P, et al., Computing vibrational spectra from *ab initio* molecular dynamics, *Physical Chemistry Chemical Physics*, **15** (2013) 6608. <https://doi.org/10.1039/c3cp44302g>
32. Brehm M, Kirchner B, TRAVIS - a free analyzer and visualizer for Monte Carlo and molecular dynamics trajectories, *Journal of Chemical Information and Modeling*, **51** (2011) 2007–2023. <https://doi.org/10.1021/ci200217w>
33. Yu M, Trinkle DR, Accurate and efficient algorithm for Bader charge integration, *The Journal of Chemical Physics*, **134** (2011) 064111. <https://doi.org/10.1063/1.3553716>
34. Bockris JO, Richards SR, Nanis L, Self-Diffusion and structure in molten group II chlorides, *The Journal of Physical Chemistry*, **69** (1965) 1627–1637. <https://doi.org/10.1021/j100889a031>
35. Ichikawa K, Shimoji M, Niwa K, Impurity diffusion of calcium ions in alkali chloride + calcium chloride mixed melts and Self-Diffusion of calcium ions in molten calcium chloride, *Berichte Der Bunsengesellschaft Für Physikalische Chemie*, **69** (1965) 248–255. <https://doi.org/10.1002/bbpc.19650690313>

Details on oxygen surface exchange mechanism over $\text{Pr}_{1.6}\text{Ca}_{0.4}\text{Ni}_{1-y}\text{Cu}_y\text{O}_{4+\delta}$ solid oxide fuel cell/electrolyzer air electrodes

Received: 8 June 2025
Accepted: 16 June 2025
Published online: 20 June 2025

Vladislav Sadykov^a, Ekaterina Sadovskaya^a, Nikita Ereemeev^{a*},
Elena Pikalova^b

DOI: [10.15826/elmattech.2025.4.053](https://doi.org/10.15826/elmattech.2025.4.053)



In the design of solid oxide fuel cell/electrolyzer air electrodes, the oxygen mobility and surface reactivity are of paramount importance. In this study, the oxygen surface heteroexchange rate is examined for a series of promising electrode materials, $\text{Pr}_{1.6}\text{Ca}_{0.4}\text{Ni}_{1-y}\text{Cu}_y\text{O}_{4+\delta}$ ($y = 0.0\text{--}0.4$). The investigation encompasses the relationship between this rate and the structural, surface, and electrochemical properties. Single-phase materials synthesized by a nitrate combustion technique using glycerol as a fuel possess an orthorhombic structure. The oxygen surface reactivity is studied by the temperature-programmed isotope exchange of oxygen with $^{18}\text{O}_2$ in a flow reactor. The values of the oxygen heteroexchange rate (R^*) and surface exchange constant (k^*) are acquired using mathematical modeling. The isotope exchange between the gas oxygen and the sample surface occurs primarily via the R^2 -type of exchange mechanism, i.e., the simultaneous exchange of two atoms of the oxygen molecule with two atoms of oxygen in the sample surface. The process is limited by surface exchange of oxygen characterized by high values of surface exchange constant (up to $\sim 10^{-5}$ cm/s at 700 °C). The best characteristics are achieved for the $\text{Pr}_{1.6}\text{Ca}_{0.4}\text{Ni}_{1-y}\text{Cu}_y\text{O}_{4+\delta}$ samples, $y = 0.0\text{--}0.2$. There is a correlation of the oxygen exchange kinetic parameters (surface exchange constant, tracer diffusion coefficient) with the electrochemical properties of the electrodes according to the Adler–Lane–Steele model.

keywords: solid oxide fuel cells, solid oxide electrolyzers, layered nickelates, oxygen surface exchange, isotope exchange of oxygen

© 2025, the Authors. This article is published in open access under the terms and conditions of the Creative Commons Attribution (CC BY) license (<http://creativecommons.org/licenses/by/4.0/>).

1. Introduction

First-order Ruddlesden–Popper (RP) phases $L_n\text{MO}_{4+\delta}$ ($L_n = \text{La, Pr, Nd, etc.}$; $M = \text{Co, Ni, Cu, etc.}$) have attracted considerable attention due to their efficient application in solid oxide fuel cells (SOFCs) and electrolyzers (SOEs) as air [1–7] and fuel [2, 5, 8–10] electrodes, oxygen separation membranes [11–13], and components of catalysts for hydrogen and syngas production [11, 14]. They have also demonstrated promise in a variety of other applications [15, 16]. Their high performances in such applications are provided by the distinguishable features of these materials due to a layered structure comprising alternating perovskite and rock-salt layers. Among their advances are high mixed ionic-electronic conductivity, oxygen mobility and surface

reactivity, moderate thermal expansion coefficients and chemical stability under operating conditions (except for $\text{Pr}_2\text{NiO}_{4+\delta}$). In particular, achieving a high level of oxygen mobility and surface reactivity is imperative to ensure the effective operation of the SOFC/SOE air electrodes. In this case, the electrode reaction (oxygen reduction/evolution reactions, ORR/OER) is not limited by a triple-phase boundary (gas – electrode – electrolyte), but occurs on a double-phase boundary (gas–electrode) as well [3–5, 7, 17–19]. There has been an Adler–Lane–Steele (ALS) model, in which the mixed ion-electron conducting (MIEC) electrode performance correlates with the oxygen self-diffusion coefficient and surface exchange constant values of the electrode material as well as the microstructure features [19–21].

Excellent oxygen transport properties of first-order RP phases, including L_n nickelates, are attributed to a cooperative mechanism of oxygen migration involving both regular and highly mobile interstitial oxygen

^a: Federal Research Center Boreskov Institute of Catalysis SB RAS, Novosibirsk 630090, Russia

^b: Institute of High-Temperature Electrochemistry UB RAS, Ekaterinburg 620066, Russia

* Corresponding author: yeremeev21@catalysis.ru

presented in a high excess [3, 7, 12, 19, 22–27]. This mechanism (known also as an interstitial mechanism) involves the movement of interstitial oxygen in a rock salt layer across the Ln_3 triangle into the apical position of NiO_6 octahedra in a perovskite layer, and this apical oxygen is displaced across the neighboring Ln_3 triangle into the interstitial position. Such a mechanism provides high values of the oxygen self-diffusion coefficient (up to $\sim 10^{-8}$ – 10^{-7} cm^2/s at 700 °C). The doping of A - and B -sites with various cations has been demonstrated to exert a substantial influence on the cooperative mechanism and, consequently, on the oxygen mobility of the RP phases [22, 24–30]. This is related to the interstitial oxygen content, the size of the dopant cation, as well as other structural and defect features.

Another salient feature pertains to oxygen surface reactivity, given that surface exchange of oxygen in the oxide and in the gas phase constitutes a pivotal process in ORR/OER [31–33]. Interstitial oxygen in the rock salt layers and regular oxygen in the perovskite layers have been demonstrated to be two major active centers for ORR and OER. The governing factors have been demonstrated to be oxygen adsorption and incorporation. Ln nickelates have been shown to exhibit high values of the oxygen surface exchange constant (up to $\sim 10^{-7}$ – 10^{-6} cm/s at 700 °C) [26, 28, 29, 32, 34–36]. The surface exchange of oxygen for RP phases typically occurs via R^1 and R^2 type of exchange mechanisms according to the Muzykantov's classification [37, 38], i.e., the simultaneous exchange of one or two oxygen atoms from the oxygen molecule with one or two oxygen atoms from the oxide surface, respectively. The rate-determining steps in this process are believed to be either oxygen dissociative adsorption and incorporation, or both stages may be competing depending on the sample composition and synthesis technique. It has been demonstrated that interstitial oxygen plays an important role in the incorporation of adsorbed oxygen [26, 32, 33, 35]. The oxygen surface exchange process is influenced by the dopant nature and content due to the effects of surface properties, defects, the rate-determining step, the affinity of oxygen to A - and B -site cations, and the surface diffusion energy barrier [27–29, 33–36].

In several recent works performed jointly in IHTE UB RAS, UrFU and BIC SB RAS [39–41], the physicochemical properties of $Pr_{1.6}Ca_{0.4}Ni_{1-y}Cu_yO_{4+\delta}$ ($y = 0.0$ – 0.4) materials perspective for air electrodes in various electrochemical devices have been studied. The materials have demonstrated a moderate level of the total conductivity (σ_{tot} , 155–90 S/cm at 700 °C depending on the Cu content) and the thermal expansion coefficient (TEC, 13.5 – 13.7×10^{-6} K^{-1} in the range of 100–900 °C).

They exhibit excellent phase stability and chemical and thermomechanical compatibility with CeO_2 - and $BaCe(Zr)O_3$ -based electrolytes. Moreover, Cu-doping was found to enhance the electrochemical activity of the related electrodes. For instance, the polarization resistance of the $Pr_{1.6}Ca_{0.4}Ni_{0.8}Cu_{0.2}O_{4+\delta}$ electrode is in the range of 0.19–0.27 $\Omega \cdot cm^2$ (at 700 °C) depending on the electrolyte substrate [39]. According to the data obtained using temperature-programmed isotope exchange of oxygen (TPIE) with $C^{18}O_2$ in a flow reactor, the highest D^* value for O_{fast} moving via the cooperative mechanism, was demonstrated for $Pr_{1.6}Ca_{0.4}Ni_{0.8}Cu_{0.2}O_{4+\delta}$ equal to $9.4 \cdot 10^{-8}$ cm^2/s at 700 °C [41]. To complement these findings, in the present work, the surface exchange properties of these materials have been studied by TPIE with $^{18}O_2$. The correlation of the electrode performance with oxygen surface heteroexchange rate and diffusion coefficient values according to the ALS model has been demonstrated.

2. Experimental

The materials of the $Pr_{1.6}Ca_{0.4}Ni_{1-y}Cu_yO_{4+\delta}$ ($y = 0.0$ – 0.4 , PCNO, PCNCO01–PCNCO04) series were synthesized by nitrate combustion using glycerol as a fuel, as described in detail in the works [39, 41].

The structural properties of the materials were examined after the final step by powder X-ray diffraction (XRD) analysis using a Shimadzu XRD-7000 diffractometer (Japan) with a graphite monochromator with $Cu K\alpha_1$ radiation at room temperature in air. The XRD patterns were obtained over the angle range of $10 < 2\theta < 90$ with a step size of 0.02 ° and an exposure time of 5 s at each point.

A Brunauer–Emmett–Teller (BET) method was employed to determine the specific surface area values, utilizing a SORBI N.4.1 analyzer (Meta, Russia).

The oxygen surface reactivity of the samples was studied by the temperature-programmed isotope exchange (TPIE) of oxygen with $^{18}O_2$ in a flow reactor. The samples (0.25–0.5 mm fraction, 50 mg weight) were loaded into a quartz tubular reactor (inner diameter of 3 mm). Pretreatment was carried out at 700 °C during 0.5 h in a flow of 1 % O_2 + He (flow rate of 25 ml/min) followed by cooling. The TPIE experiments were carried out in 1 % $^{18}O_2$ + He (flow rate of 25 ml/min) while heating from 50 °C to 800 °C with a ramp of 5 °C/min. The gas phase composition at the reactor outlet was analyzed by a UGA 200 mass spectrometer (Stanford Research Systems, USA). The dependencies of the ^{18}O atomic fraction (α) and the $^{16}O^{18}O$ molecular fraction (f_{34}) in the gas phase were used for calculations of isotope

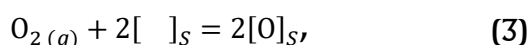
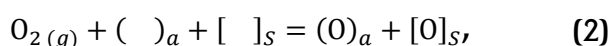
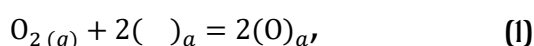
exchange kinetic parameters via mathematical modeling [29, 42, 43].

3. Theory

3.1. Dissociative adsorption-desorption and three types of exchange mechanisms

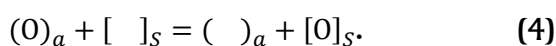
The surface exchange of oxygen in the molecular oxygen – solid oxide systems is known to occur via the Muzykantov–Boreskov mechanism, or the dissociative adsorption-desorption mechanism [26, 29, 35, 36, 44–46], which includes the steps of:

- physical adsorption;
- chemisorption of an oxygen molecule with its dissociation (Equations 1–3):



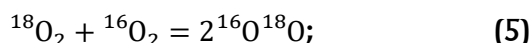
where $(\)_a$ and $[\]_S$ are the adsorption site and oxygen vacancy on the surface, respectively, $(O)_a$ and $[O]_S$ are the adsorbed (weakly bound, capable of surface diffusion) and surface (strongly bound with oxygen vacancy) oxygen species, respectively;

- incorporation (Equation 4):

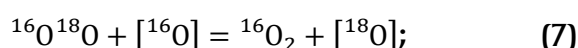
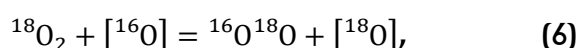


For isotope exchange with $^{18}O_2$ (as well as other molecules containing two identical atoms), according to the Muzykantov's classification [37, 38], there are three types of exchange mechanism:

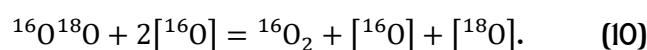
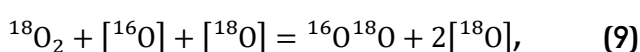
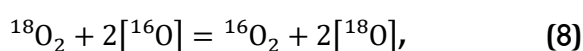
- Homoexchange
- R^0 -type (O-atomic type, I type, Equation 5):



- Heteroexchange
- R^1 -type (I-atomic type, II type, Equations 6 and 7):



- R^2 -type (2-atomic type, III type, Equations 8–10):



3.2. Mathematical models for description of TPIE $^{18}O_2$ data

There are two models applied in this work for the description of isotope exchange data:

- Model 1 (Equations 11–17) considering a direct exchange of molecular oxygen with the oxygen of the oxide surface [29];

- Model 2 (two-step model, Equations 18–25) considering the exchange of the molecular oxygen with the chemisorbed oxygen atoms ($O_2^{GAS} \leftrightarrow O_{ADS}$, as formed according to the Equations 1–3) followed by the exchange of the chemisorbed oxygen atoms with the surface oxygen of the oxide surface ($O_{ADS} \leftrightarrow O_S$, Equation 4).

Model 1

$$\frac{\partial \alpha_G}{\partial t} + \frac{1}{\tau} \frac{\partial \alpha_G}{\partial \xi} = \frac{N_S}{N_G} R(\alpha_S - \alpha_G) \quad (11)$$

$$\frac{\partial \alpha_S}{\partial t} = R(\alpha_G - \alpha_S) - \frac{N_{BULK}}{N_S} \frac{D}{h^2} \frac{\partial \alpha_{BULK}}{\partial \eta} \Big|_{\eta=0} \quad (12)$$

$$\frac{\partial \alpha_{BULK}}{\partial t} = \frac{D}{h^2} \frac{\partial^2 \alpha_{BULK}}{\partial \eta^2} \quad (13)$$

In the case of R^0 -type of exchange mechanism:

$$\frac{\partial f_{34}}{\partial t} + \frac{1}{\tau} \frac{\partial f_{34}}{\partial \xi} = \frac{N_S}{N_G} R^0(2\alpha_G(1 - \alpha_G) - f_{34}) \quad (14)$$

In the case of R^1 -type of exchange mechanism:

$$\frac{\partial f_{34}}{\partial t} + \frac{1}{\tau} \frac{\partial f_{34}}{\partial \xi} = \frac{N_S}{N_G} (R^1(\alpha_G(1 - \alpha_S) + 2\alpha_S(1 - \alpha_G) - f_{34}), R^1 = 2R) \quad (15)$$

In the case of R^2 -type of exchange mechanism:

$$\frac{\partial f_{34}}{\partial t} + \frac{1}{\tau} \frac{\partial f_{34}}{\partial \xi} = \frac{N_S}{N_G} (R^2(2\alpha_S(1 - \alpha_S) - f_{34}), R^2 = R) \quad (16)$$

Initial and boundary conditions:

$$\begin{aligned} t = 0: \alpha &= \alpha_{OX} = f_{34} = 0 \\ \xi = 0: \alpha &= \alpha^{input}, f_{34} = f_{34}^{input} \end{aligned} \quad (17)$$

Here, N_G , N_S and N_{BULK} are the numbers of atoms in the gas phase, on the surface and in the bulk of the oxide, respectively; R^1 and R^2 are the exchange rates via R^1 - and

R^2 -types of mechanism, respectively, D is the tracer diffusion coefficient, h is the characteristic size of the oxide particle; η is a dimensionless distance from the oxide surface; α_G , α_{OX} , α_S and α_{BULK} are ^{18}O fractions in the gas phase, in the oxide, on the surface and in the bulk of the oxide, respectively; t is time; τ is the contact time; ξ is dimensionless length of the sample layer in the reactor.

Model 2

$$\frac{\partial \alpha_G}{\partial t} + \frac{1}{\tau} \frac{\partial \alpha_G}{\partial \xi} = \frac{N_{ADS}}{N_G} R(\alpha_{ADS} - \alpha_G) \quad (18)$$

$$\frac{\partial \alpha_{ADS}}{\partial t} = R(\alpha_G - \alpha_{ADS}) - \frac{N_S}{N_{ADS}} (\alpha_S - \alpha_{ADS}) \quad (19)$$

$$\frac{\partial \alpha_S}{\partial t} = R(\alpha_{ADS} - \alpha_S) - \frac{N_{BULK}}{N_S} \frac{D}{h^2} \frac{\partial \alpha_{BULK}}{\partial \eta} \Big|_{\eta=0} \quad (20)$$

$$\frac{\partial \alpha_{BULK}}{\partial t} = \frac{D}{h^2} \frac{\partial^2 \alpha_{BULK}}{\partial \eta^2} \quad (21)$$

In the case of R^0 -type of exchange mechanism:

$$\frac{\partial f_{34}}{\partial t} + \frac{1}{\tau} \frac{\partial f_{34}}{\partial \xi} = \frac{N_{ADS}}{N_G} R^0 (2\alpha_G(1 - \alpha_G) - f_{34}) \quad (22)$$

In the case of R^1 -type of exchange mechanism:

$$\frac{\partial f_{34}}{\partial t} + \frac{1}{\tau} \frac{\partial f_{34}}{\partial \xi} = \frac{N_{ADS}}{N_G} (R^1 (\alpha_G(1 - \alpha_{ADS}) + \alpha_{ADS}(1 - \alpha_G) - f_{34}), R^1 = 2R \quad (23)$$

In the case of R^2 -type of exchange mechanism:

$$\frac{\partial f_{34}}{\partial t} + \frac{1}{\tau} \frac{\partial f_{34}}{\partial \xi} = \frac{N_{ADS}}{N_G} R^2 (2\alpha_{ADS}(1 - \alpha_{ADS}) - f_{34}), \quad R^2 = R \quad (24)$$

Initial and boundary conditions:

$$t = 0: \alpha_G = \alpha_{ADS} = \alpha_S = \alpha_{BULK} = f_{34} = 0 \quad (25)$$

$$\xi = 0: \alpha_G = \alpha^{input}, f_{34} = f_{34}^{input}$$

Here, α_{ADS} is ^{18}O fraction of the adsorbed oxygen, N_{ADS} is the number of adsorbed oxygen atoms.

3.3. Adler–Lane–Steele model

For elucidation of the correlations of the electrochemical performance of electrodes with the oxygen exchange and diffusion rates, the ALS model (Equation 26) is applied [20, 21, 28, 47]:

$$R_p = \frac{RT}{4F} \sqrt{\frac{\pi_{tort}}{(1 - \pi_{por})^4 S_{sp} C_O D_{over}^* k^*}} \quad (26)$$

where R_p is the polarization resistance of the electrode; F is the Faraday constant; π_{tort} and π_{por} are the electrode tortuosity and porosity, respectively; S_{sp} is the specific surface area of the electrode; C_O is the molar concentration of oxide anions in the oxide; D_{over}^* is the mean integral oxygen tracer diffusion coefficient; k^* is the oxygen surface exchange constant.

Hence, the correlations between R_p and $(D_{over}^* k^*)^{0.5}$ can be considered. D_{over}^* can be calculated considering the diffusion coefficients of various oxygen forms. k^* can be calculated as being proportional to the oxygen surface heteroexchange rate [35, 48].

4. Results and discussion

4.1. Structural features and oxygen content

According to the XRD data (Figure 1), all $\text{Pr}_{1.6}\text{Ca}_{0.4}\text{Ni}_{1-y}\text{Cu}_y\text{O}_{4+\delta}$ ($y = 0.0-0.4$) samples are single-phase and possess an orthorhombic structure with the $Bmab$ space group. The refinement of unit cell parameters was carried out using the Rietveld full-profile analysis method with the FullProf Suite software (presented in Table 1). The unit cell parameter c increases with increasing Cu content in the series, whereas the a and b parameters decrease, which can be related to the tendency of Jahn–Teller Cu^{2+} ions to form elongated CuO_6 octahedra [49, 50]. These multidirectional changes result in an increase in the unit cell volume. More detailed data on the structural characterization of samples are presented in the authors' previous works [39, 41].

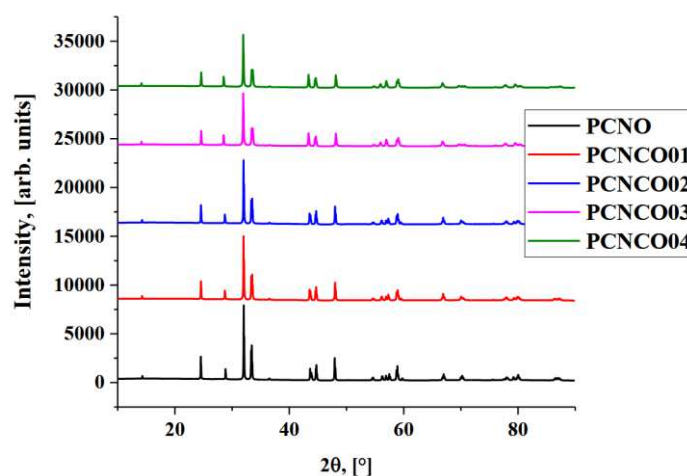
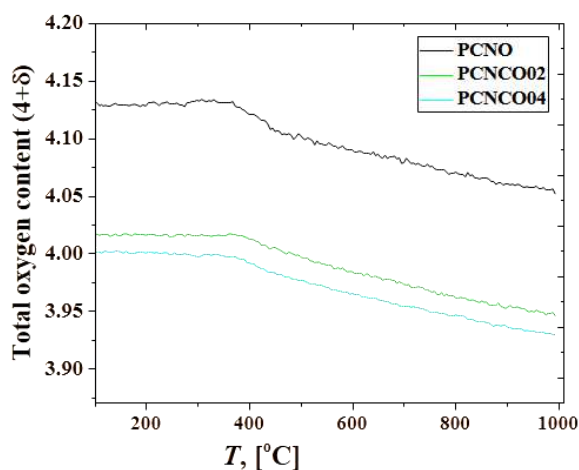


Figure 1 XRD patterns obtained at room temperature for the as-synthesized $\text{Pr}_{1.6}\text{Ca}_{0.4}\text{Ni}_{1-y}\text{Cu}_y\text{O}_{4+\delta}$ materials. Reproduced from Ref. [41] under the CC BY 4.0 license.

Table 1 – Structure parameters and oxygen content for the $\text{Pr}_{1.6}\text{Ca}_{0.4}\text{Ni}_{1-y}\text{Cu}_y\text{O}_{4+\delta}$ series [39, 41].

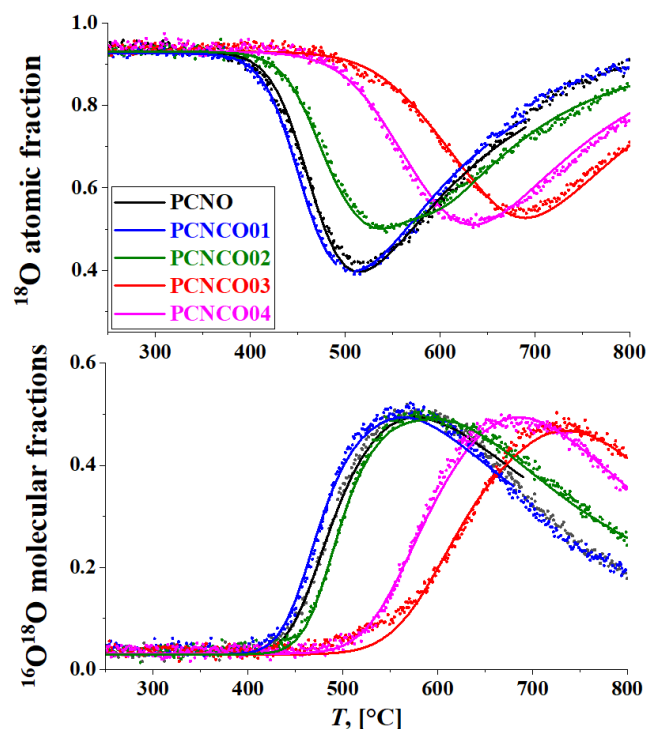
y	0.0	0.1	0.2	0.3	0.4
Sample designation	PCNO	PCNCO01	PCNCO02	PCNCO03	PCNCO04
a , [Å]	5.3537(1)	5.3441(2)	5.3340(3)	5.3270(1)	5.3220(2)
b , [Å]	5.3726(2)	5.3686(3)	5.3626(3)	5.3580(1)	5.3560(2)
c , [Å]	12.3706(3)	12.4166(3)	12.4659(3)	12.5051(4)	12.5521(4)
V , [Å ³]	355.82(2)	356.24(1)	356.58(1)	356.98(2)	357.8(2)
$4+\delta$	4.12	4.09	4.02	3.97	4.00

The oxygen content according to the TGA data [39, 41] is given in Table 1. The examples of temperature dependencies of oxygen overstoichiometry according to the TGA data in air are given in Figure 2. The overall oxygen content decreases with increasing temperature due to the oxygen desorption, which is typical for first-order RP phases. More detailed data on the oxygen content of the samples are presented in the authors' previous works [39, 41].

**Figure 2** Total oxygen content in the materials of the $\text{Pr}_{1.6}\text{Ca}_{0.4}\text{Ni}_{1-y}\text{Cu}_y\text{O}_{4+\delta}$ series, as defined via TGA data in air. Reproduced from Ref. [41] under the CC BY 4.0 license.

4.2. Oxygen surface reactivity

Figure 3 (upper image) demonstrates the dependencies for the ^{18}O atomic fractions in the gas phase oxygen (α_G) acquired for the $\text{Pr}_{1.6}\text{Ca}_{0.4}\text{Ni}_{1-y}\text{Cu}_y\text{O}_{4+\delta}$ samples during TPIE run. The variation of α_G depends on both surface exchange rates and bulk diffusion of oxygen. The higher the total rate of O_2 exchange with the oxide oxygen – the lower the temperature at which a significant decrease in α_G is observed. As illustrated in Figure 3, the $\alpha_G(T)$ dependencies for the PCNO and PCNCO01 samples are highly analogous. A slight decrease in the observed exchange rate for the PCNCO01 sample is most likely related to the higher specific surface area (S_{sp} is 1.5 m^2/g and 2.1 m^2/g for the PCNO and PCNCO01 samples, respectively). The oxygen surface exchange rate demonstrates a substantial decline when the Cu content is

**Figure 3** Temperature-programmed isotope exchange of oxygen with $^{18}\text{O}_2$ in the flow reactor for the $\text{Pr}_{1.6}\text{Ca}_{0.4}\text{Ni}_{1-y}\text{Cu}_y\text{O}_{4+\delta}$ samples. Points – experiment, lines – modeling.

elevated from $y = 0.1$ to 0.3 (PCNCO01–03). However, a subsequent increase in the Cu content to $y = 0.4$ (PCNCO04) results in an increase in the oxygen surface exchange rate.

The potential causes of the decrease in the oxygen surface exchange rate with increasing the Cu content in the $\text{Pr}_{1.6}\text{Ca}_{0.4}\text{Ni}_{1-y}\text{Cu}_y\text{O}_{4+\delta}$ ($y = 0.0$ –0.3) are evident. It has been established that CuO exhibits an oxygen surface heteroexchange rate with $^{18}\text{O}_2$ that is approximately one order of magnitude lower than that of NiO [51]. $\text{Pr}_2\text{CuO}_{4+\delta}$ exhibits reduced activity in the isotope exchange of oxygen in comparison with $\text{Pr}_2\text{NiO}_{4+\delta}$ [52].

However, Miyoshi et al. [53] have shown that the substitution of Ni with Cu has a significant impact on both mixed conductivity and oxygen diffusion. Specifically, two compositions of $\text{Pr}_2\text{Ni}_{0.8}\text{Cu}_{0.2}\text{O}_{4+\delta}$ and $\text{Pr}_2\text{Ni}_{0.75}\text{Cu}_{0.25}\text{O}_{4+\delta}$ showed considerably higher oxygen permeation rates of 60 and 100 $\mu\text{mol} \cdot \text{min}^{-1} \cdot \text{cm}^{-2}$ at

1000 °C through a membrane with a thickness of 0.5 mm than that of the other B -site doped (with Co, Fe, Mn, Zn, Al, Ga, Mg) $\text{Pr}_2\text{NiO}_{4+\delta}$ oxides.

Yashima et al. [54], using Density Functional Theory calculations, have shown that in the $\text{Pr}_2\text{Ni}_{1-x}\text{Cu}_x\text{O}_{4+\delta}$ crystal structure the degeneracy in molecular or ionic complexes with electronically degenerate states can be removed by a distortion where the Cu–O bond length in the direction perpendicular to the perovskite layer (bonds between Cu^{2+} and apical oxygen ions), increases. Due to the distortion, the bonds between Cu^{2+} and the apical oxygen ions are weaker than the bonds between Cu^{2+} and the equatorial oxygen ions. Thereby, the apical ion can contribute to oxygen ion diffusion by moving into the interstitial site. This creates a vacancy at the apical site while simultaneously increasing the number of ionic charge carriers.

It is established that highly mobile interstitial oxygen plays a crucial role in the surface exchange for RP phases [26, 32, 33, 35]. The observed decrease in the oxygen surface exchange rate in the row of $\text{Pr}_{1.6}\text{Ca}_{0.4}\text{Ni}_{1-y}\text{Cu}_y\text{O}_{4+\delta}$ ($y = 0.0\text{--}0.3$) (Figure 3) is in agreement with the decrease in the interstitial oxygen content (Table 1), as well as the decrease in the oxygen tracer diffusion coefficient values with increasing Cu content, as previously demonstrated by C^{18}O_2 TPIE [41].

The PCNCO04 sample exhibits slightly higher oxygen content ($\delta = 0.00$) compared to PCNCO03 ($\delta = -0.03$, Table 1) [39, 41].

A higher surface reactivity for the PCNCO04 sample compared to the PCNCO03 one may also be related to the surface properties. As demonstrated in the work [39] by X-ray photoelectron spectroscopy (XPS), there are four forms of surface oxygen for the PCNCO samples with a binding energy of 528.8, 530.15, 531.2 and 532.6 eV (Table 2). The first two forms likely correspond to the structural oxygen associated with Ni and Pr [39]. The third form may correspond to the oxygen within $(\text{CO}_3)^{2-}$ groups, as well as adsorbed oxygen and oxygen in the defect sites of the crystal lattice [39, 55, 56]. The peak at 532.6 eV may be associated with adsorbed water [39, 54]. The PCNCO04 sample exhibits the greatest contribution

of the surface oxygen linked to Pr (Table 2) [39]. All of these factors may be considered responsible for the higher oxygen surface exchange rate for the PCNCO04 sample compared to the PCNCO03 one.

The effect of the diffusion retardation on the dynamics of exchange with $^{18}\text{O}_2$ can be demonstrated qualitatively by comparing the dynamic extent of exchange (X), defined as the amount of oxygen substituted at a given point in time divided by its total amount in the sample (Equation 27), during TPIE $^{18}\text{O}_2$ and C^{18}O_2 [41] runs (Figure 4).

$$X = \frac{1}{N} \frac{2C_{\text{O}_2}U}{\alpha_{\text{input}}R_T} \int_{T_0}^{T_{\text{end}}} (\alpha_{\text{input}} - \alpha_G) dT \quad (27)$$

where N is the total amount of oxygen atoms in the sample, C_{O_2} is the oxygen concentration in the gas phase, U is the flow rate, R_T is the heating ramp rate.

As follows from Figure 4, the onset of isotope exchange with $^{18}\text{O}_2$ is shifted by ~ 100 °C or more towards higher temperatures compared to the exchange with C^{18}O_2 for all samples. Therefore, the dynamics of exchange with $^{18}\text{O}_2$ at low temperatures is limited by the exchange of oxygen in the gas phase with oxygen on the sample surface. While reaching $X = 20$ % (i.e. approaching the minima of the α_G curves), the extent of exchange with C^{18}O_2 for the PCNO and PCNCO01 samples is ~ 60 %, while for other samples, this extent is significantly lower. This suggests that the limiting effect of bulk diffusion is negligible for the PCNO and PCNCO01 samples, while it can be substantial for other samples, particularly PCNCO02.

Based on the mathematical modeling employing Model 1 (Equations 11–17) a satisfactory description of the $\alpha_G(T)$ dependencies is obtained. The oxygen tracer diffusion coefficient values are derived from the TPIE C^{18}O_2 data acquired in the authors' previous work [41]. The estimation errors for calculating the oxygen tracer diffusion coefficients and their effective activation energies do not exceed ± 15 % (if the other is not specified) [41]. These values (Table 3) are then used in

Table 2 – The contribution (in [%]) of the oxygen states peaks to the total O1s XPS spectra [39].

Sample	528.8 eV	530.15 eV	531.2 eV	0.3
	Ni–O	Pr–O	$(\text{CO}_3)^{2-}$	$(\text{H}_2\text{O})_{\text{ads}}$
PCNO	30.1	19.5	42.0	8.4
PCNCO01	30.0	18.7	43.3	7.9
PCNCO02	27.7	16.6	45.2	10.5
PCNCO03	30.8	16.9	39.2	13.1
PCNCO04	27.5	21.3	35.5	15.6

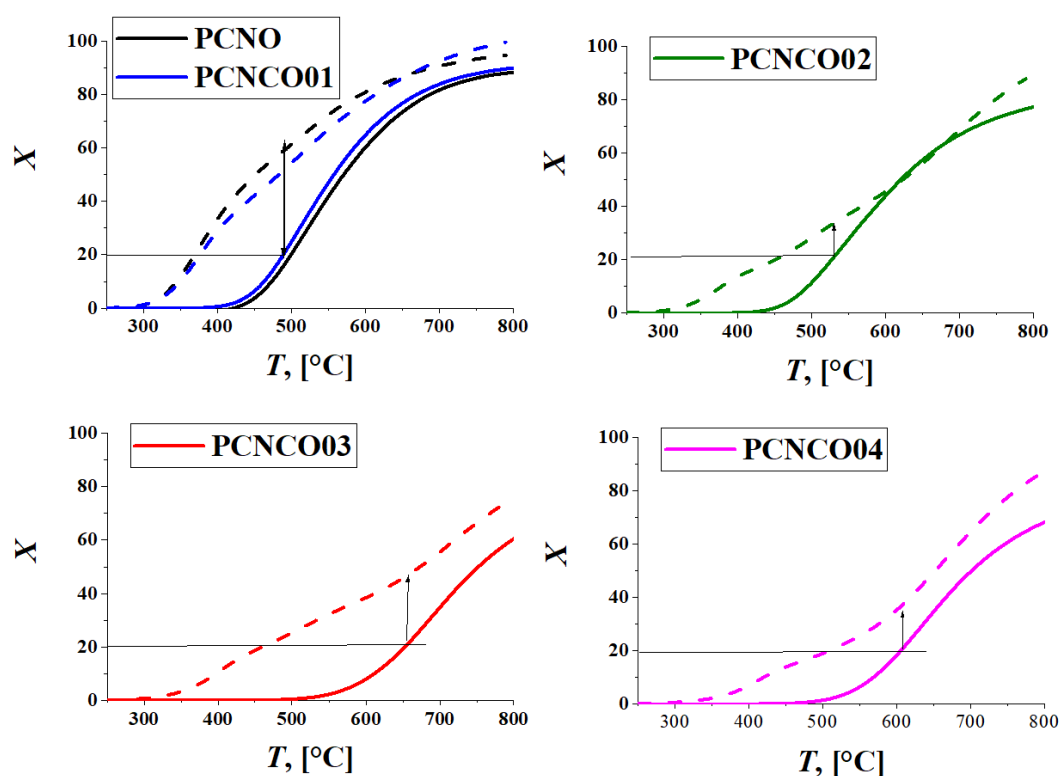


Figure 4 The dynamic extent of exchange for the $\text{Pr}_{1.6}\text{Ca}_{0.4}\text{Ni}_{1-y}\text{Cu}_y\text{O}_{4+6}$ samples during TPIE $^{18}\text{O}_2$ (solid lines, this work) and C^{18}O_2 (dashed lines, from Ref. [41]) runs.

Table 3 – The oxygen tracer diffusion coefficient (D^*) values at 700 K and their effective activation energies (E_a) for various oxygen forms (with the fraction of θ) according to the TPIE C^{18}O_2 data modeling [41].

Sample	O_{fast}			O_{middle}			O_{slow}		
	θ , [%]	$D^* \cdot 10^{11}$, [cm ² /s]	E_a , [kJ/mol]	θ , [%]	$D^* \cdot 10^{13}$, [cm ² /s]	E_a , [kJ/mol]	θ , [%]	$D^* \cdot 10^{15}$, [cm ² /s]	E_a , [kJ/mol]
PCNO	77	3.6	160	23	0.6	160	0	–	–
PCNCO01	40	2.3	160	30	0.5	160	30	(0.1 ÷ 1)	160
PCNCO02	15	4.2	160	25	(0.2 ÷ 2)	160	60	1.0	160
PCNCO03	20	1.7	160	20	(0.1 ÷ 1)	160	60	0.7	160
PCNCO04	13	0.7	160	7	(0.1 ÷ 1)	160	80	1.1	160

subsequent calculations. On the other hand, the $\alpha_G(T)$ dependencies for the PCNO and PCNCO01 samples can be described using a uniform model [29] with a single diffusion coefficient within the sample bulk. This suggests no limiting effect of oxygen diffusion for the PCNO and PCNCO01 samples. For other samples, the $\alpha_G(T)$ dependencies cannot be described by a uniform model; therefore, oxygen bulk diffusion must be taken into account. The limiting effect of diffusion manifests exclusively at elevated isotope substitution extents for the PCNCO03 and PCNCO04 samples. In contrast, for the PCNCO02 sample, diffusion begins to limit the process almost immediately upon the onset of isotope exchange.

Figure 5 demonstrates the dependencies of the ^{18}O atomic (α_G) and $^{16}\text{O}^{18}\text{O}$ molecular (f_{34}) fractions in O_2 acquired for the PCNO samples. The f_{34} dependence is determined not only by the surface exchange rate, but

also by the exchange mechanism. Generally, there are two types of heteroexchange R^1 (Equations 6 and 7) and R^2 (Equations 8–10) [26, 28, 29, 37, 38, 44–46]. As illustrated in Figure 5, Model 1 is incapable of explaining the f_{34} dependence, regardless of whether R^1 or R^2 is considered as the exchange mechanism. Employing the two-step model (Model 2, see Section 3.2 for details) allows a successful description of both $\alpha_G(T)$ and $f_{34}(T)$ dependencies using the R^2 -type of exchange mechanism for all samples (Figure 3, upper and lower images, respectively).

The calculations demonstrated that the limiting effect of the $\text{O}_{ADS} \leftrightarrow \text{O}_S$ step occurs only for the PCNO and PCNCO01 samples. In the case of PCNCO02 sample at the onset of isotope exchange, the $\text{O}_2^{GAS} \leftrightarrow \text{O}_{ADS}$ step is limiting, then oxygen diffusion in the oxide bulk is limiting. For the PCNCO03 and PCNCO04 samples, the

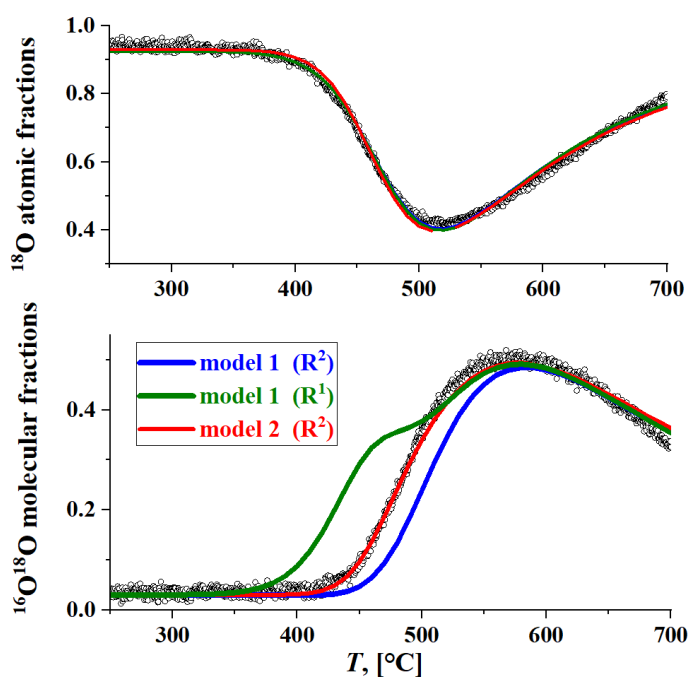


Figure 5 Temperature-programmed isotope exchange of oxygen with $^{18}\text{O}_2$ in the flow reactor for the $\text{Pr}_{1.6}\text{Ca}_{0.4}\text{NiO}_{4+\delta}$ sample. Points – experiment, lines – description using various models.

$\text{O}_2^{\text{GAS}} \leftrightarrow \text{O}_{\text{ADS}}$ step is mainly limiting, except for high oxygen isotope substitution extents. The calculated values of the surface exchange rates for the $\text{O}_2^{\text{GAS}} \leftrightarrow \text{O}_{\text{ADS}}$ (R^2) and $\text{O}_{\text{ADS}} \leftrightarrow \text{O}_S$ (K) steps are given in Table 4 and Figure 6(a). It is noteworthy that the effective activation energy values for all $\text{Pr}_{1.6}\text{Ca}_{0.4}\text{Ni}_{1-\gamma}\text{Cu}_\gamma\text{O}_{4+\delta}$ ($\gamma = 0.0$ – 0.4) samples remain constant within the estimation error range, 180 kJ/mol (Table 4). The oxygen surface

exchange rate is known to depend on various factors, including the frequency of exchange attempts, the surface coverage by adsorbed oxygen species, oxygen vacancies, and other oxygen forms; the enthalpies and entropies of oxygen adsorption, incorporation, and charge transfer [57–59]. The experimental findings suggest that the incorporation of Cu does not appear to exert a substantial influence on these enthalpies and entropies. However, it may have an impact on the contribution of the oxygen surface form, as evidenced by the XPS data (Table 2) [39]. Additionally, there is the possibility that the attempt frequency may be affected.

In order to compare the samples studied with the other samples and make correlations according to the ALS model, the oxygen surface exchange values (k^*) should be calculated. As follows from the calculations (Figure 6(b)), the samples possess high k^* values ($\sim 10^{-7}$ – 10^{-5} cm/s at 700 °C), which is comparable or even exceeding the values for other first-order RP phases [26, 28, 29, 32, 34–36].

Table 4 – The values of the oxygen surface exchange rates (R^2 , K) at 700 K and their effective activation energies ($E_a(R, K)$) according to the TPIE $^{18}\text{O}_2$ data modeling.

Sample	R^2 , [$\mu\text{mol}/(\text{m}^2 \cdot \text{s})$]	K , [$\mu\text{mol}/(\text{m}^2 \cdot \text{s})$]	$E_a(R, K)$, [kJ/mol]
PCNO	0.8	0.3	180(\pm 0.3)
PCNCO01	0.8		
PCNCO02	0.1	Not limited	
PCNCO03	0.01		
PCNCO04	0.03		

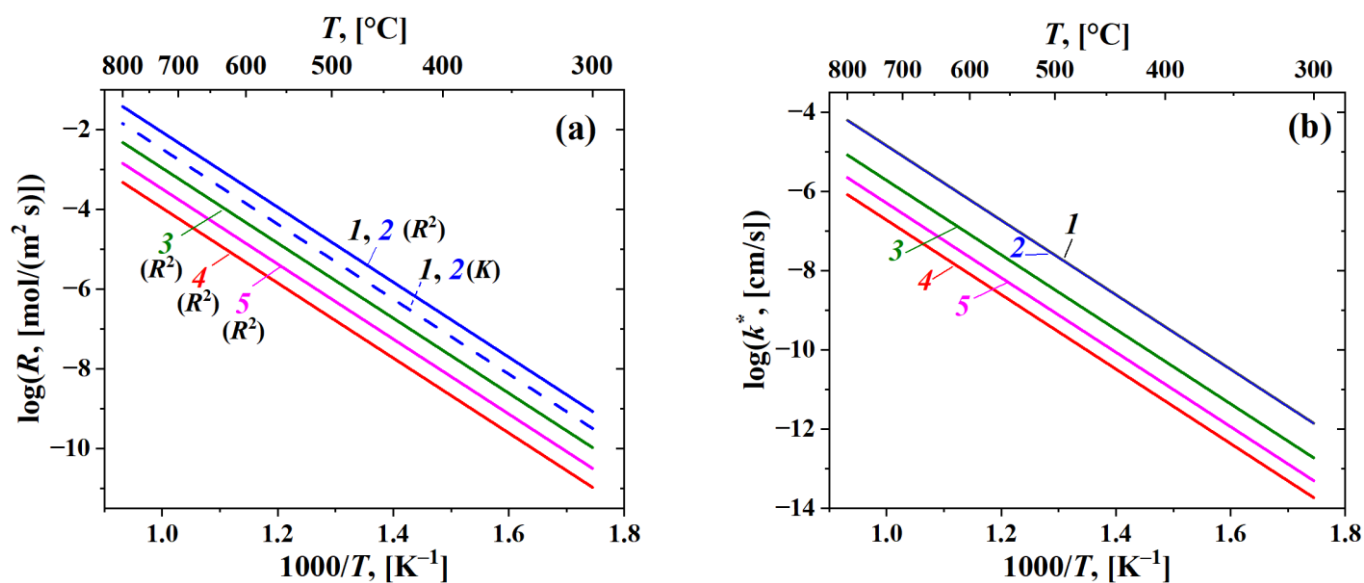


Figure 6 – Arrhenius plots for oxygen surface exchange rates (a) and constants (b) according to the TPIE $^{18}\text{O}_2$ in the flow reactors for the $\text{Pr}_{1.6}\text{Ca}_{0.4}\text{Ni}_{1-\gamma}\text{Cu}_\gamma\text{O}_{4+\delta}$ samples, $\gamma = 0.0$ (1), 0.1 (2), 0.2 (3), 0.3 (4) and 0.4 (5).

4.3. Correlation with electrochemical properties

Electrochemical impedance measurements and detailed analysis of the electrode performance were carried out in the authors' previous works [39, 40]. The polarization resistance values, R_p , for the single-layer $\text{Pr}_{1.6}\text{Ca}_{0.4}\text{Ni}_{1-y}\text{Cu}_y\text{O}_{4+\delta}$ electrodes on the SDC electrolyte were calculated as 1.88, 1.05, 1.54, 1.65 and $0.91 \Omega \cdot \text{cm}^2$ at 700°C for $y = 0.0, 0.1, 0.2, 0.3$ and 0.4 , respectively. The effective activation energy values, found from the reciprocal R_p temperature dependencies, are 130, 120, 120, 120 and 90 kJ/mol for $y = 0.0, 0.1, 0.2, 0.3$ and 0.4 (Figure 7). The variation of the effective activation energy of R_p with the Cu content, while the effective activation energies of D^* and k^* are almost constant (Tables 3 and 4) may be due to the variation of the oxygen content (Equation 26) with temperature as shown by the TGA data [39, 41] as well possible deviations from the ALS model [60–62].

While analyzing the correlations of polarization resistance with oxygen content, diffusion coefficient, and surface exchange constant within the framework of the ALS model [20, 21, 28, 34, 47], the trends of decreasing R_p with increasing the $(D^*k^*)^{0.5}$ and δ values were observed (Figure 8).

The R_p and δ dependencies on the Cu content are non-monotonous, while $(D^*k^*)^{0.5}$ gradually decreases with increasing the Cu content. Especially, there are

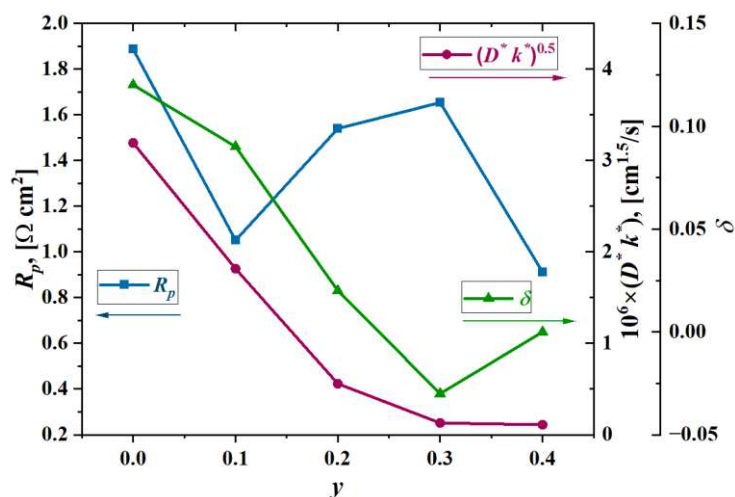
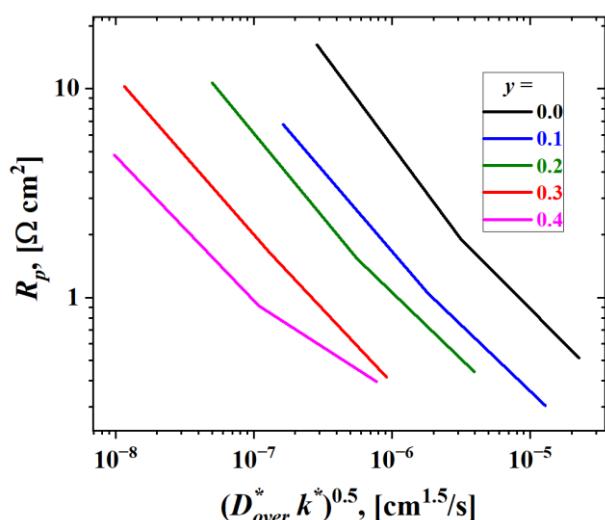


Figure 8 – Correlation of polarization resistance, oxygen overstoichiometry, tracer diffusion coefficient and surface exchange constant for the $\text{Pr}_{1.6}\text{Ca}_{0.4}\text{Ni}_{1-y}\text{Cu}_y\text{O}_{4+\delta}$ series ($y = 0.0$ – 0.4).

5. Conclusions

The present study demonstrates the effect of the Cu content in the $\text{Pr}_{1.6}\text{Ca}_{0.4}\text{Ni}_{1-y}\text{Cu}_y\text{O}_{4+\delta}$ series on the oxygen surface reactivity. The temperature-programmed isotope

exchange with $^{18}\text{O}_2$ studies demonstrate that the oxygen surface exchange occurs via the R^2 -type of mechanism, i.e., two-atomic heteroexchange. For some samples, the limiting effect of the adsorbed oxygen incorporation into the oxide surface is shown. The oxygen surface exchange

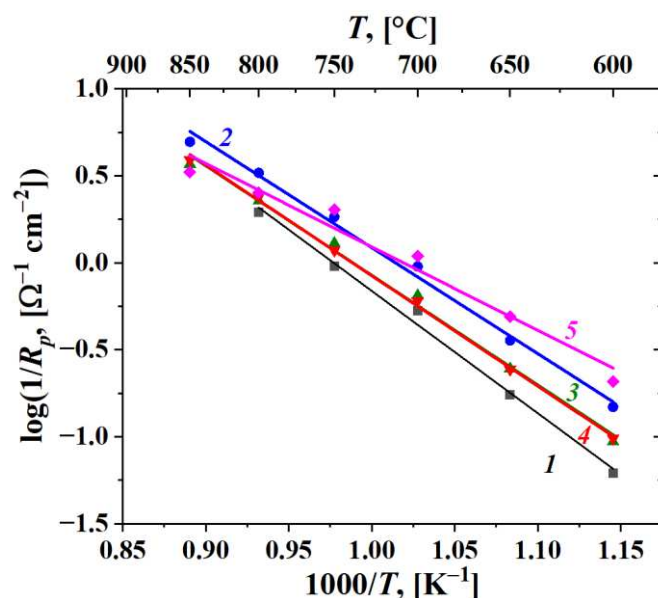


Figure 7 – Arrhenius plots for the reciprocal polarization resistance of the $\text{Pr}_{1.6}\text{Ca}_{0.4}\text{Ni}_{1-y}\text{Cu}_y\text{O}_{4+\delta}$ electrodes without collector layer, $y = 0.0$ (1), 0.1 (2), 0.2 (3), 0.3 (4) and 0.4 (5) [39].

rate tends to decrease with increasing the Cu content, which can be explained by a decrease in the highly-mobile interstitial oxygen content and mobility. The exception for the $\text{Pr}_{1.6}\text{Ca}_{0.4}\text{Ni}_{0.6}\text{Cu}_{0.4}\text{O}_{4+\delta}$ sample exhibiting higher oxygen surface exchange rate values compared to the $\text{Pr}_{1.6}\text{Ca}_{0.4}\text{Ni}_{0.7}\text{Cu}_{0.3}\text{O}_{4+\delta}$ sample can be explained by the combined effect of the sample surface properties and/or the oxygen content. Nevertheless, all samples possess high oxygen surface exchange constant values ($\sim 10^{-7}$ – 10^{-5} cm/s at 700 °C) that are comparable or even exceeding the values for other first-order RP phases and is very attractive for practical application as SOFC/SOE air electrodes. The correlations of the electrode performance and materials' oxygen kinetics are demonstrated.

Supplementary materials

No supplementary materials are available.

Funding

Oxygen isotope exchange studies and mathematical modeling of the results were performed in the framework of the budget projects of the Boreskov Institute of Catalysis, Siberian Branch, Russian Academy of Sciences (projects FWUR-2024-0033 and FWUR-2024-0038, respectively). Synthesis of the materials and their characterization was done using the equipment of the Shared Access Center "Composition of compounds" in the framework of the State Assignment for the Institute of High Temperature Electrochemistry, Ural Branch, Russian Academy of Sciences (project No 125020501556-0).

Acknowledgments

The authors are grateful to Tatiana Zhulanova (IHTE UB RAS) for the synthesis of the materials, Sergey Pikalov (IMET UB RAS), Dr. Elena Filonova (UrFU) for the XRD characterizations and calculations and Yulia Fedorova (BIC SB RAS) for the measurement of true and bulk density of the samples.

Author contributions

Vladislav Sadykov: Conceptualization, Supervision, Writing – Review & Editing.

Ekaterina Sadovskaya: Data curation, Formal Analysis, Methodology, Visualization, Writing – Original draft.

Nikita Ereemeev: Investigation, Visualization, Writing – Original draft.

Elena Pikalova: Conceptualization, Formal Analysis, Supervision, Visualization, Writing – Review & Editing.

Conflict of interest

The authors declare no conflict of interest.

Additional information

Scopus author IDs:

Vladislav Sadykov, Scopus ID [7006677003](https://orcid.org/0009-0001-7006-6770), [57200684813](https://orcid.org/0009-0001-5720-0684);

Ekaterina Sadovskaya, Scopus ID [57202034821](https://orcid.org/0009-0001-5720-2034), [57204295192](https://orcid.org/0009-0001-5720-4295);

Nikita Ereemeev, Scopus ID [55645818400](https://orcid.org/0009-0001-5564-5818);

Elena Pikalova, Scopus ID [16242376500](https://orcid.org/0009-0001-1624-2376).

Websites:

Federal Research Center Boreskov Institute of Catalysis SB RAS <https://en.catalysis.ru/>;

Institute of High-Temperature Electrochemistry UB RAS, <https://ihte.ru/>.

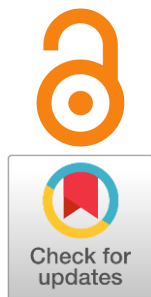
References

- Peng C, Han X, Mabaleha S, Kwong P, et al., Recent advances in perovskite air electrode materials for protonic solid oxide electrochemical cells, *Energy Environ. Sci.*, **18**(10) (2025) 4555–4595. <https://doi.org/10.1039/D5EE00983A>
- Liu F, Su Z, Li H, Wang Q, et al., Status and prospects of electrode materials for symmetrical solid oxide fuel cells: A concise review, *Ionics*, **31**(5) (2025) 3877–3894. <https://doi.org/10.1007/s11581-025-06182-8>
- Chen X, Tan Y, Li Z, Liu T, et al., Advanced air electrodes for reversible protonic ceramic electrochemical cells: A comprehensive review, *Adv. Mater.*, (2025) 2418620. <https://doi.org/10.1002/adma.202418620>
- Kang HC, Park YJ, Baek SY, Kim J, et al., Recent breakthroughs in cathode of protonic ceramic fuel cells: Materials, functionalization, and future perspectives, *InfoMat*, (2025) e70025. <https://doi.org/10.1002/inf2.70025>
- Zhu Y, Tang Z, Yuan L, Li B, et al., Beyond conventional structures: Emerging complex metal oxides for efficient oxygen and hydrogen electrocatalysis, *Chem. Soc. Rev.*, **54**(2) (2025) 1027–1092. <https://doi.org/10.1039/D3CS01020A>
- Samreen A, Ali MS, Huzaifa M, Ali N, et al., Advancements in perovskite-based cathode materials for solid oxide fuel cells: A comprehensive review, *Chem. Rec.*, **24**(1) (2024) e202300247. <https://doi.org/10.1002/tcr.202300247>
- Jiang S, Zheng X, Sun W, Toward advanced fuel electrodes for high-performance proton-conducting ceramic cells, *Adv. Energy Mater.*, **15**(4) (2025) 2403745. <https://doi.org/10.1002/aenm.202403745>
- Yatoo MA, Skinner SJ, Ruddlesden-Popper phase materials for solid oxide fuel cell cathodes: A short review, *Mater. Today: Proc.*, **56**(6) (2022) 3747–3754. <https://doi.org/10.1016/j.matpr.2021.12.537>
- Qu J, Wang X, Zhang J, Shi H, et al., Gùtì yǎnghuà wù ránliào diànchí Ruddlesden-Popper xíng yǎnghuà wù yángjī de yánjiū jìnzhǎn [Recent advances in Ruddlesden-Popper oxide for solid oxide fuel cells anodes], *J. Funct. Mater. / Gongneng Cailiao*, **55**(9) (2024) 9078–9086. Chinese. <https://doi.org/10.3969/j.issn.1001-9731.2024.09.010>

10. Zhu S, Fan F, Li Z, Wu J, et al., Metal exsolution from perovskite-based anodes in solid oxide fuel cells, *Chem. Commun.*, **60(9)** (2024) 1062–1071. <https://doi.org/10.1039/D3CC05688K>
11. Tong J, Zhang P, Zhuang F, Zheng Y, et al., Mixed-conducting ceramic membrane reactors for hydrogen production, *React. Chem. Eng.*, **9(12)** (2024) 3072–3099. <https://doi.org/10.1039/D4RE00372A>
12. Lu Q, Papaioannou EI, Development of mixed ionic and electronic conducting materials for gas separation membranes: A critical overview, *Chem. Eng. J.*, **496** (2024) 153791. <https://doi.org/10.1016/j.cej.2024.153791>
13. Kwon Y-I, Nam GD, Lee G, Choi S, et al., Recent progress and challenges in mixed ionic–electronic conducting membranes for oxygen separation, *Adv. Energy Sustain. Res.*, **3(11)** (2022) 2200086. <https://doi.org/10.1002/aesr.202200086>
14. Wang P, Liao L, Chu H, Xie Y, et al., Recent advances in Ruddlesden–Popper phase-layered perovskite Sr_2TiO_4 photocatalysts, *Nanomaterials*, **15(1)** (2025) 20. <https://doi.org/10.3390/nano15010020>
15. Zhou C, Guo W, Fan J, Shi N, et al., Recent advances and future perspectives of Ruddlesden–Popper perovskite oxides electrolytes for all-solid-state batteries, *Infomat*, **6(8)** (2024) e12563. <https://doi.org/10.1002/inf2.12563>
16. Neelakandan M, Dhandapani P, Ramasamy S, Duraisamy R, et al., A review on perovskite oxides and their composites as electrode materials for supercapacitors, *RSC Adv.*, **15(21)** (2025) 16766–16791. <https://doi.org/10.1039/D5RA01950H>
17. Desta HG, Gebresslassie G, Zhang J, Lin B, et al., Enhancing performance of lower-temperature solid oxide fuel cell cathodes through surface engineering, *Prog. Mater. Sci.*, **147** (2025) 101353. <https://doi.org/10.1016/j.pmatsci.2024.101353>
18. Yang G, Jung W, Ahn S-J, Lee D, Controlling the oxygen electrocatalysis on perovskite and layered oxide thin films for solid oxide fuel cell cathodes, *Appl. Sci.*, **9(5)** (2019) 1030. <https://doi.org/10.3390/app9051030>
19. Sadykov VA, Ereemeev NF, Shlyakhtina AV, Pikalova EYu, Advances in alternative metal oxide materials of various structures for electrochemical and catalytic applications, *Int. J. Hydrogen Energy*, **94** (2024) 179–208. <https://doi.org/10.1016/j.ijhydene.2024.11.072>
20. Adler SB, Factors governing oxygen reduction in solid oxide fuel cell cathodes, *Chem. Rev.*, **104(10)** (2004) 4791–4844. <https://doi.org/10.1021/cr020724o>
21. Adler SB, Lane JA, Steele BCH, Electrode kinetics of porous mixed-conducting oxygen electrodes, *J. Electrochem. Soc.*, **143(11)** (1996) 3554–3564. <https://doi.org/10.1149/1.1837252>
22. Yang S, Liu G, Li W, Sabolsky EM, et al., Ab initio study on the effect of A-site doping on the stability, equilibrium volume, activation energy barrier, and oxygen diffusivity in $\text{La}_{2-x}\text{A}_x\text{NiO}_{4+\delta}$, *Int. J. Hydrogen Energy*, **119** (2025) 235–251. <https://doi.org/10.1016/j.ijhydene.2025.03.239>
23. Li X, Benedek NA, Enhancement of ionic transport in complex oxides through soft lattice modes and epitaxial strain, *Chem. Mater.*, **27(7)** (2015) 2647–2652. <https://doi.org/10.1021/acs.chemmater.5b00445>
24. Lee D, Lee HN, Controlling oxygen mobility in Ruddlesden–Popper oxides, *Materials*, **10(4)** (2017) 368. <https://doi.org/10.3390/ma10040368>
25. Sadykov V, Pikalova E, Ereemeev N, Shubin A, et al., Oxygen transport in Pr nickelates: Elucidation of atomic-scale features, *Solid State Ionics*, **344** (2020) 115155. <https://doi.org/10.1016/j.ssi.2019.115155>
26. Ananyev MV, Tropin ES, Eremin VA, Farlenkov AS, et al., Oxygen isotope exchange in $\text{La}_2\text{NiO}_{4\pm\delta}$, *Phys. Chem. Chem. Phys.*, **18(13)** (2016) 9102–9111. <https://doi.org/10.1039/C5CP05984D>
27. Grobovoy IS, Kolchugin AA, Pikalova EYu, Suntsov AYU, Defect formation and thermodynamic properties of Ca-doped La_2NiO_4 oxides, *Inorg. Chem. Commun.*, **179(2)** (2025) 114823. <https://doi.org/10.1016/j.inoche.2025.114823>
28. Pikalova EYu, Guseva EM, Filonova EA, Short review on recent studies and prospects of application of rare-earth-doped $\text{La}_2\text{NiO}_{4+\delta}$ as air electrodes for solid oxide electrochemical cells, *Electrochem. Mater. Technol.*, **2(4)** (2024) 20232025. <https://doi.org/10.15826/elmattech.2023.2.025>
29. Sadykov V, Pikalova E, Sadovskaya E, Shlyakhtina A, et al., Design of mixed ionic-electronic materials for permselective membranes and solid oxide fuel cells based on their oxygen and hydrogen mobility, *Membranes*, **13(8)** (2023) 698. <https://doi.org/10.3390/membranes13080698>
30. Amov G, Skinner SJ, Recent developments in Ruddlesden–Popper nickelate systems for solid oxide fuel cell cathodes, *J. Solid State Electrochem.*, **10(8)** (2006) 538–546. <https://doi.org/10.1007/s10008-006-0127-x>
31. Yin B, Li Y, Sun N, Ji X, et al., Activating ORR and OER in Ruddlesden–Popper based catalysts by enhancing interstitial oxygen and lattice oxygen redox reactions, *Electrochim. Acta*, **370** (2021) 137747. <https://doi.org/10.1016/j.electacta.2021.137747>
32. Li W, Guan B, Zhang X, Yan J, et al., New mechanistic insight into the oxygen reduction reaction on Ruddlesden–Popper cathodes for intermediate-temperature solid oxide fuel cells, *Phys. Chem. Chem. Phys.*, **18(12)** (2016) 8502–8511. <https://doi.org/10.1039/C6CP00056H>
33. Gu X-K, Nikolla E, Design of Ruddlesden–Popper oxides with optimal surface oxygen exchange properties for oxygen reduction and evolution, *ACS Catal.*, **7(9)** (2017) 5912–5920. <https://doi.org/10.1021/acscatal.7b01483>
34. Pikalova EYu, Sadykov VA, Filonova EA, Ereemeev NF, et al., Structure, oxygen transport properties and electrode performance of Ca-substituted Nd_2NiO_4 , *Solid State Ionics*, **335** (2019) 53–60. <https://doi.org/10.1016/j.ssi.2019.02.012>
35. Kolchugin AA, Pikalova EYu, Bogdanovich NM, Bronin DI, et al., Structural, electrical and electrochemical properties of calcium-doped lanthanum nickelate, *Solid State Ionics*, **288** (2016) 48–53. <https://doi.org/10.1016/j.ssi.2016.01.035>
36. Tropin E, Ananyev M, Porotnikova N, Khodimchuk A, et al., Oxygen surface exchange and diffusion in $\text{Pr}_{1.75}\text{Sr}_{0.25}\text{Ni}_{0.75}\text{Co}_{0.25}\text{O}_{4\pm\delta}$, *Phys. Chem. Chem. Phys.*, **21(9)** (2019) 4779–4790. <https://doi.org/10.1039/C9CP00172G>
37. Muzykantov VS, Popovski VV, Borekov GK, Kinetika izotopnogo obmena v sisteme molekulyarnyi kislorod – tvyodyi okisel [Kinetics of isotope exchange in molecular oxygen – solid oxide system], *Kinet. Katal.*, **5(4)** (1964) 624–629. Russian.

38. Muzykantov VS, Popovski VV, Boreskov GK, Kinetika i mekhanizm izotopnogo obmena v sisteme molekulyarnyi kislorod – tvyodyi okisel [Kinetics and mechanism of isotope exchange in molecular oxygen – solid oxide system]. In: Problemy kinetiki i kataliza, T.12 [Problems in kinetics and catalysis, V.12]. Moscow: Nauka, 1968. pp. 155–159. Russian.
39. Pikalova E, Zhulanova T, Ivanova A, Tarutin A, et al., Optimized $\text{Pr}_{1.6}\text{Ca}_{0.4}\text{Ni}_{1-y}\text{Cu}_y\text{O}_{4+\delta}$ phases as promising electrode materials for CeO_2 - and $\text{BaCe}(\text{Zr})\text{O}_3$ -based electrochemical cells, *Ceram. Int.*, **50(20C)** (2024) 40476–40491. <https://doi.org/10.1016/j.ceramint.2024.06.048>
40. Zhulanova T, Filonova E, Ivanova A, Russkikh O, et al., Control physicochemical and electrochemical properties of $\text{Pr}_{1.6}\text{Ca}_{0.4}\text{Ni}_{0.6}\text{Cu}_{0.4}\text{O}_{4+\delta}$ as a prospective cathode material for solid oxide cells through the synthesis process, *Solid State Sci.*, **156** (2024) 107671. <https://doi.org/10.1016/j.solidstatesciences.2024.107671>
41. Sadykov V, Ereemeev N, Sadovskaya E, Zhulanova T, et al., Impact of calcium and copper co-doping on the oxygen transport of layered nickelates: A case study of $\text{Pr}_{1.6}\text{Ca}_{0.4}\text{Ni}_{1-y}\text{Cu}_y\text{O}_{4+\delta}$ and a comparative analysis, *Chim. Tech. Acta*, **11(4)** (2024) 202411411. <https://doi.org/10.15826/chimtech.2024.11.4.11>
42. Sadykov VA, Sadovskaya EM, Uvarov NF, Methods of isotopic relaxations for estimation of oxygen diffusion coefficients in solid electrolytes and materials with mixed ionic-electronic conductivity, *Russ. J. Electrochem.*, **51(5)** (2015) 458–467. <https://doi.org/10.1134/S1023193515050109>
43. Sadykov V, Sadovskaya E, Bobin A, Kharlamova T, et al., Temperature-Programmed C^{18}O_2 SSITKA for powders of fast oxide-ion conductors: Estimation of oxygen self-diffusion coefficients, *Solid State Ionics*, **271** (2015) 69–72. <https://doi.org/10.1016/j.ssi.2014.11.004>
44. Boreskov GK, Muzykantov VS, Investigation of oxide-type oxidation catalysts by reactions of oxygen isotopic exchange, *Ann. N. Y. Acad. Sci.*, **213(1)** (1973) 137–170. <https://doi.org/10.1111/j.1749-6632.1973.tb51065.x>
45. Muzykantov VS, Isotopic studies of dioxygen activation on oxide catalysts for oxidation: Problems, results and perspectives, *React. Kinet. Catal. Lett.*, **35(1–2)** (1987) 437–447. <https://doi.org/10.1007/BF02062178>
46. den Otter MW, Boukamp BA, Bouwmeester HJM, Theory of oxygen isotope exchange, *Solid State Ionics*, **139(1–2)** (2001) 89–94. [https://doi.org/10.1016/S0167-2738\(00\)00801-8](https://doi.org/10.1016/S0167-2738(00)00801-8)
47. Huang Q-A, Hui R, Wang B, Zhang J, A review of AC impedance modeling and validation in SOFC diagnosis, *Electrochim. Acta*, **52(28)** (2007) 8144–64. <https://doi.org/10.1016/j.electacta.2007.05.071>
48. Ananyev MV, Kurumchin EK, Porotnikova NM, Effect of oxygen nonstoichiometry on kinetics of oxygen exchange and diffusion in lanthanum-strontium cobaltites, *Russ. J. Electrochem.*, **46(7)** (2010) 789–797. <https://doi.org/10.1134/S1023193510070128>
49. Aguadero A, Alonso J, Escudero M, Daza L, Evaluation of the $\text{La}_2\text{Ni}_{1-x}\text{Cu}_x\text{O}_{4+\delta}$ system as SOFC cathode material with 8YSZ and LSGM as electrolytes, *Solid State Ionics*, **179(11–12)** (2008) 393–400. <https://doi.org/10.1016/j.ssi.2008.01.099>
50. Sakai M, Wang C, Okiba T, Soga H, et al., Thermal analysis of structural phase transition behavior of $\text{Ln}_2\text{Ni}_{1-x}\text{Cu}_x\text{O}_{4+\delta}$ ($\text{Ln} = \text{Nd}, \text{Pr}$) under various oxygen partial pressures, *J. Therm. Anal. Calorim.*, **135(5)** (2019) 2765–2774. <https://doi.org/10.1007/s10973-018-7621-0>
51. Popovski VV, Boreskov GK, Kinetika izotopnogo obmena molekulyarnogo kisloroda s kislorodom poverkhnosti okislov zheleza, kobal'ta, nikelya i medi [Kinetics of isotope exchange of molecular O_2 with oxide surfaces of Fe, Co, Ni, and Cu], *Kinet. Catal.*, **1(4)** (1960) 566–575. Russian.
52. Kaluzhskikh MS, Kazakov SM, Mazo GN, Istomin SYA, et al., High-temperature crystal structure and transport properties of the layered cuprates Ln_2CuO_4 , $\text{Ln} = \text{Pr}, \text{Nd}$ and Sm , *J. Solid State Chem.*, **184(3)** (2011) 698–704. <https://doi.org/10.1016/j.jssc.2011.01.035>
53. Miyoshi S, Furuno T, Sangoanruang O, Matsumoto H, et al., Mixed conductivity and oxygen permeability of doped Pr_2NiO_4 -based oxides, *J. Electrochem. Soc.*, **154(1)** (2007) B57–B62. <https://doi.org/10.1149/1.2387103>
54. Yashima M, Yamada H, Nuansaeng S, Ishihara T, Role of Ga^{3+} and Cu^{2+} in the high interstitial oxide-ion diffusivity of Pr_2NiO_4 -based oxides: design concept of interstitial ion conductors through the higher-valence d^{10} dopant and Jahn-Teller effect, *Chem. Mater.*, **24(21)** (2012) 4100–4113. <https://doi.org/10.1021/cm3021287>
55. Biesinger MC, Payne BP, Lau LWM, Gerson A, et al., X-ray photoelectron spectroscopic chemical state quantification of mixed nickel metal, oxide and hydroxide systems, *Surf. Interface Anal.*, **41(4)** (2009) 324–332. <https://doi.org/10.1002/sia.3026>
56. Vincent Crist B. Handbooks of Monochromatic XPS Spectra: Volume 2: Commercially Pure Binary Oxides and a few Common Carbonates and Hydroxides: John Wiley & Sons; 2000. 27 p.
57. Ishihara T. Perovskite oxide for solid oxide fuel cells. New York: Springer Science + Business Media, LLC; 2009. 302 p.
58. Kilner JA, De Souza RA, Fullarton IC, Surface exchange of oxygen in mixed conducting perovskite oxides, *Solid State Ionics*, **86–88(2)** (1996) 703–709. [https://doi.org/10.1016/0167-2738\(96\)00153-1](https://doi.org/10.1016/0167-2738(96)00153-1)
59. De Souza RA, Limits to the rate of oxygen transport in mixed-conducting oxides, *J. Mater. Chem. A*, **5(38)** (2017) 20334–20350. <https://doi.org/10.1039/C7TA04266C>
60. Abd Aziz AJ, Baharuddin NA, Lim BH, Characterization of oxygen diffusion and catalytic behavior of composite materials in solid oxide fuel cells using the non-destructive Adler-Lane-Steele method, e-J, *Nondestructive Testing*, **29(6)** (2024). <https://doi.org/10.58286/30310>
61. Endler-Schuck C, Joos J, Niedrig C, Weber A, et al., The chemical oxygen surface exchange and bulk diffusion coefficient determined by impedance spectroscopy of porous $\text{La}_{0.58}\text{Sr}_{0.4}\text{Co}_{0.2}\text{Fe}_{0.8}\text{O}_{3-\delta}$ (LSCF) cathodes, *Solid State Ionics*, **269** (2015) 67–79. <https://doi.org/10.1016/j.ssi.2014.11.018>
62. Goel V, Cox D, Barnett SA, Thornto K, Simulation of the electrochemical impedance in a three-dimensional, complex microstructure of solid oxide fuel cell cathode and its application in the microstructure characterization, *Front. Chem.*, **9** (2021) 627699. <https://doi.org/10.3389/fchem.2021.627699>

Progress in infiltration technology applied to air electrodes with proton-conducting electrolyte backbones

Elena Pikalova^{a*}Received: 7 June 2025
Accepted: 19 June 2025
Published online: 27 June 2025DOI: [10.15826/elmattech.2025.4.054](https://doi.org/10.15826/elmattech.2025.4.054)

Lowering the operating temperature of solid-state energy devices to 500–700 °C has driven an increased attention being paid to protonic ceramic cells (PCCs) due to several advantages they offer such as low activation energy for proton diffusion, fuel flexibility, higher power efficiency provided by the absence of fuel dilution at the anode, as well as enhanced potential for lower housing and stacking costs. However, a significant challenge for fuel/electrolysis cells based on proton-conducting electrolytes is the performance of air electrodes for efficient oxygen reduction and water splitting reactions. The infiltration of catalysts into porous backbone layers has been demonstrated to be a highly effective method for the fabrication of highly active and durable PCC electrodes. This Focus Review summarizes the achievements in the application of the infiltration technique to the formation of air electrodes with proton-conducting electrolyte/composite backbones modified with various catalysts as a promising simple and cost-effective way to eliminate electrode/electrolyte mismatch issues and provide significant performance enhancement.

keywords: proton conducting fuel cells, air electrode, proton-conducting electrolytes, infiltration technique, electrolyte backbone, composite backbone, enhanced performance, durability

© 2025, the Authors. This article is published in open access under the terms and conditions of the Creative Commons Attribution (CC BY) license (<http://creativecommons.org/licenses/by/4.0/>).

1. Introduction

Protonic ceramic cells (PCCs) represent a promising class of electrochemical devices for the efficient clean energy [1, 2]. Compared to conventional solid state devices, these cells offer several advantages, including low activation energy for proton diffusion, fuel flexibility, ability to operate in the intermediate temperature range (500–700 °C), and the elimination of the need for expensive noble metals as electrocatalysts [3]. Moreover, PCCs exhibit wide-ranging application prospects for the production of hydrogen and valuable chemical products at intermediate temperatures [2].

Despite the promising potential of PCCs, their widespread implementation faces difficulties due to the challenge of insufficient electrochemical performance. Lowering the operation temperature and the presence of water in the air electrode, which can partly block the active sites for ORR, cause large overpotentials. This

factor may contribute greatly to the deterioration of the whole cell performance. Therefore, the absence of highly active and durable cathodes, which compromise both cell efficiency and long-term stability, can be considered as the main obstacle for the PCC commercialization. Overcoming these limitations will help to unlock full potential of PCCs and accelerate their integration into the global energy landscape [4–7].

Air electrode materials developed for PCCs currently encompass electronic conductors, oxide-ionic – electronic conductors, protonic – electronic conductors, triple-conducting oxides, as well as composite electrodes [4, 8–11]. Modifying the electrodes in PCCs to meet the requirements for the PCCs efficient operation at decreased temperatures involves optimizing their material composition, microstructure, and surface properties to enhance performance. The guide on chemical and structural design of oxygen electrodes, including those for PCCs, was represented recently by Tarutin et al. [12]. Several advanced techniques were proposed to improve PCCs' air electrode activity: methods to change the electrode composition under the influence of external

^a: Institute of High Temperature Electrochemistry UB RAS, Yekaterinburg 620137, Russia

* Corresponding author: e.pikalova@ihte.ru

conditions with the formation of heterogenic catalysts [13–15], creation of nanocomposites with extended triple phase boundary (TPB) using infiltration [16–20], infiltration/reactive sintering [21], and a one-pot method [22–24], surface modification by spin-coating [25], electrospinning [26], atomic layer deposition [27], and pulsed laser deposition [28], and others.

The infiltration-based modification of the electrodes offers three primary advantages. First, it is an efficient approach to enhance the electrocatalytic activity of PCFC electrodes at low cost by applying an appropriate catalyst without utilization of complicated equipment. Secondly, due to lowering the sintering temperature of the electrodes, it facilitates the utilization of a diverse array of active materials that are otherwise incompatible with conventional electrodes due to their high reactivity with other PCFC components. Finally, this approach facilitates the creation of nanoscale and/or nanostructured composite electrodes, which will enhance the performance of existing PCFC systems due to the increased TPBs. Due to all these outlined advantages, the infiltration technique, which appeared in 90th of XX century [29], is still attracting enhanced attention among other methods of the electrode nanoengineering [30, 31].

The majority of the studies conducted in Russia were focused on enhancing the electrocatalytic activity of SOFC air electrodes through the infiltration of Pr-based catalysts [32–38]. A limited number of studies have focused on the infiltration of air electrodes in PCFCs [16, 39, 40]. Nevertheless, as far as the interest to PCCs is constantly growing, so more studies to improve their performance using infiltration are underway.

Recent reviews have elucidated the specifics and demonstrated advantages of the infiltration technique for

the SOFC air electrodes [41–49]. Impregnation/infiltration technique was mentioned as promising in the reviews on the PCFCs electrodes, including composites [4, 8, 44, 50–53]. However, to the best of our knowledge, there is no any specific review on the infiltration of the PCFCs air electrodes. Therefore, the present review is focused on infiltration technology applied to air electrodes for PCCs, particularly, for the electrodes with proton-conducting electrolyte backbones.

The review begins with an outline of the primary principles of PCC operation and the range of available PCC electrode materials. It emphasizes the application of the infiltration technique, which is a simple, cost-effective method of fabricating nanoscale composite electrodes with an extended triple phase boundary. Next, it transitions to its main subject: nanocomposite air (oxygen) electrodes based on proton-conducting electrolyte/composite backbones, considering infiltration of various catalysts, influence of microstructure, loading level and sintering conditions on the electrode performance.

2. Proton ceramic cells: specifics of operation and requirements for oxygen electrodes

The main advantage of proton ceramic fuel cells (PCFCs) over other known classes of fuel cells based on solid-state electrolytes is the effective operation at reduced temperatures due to the higher mobility and lower activation energy of protons compared to oxide ions in this range [54, 55]. In addition, the water in the electrochemical reaction is generated at the PCFC cathode, eliminating fuel dilution at the anode (Figure 1). In the case of the electrolysis cell, no separation of the output gas mixture is required. PCECs differ from PCFCs

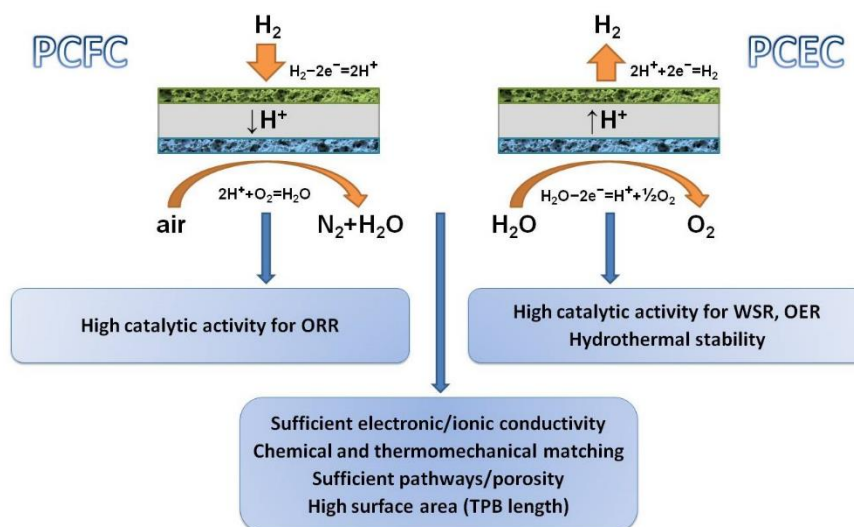


Figure 1 Principles of the operation of electrochemical devices based on a proton-conducting electrolyte: fuel cell (PCFC) and electrolysis cell (PCEC). The diagram shows common and specific requirements for air electrodes for these devices.

not only by polarization polarity applied to the cells, but also unconventional conditions of highly humidified atmospheres.

The main role of the PCCs oxygen electrodes is to provide the sites for the electrochemical reactions – the oxygen reduction reactions (ORR)/oxygen evolution reactions (OER), and the water-splitting reactions (WSR). Sufficient electronic conductivity is also necessary for the stable current collection. Functionality of oxygen electrodes in PCFC and PCEC defines specific requirements for these electrodes. Requirements for air electrodes for PCFCs include high electronic/ionic conductivity and stability under working conditions ($500\text{--}700\text{ }^{\circ}\text{C}$, $10^{-5} \leq p\text{O}_2 \text{ (atm)} \leq 0.21$, in the presence of H_2O and CO_2), high catalytic activity for ORR, thermomechanical and chemical compatibility with electrolyte and interconnect materials, good adhesion to the electrolyte, and suitable porosity for gas exchange across the electrode bulk and between the electrode/electrolyte interface. High catalytic activity for OER and WSR, as well as hydrothermal stability, are important for PCEC's air electrodes [9, 12].

3. Major types of oxygen electrodes for PCCs

The following major types of oxygen electrodes can be distinguished: pure electronic conductors (ECs) that only allows electron (e^-) to conduct, mixed ionic (O^{2-}) and electronic (e^-) conductors (MIECs), mixed protonic (H^+) and electronic (e^-) conductors (MPECs), and triple-conducting oxides that allows all types of charge carriers – ionic (H^+) and (O^{2-}), and electronic (e^-) (TIECs) [4, 5, 50, 56, 57].

Figure 2 shows specifics of the ORR reaction in PCFCs in dependence on the oxygen electrode conducting nature. The first studies concerning PCFCs reported the use of ECs, such as Pt [58–63] or traditional Sr-doped LaMnO_3 (LSM) [64, 65] as a cathode. However, Pt is not

preferred for practical applications due to its high cost. Moreover, Pt in contact with a proton-conducting electrolyte is found to show significant polarization losses caused by the limited number of reaction sites, localized mainly at the cathode/electrolyte interface [66, 67]. LSM electrodes require specific modifications to be effectively used in PCFCs at reduced operating temperatures as well [68–70].

Generally, mixed ionic and electronic conductors (MIECs) are considered as the most promising cathode materials for the next-generation SOFCs with reduced operating temperatures due to their excellent catalytic activities for ORR through the extension of the electrochemically active sites to the entire surface of the cathode [71–73]. Due to their high conducting properties, fast oxygen kinetics, and excellent catalytic activity, conventional and double perovskites, layered and misfit layered phases were considered as air electrode materials in contact with proton-conducting electrolytes [51, 74–78]. However, in PCFCs, the electrochemically active sites of a MIEC air electrode are also limited to the triple-phase boundary (TPB) which is the electrode/electrolyte interface due to their poor proton-conducting properties.

MPECs are proton-conducting materials that exhibit enhanced electronic conductivity when doped with transition metals or multivalent elements, such as Co, Fe, Pr, and Bi. These materials have been investigated for their potential application as PCC oxygen electrodes and proton-conducting membrane materials [50, 77, 79–83]. The effectiveness of MPECs can be attributed to their triple phase boundary, which may prolong the water evolution reaction at the electrode surface. However, MPECs have not received sufficient attention from researchers because of poor outcomes between electronic and proton conduction upon doping and poor catalytic activity to ORR due to a relatively lower content

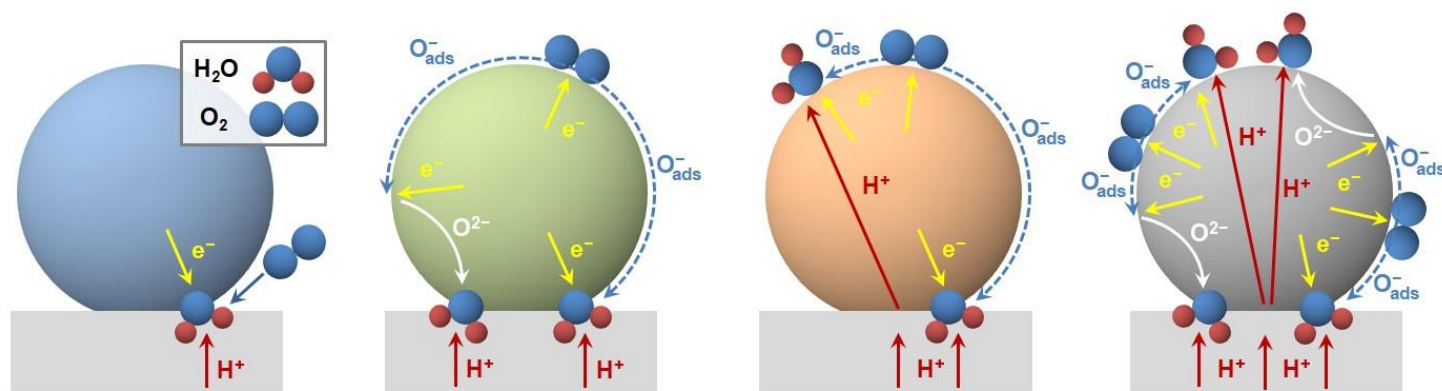


Figure 2 Schematic representation of the ORR reaction in oxygen electrodes with a different type of conductivity (from the left to the right) ECs, MIECs, MPECs and TIECs on a proton-conducting electrolyte.

of transition metals in solid solutions compared to MIECs.

Accordingly, for highly efficient PCFCs, the active sites of the cathode should be extended to the bulk sites by facilitating O^{2-} electroreduction rates and electrochemical activities for H^+ and e^- in the cathode material. Triple ionic-electronic conductors (TIECs) meet these requirements [8, 84–92]. However, it worth noting that the term "triple-conducting" signifies that all three partial conductivities (electronic, oxygen-ionic, and protonic) have to be comparable. This objective has not been attained by contemporary state-of-the-art electrode systems within the intermediate temperature range, as sufficient mobility/concentration of protons is only achieved at temperatures as low as 200–400 °C [11, 51].

Examples of the composition of the electrodes with different conducting nature and performance (peak power density, PPD) of the anode-supported PCFCs at 600 °C are presented in Table 1. The lines' color in the table is related with colors of electrodes shown in the schematic in Figure 2.

Composite electrodes enable the extension of the TPB from the electrolyte/cathode interface to the entire cathode bulk. Typically, in the research of PCC composite oxygen electrodes, a catalyst (ECs, MIECs) is mixed with a proton conductive electrolyte material to realize triple-

Table 1 – Air electrode materials for PCFCs. PPDs of the cells with doped $BaCe(Zr)O_3$ membranes of different thicknesses are presented at 600 °C.

Composition	Electrolyte: thickness	PPD	Ref
$La_{0.8}Sr_{0.2}MnO_{3-\delta}$	^a BCY15 : 20	180	[65]
$LaNi_{0.4}Fe_{0.6}O_{3-\delta}$	^b BZY : 20	46	[93]
$Sm_{0.5}Sr_{0.5}CoO_{3-\delta}$	^c BCZYZn : 20	246	[94]
$La_{0.6}Sr_{0.4}Co_{0.2}Fe_{0.8}O_{3-\delta}$	^d BZCY7 : 55	235	[95]
$Ba_{0.5}Sr_{0.5}Co_{0.8}Fe_{0.2}O_{3-\delta}$	BCY10 : 20	390	[96]
$Lm_{.2}Sr_{0.8}NiO_{4+\delta}$ ($Lm = La/Pr$)	BZCY7 : 10	223/ 127	[97]
$Ca_3Co_4O_{9+\delta}$	^e BZCY : 25	246	[98]
$SmBaCuCoO_{5+\delta}$	BZCY7 : 30	152	[99]
$BaCo_{0.7}Fe_{0.22}Sc_{0.08}O_{3-\delta}$	BZCY7 : 10	591	[100]
$BaCe_{0.5}Fe_{0.3}Bi_{0.2}O_{3-\delta}$	BZCY7 : 25	362	[101]
$NdBa_{0.5}Sr_{0.5}Co_{1.5}Fe_{0.5}O_{5+\delta}$	BZCY7 : 15	690	[84]
$PrBa_{0.5}Sr_{0.5}Co_{1.5}Fe_{0.5}O_{5+\delta}$	^f BZCYYb : 18	600	[92]
$BaCo_{0.4}Fe_{0.4}Zr_{0.1}Y_{0.1}O_{3-\delta}$	BZCY7 : 40	669	[102]
$BaCe_{0.1}Zr_{0.2}Y_{0.1}Fe_{0.6}O_{3-\delta}$	BCZYYb : 30	75	[89]
$BaZr_{0.2}Y_{0.2}Fe_{0.6}O_{3-\delta}$	BZY : 20	175	[103]

^a – $BaCe_{0.85}Y_{0.15}O_{3-\delta}$;

^b – $BaZr_{0.8}Y_{0.2}O_{3-\delta}$;

^c – $BaCe_{0.5}Zr_{0.3}Y_{0.16}Zn_{0.04}O_{3-\delta}$;

^d – $BaZr_{0.1}Ce_{0.7}Y_{0.2}O_{3-\delta}$;

^e – $BaCe_{0.5}Zr_{0.3}Y_{0.2}O_{3-\delta}$;

^f – $BaCe_{0.5}Zr_{0.3}Y_{0.1}Yb_{0.1}O_{3+\delta}$.

conductivity [10, 11, 39, 104–106]. Reducing thermomechanical mismatch between cathode and electrolyte is also among the advances of the composite electrodes, as the most of electrode materials exhibit significantly higher thermal expansion coefficients (TECs) compared to those of current proton-conducting electrolytes, which may led to adhesion issues even on the stage of the electrode fabrication [107]. Meanwhile, other types of composite cathodes, composed of a cathode catalyst and an oxygen ion conductor, have been proposed [108–112]. Oxygen ion conductors are excellent oxygen reduction catalysts; therefore, the oxygen reduction and oxide ion migration capabilities can be enhanced in the composite.

Triple-phase conducting composite cathodes, comprising both proton and oxygen conducting electrolytes as well as EC or MIEC [113, 114] or composites containing MIEC and TIEC [115], combining all the advantages of the composite component and diminishing drawbacks, have recently gained attention as promising electrode candidates for PCCs.

The critical aspect of the PCC design pertains to the chemical compatibility of the electrode and electrolyte materials, which influence not only power characteristics but also long-term stability. The problem with chemical interaction in composite electrodes can be resolved by decreasing sintering temperature of the electrodes or eliminating of the sintering step [41, 42, 116–121].

4. Infiltration technique as an advanced tool for the electrode modification

The infiltration-based modification of the electrodes facilitates the creation of nanoscale surface layers and/or nanostructured composite electrodes, which may enhance the performance of existing PCFC systems due to the increased TPBs, as schematically shown in Figure 3.

The lowering the sintering temperature of the electrodes, it facilitates the utilization of those electrode materials that are incompatible with proton-conducting

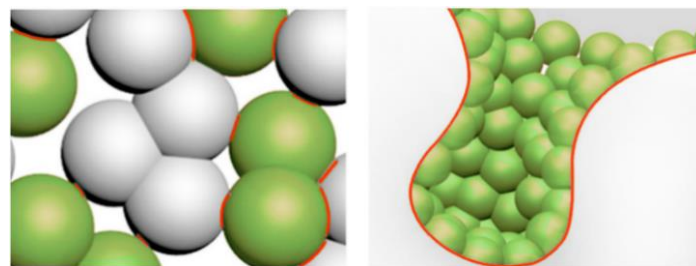


Figure 3 Schematic representation of a conventional composite (left) and a nanocomposite electrode (right) prepared using an infiltration technique. Red lines represent a triple phase boundary.

electrolytes due to their high chemical reactivity or/and a mismatch in thermal expansion properties [107].

The infiltration process typically includes several sequential steps: the preparation of a porous backbone, the preparation and introduction of a liquid precursor solution into the backbone structure, and the subsequent heat treatment, which may result in the formation of separate particles or films [44, 122], as it is shown in Figure 4.

Furthermore, each stage of the process requires the consideration of specific controllable parameters. At the initial stage, the following issues must be taken into account: the level and nature of the backbone conductivity and its microstructure, which is defined by the dispersity of the powders and the type of pore former used, as well as the formation method and sintering conditions. The precursor solution preparation also presumes a number of the controllable parameters, such as the choice of solution media, chelating agents, and surfactants. The subsequent heat treatment step enables the production of nanosized particles of the material introduced by infiltration. The sintering temperature and dwelling time, which have a significant impact on the size, crystallinity, and grain growth of the particles are controllable parameters at this step.

Schematically, the most important controllable parameters for the infiltration process are shown in Figure 5.

According to the backbone conducting nature, considered in the previous section, several classes of PCCs electrodes, presented in literature can be distinguished: (a) porous electrolyte (proton-conducting, oxygen-ion conducting or composite) backbones with infiltrated electrocatalyst; (b) single-component electronic

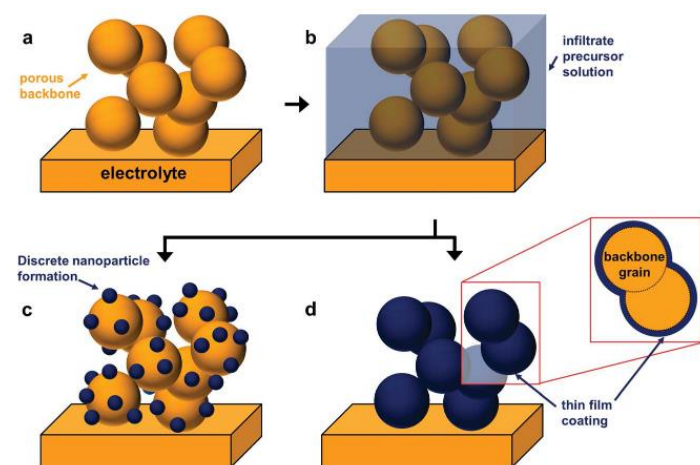


Figure 4 Schematic of infiltration: (a) backbone preparation; (b) infiltration with a precursor solution; and formation of the infiltrate after a sintering step represented by (c) separate particles or (d) films [122].

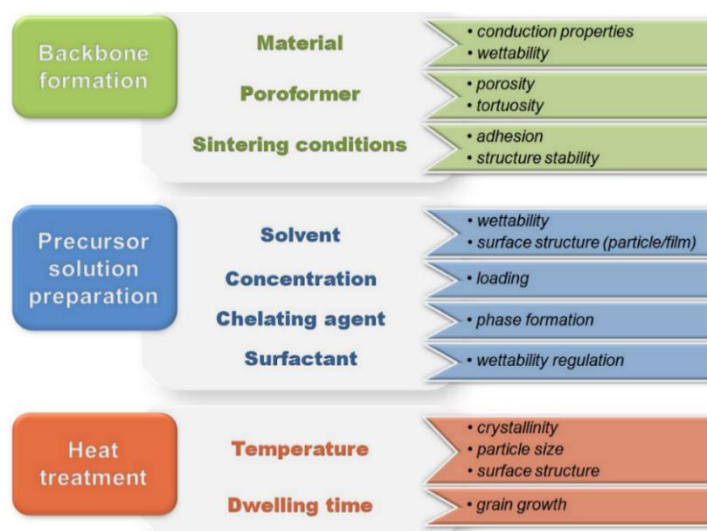


Figure 5 Controllable parameters of the infiltration process.

backbones; (c) single-component mixed ionic/protonic and electronic conducting (MIEC [123], MPECs) backbones; (d) triple-conducting backbone (TIECs) and (e) composite electrodes backbones.

Utilization of electrolyte backbones allows high sintering temperatures to ensure optimal adhesion and structural stability of the electrode. This method eliminates issues related to the electrode/electrolyte mismatching. The size of infiltrated catalyst particles can be controlled at a nanometer level due to low calcination temperatures, allowing for the generation of numerous reactive zones, which can enhance the electrode performance significantly. Moreover, the proton-conducting backbone allows the TPB to be extended to the electrode volume.

5. PCC air electrodes fabricated by infiltrating electrolyte-containing backbones

5.1. Infiltration of the proton-conducting electrolyte backbones

In the pioneering studies, the electrodes with a proton conducting backbone infiltrated with ECs/MIECs were considered [124–127]. Wu et al. [125] fabricated nanocomposites on the base of a $\text{BaCe}_{0.8}\text{Sm}_{0.2}\text{O}_{2.9}$ (BCS) backbone infiltrated with $\text{Sm}_{0.5}\text{Sr}_{0.5}\text{CoO}_{3-\delta}$ (SSC@BCS) by introducing a Sm, Sr, Co nitrate water solution with the addition of glycine (1 : 2) to the BCS porous backbone, pre-sintered at 1100–1400 °C. Here, a designation SSC@BCS has been introduced to discern composites prepared by infiltration from those prepared by mixing (SSC-BCS). The lowest polarization resistance, R_p , of about $0.21 \Omega \cdot \text{cm}^2$ at 600 °C, was achieved with the BCS backbone sintered at 1100 °C, the SSC loading level of 55 wt. %, and the SSC infiltrate sintering temperature of

800 °C. Figure 6(a) demonstrates the BCS backbone with various loading levels. It is seen that at 55 wt. % loading, the particles grow (to about 250 nm) and form a well-connected network over the BCS backbone, which results in the superior electrode performance. For the conventional SSC-BCS composite electrode with the same SSC content and sintering temperature of 1100 °C, R_p was $0.63 \Omega \cdot \text{cm}^2$ at 600 °C. The peak power densities (PPDs) of the anode supported cell with the BCS electrolyte of 70 μm in thickness were 239 and 307 $\text{mW} \cdot \text{cm}^{-2}$ at 700 °C for SSC-BCS and SSC@BCS cathodes, respectively. The cell ohmic resistance, R_{ohmic} , contributed the most to the total cell resistance (0.676 and 0.691 $\Omega \cdot \text{cm}^2$ at 700 °C

for the cell with the impregnated and conventional composite electrode, respectively) due to high electrolyte thickness.

Following this study, Zhao et al. [124] investigated SSC@BaZr_{0.1}Ce_{0.7}Y_{0.2}O_{3- δ} (BZCY) electrodes, obtained by infiltrating a Sr, Sm, Co water-alcohol nitrate solution with the addition of Pluronic P123 as a surfactant and urea as a chelating agent. A single cell with a BaCe_{0.7}In_{0.3}O_{3- δ} (BCI) electrolyte (~18 μm) and such a nanocomposite cathode with 75 wt. % SSC loading demonstrated a PPD of 491 $\text{mW} \cdot \text{cm}^{-2}$ at 700 °C, respectively. The short-term durability test (1000 min) of the cell based on the infiltrated SSC@BZCY under a constant current density

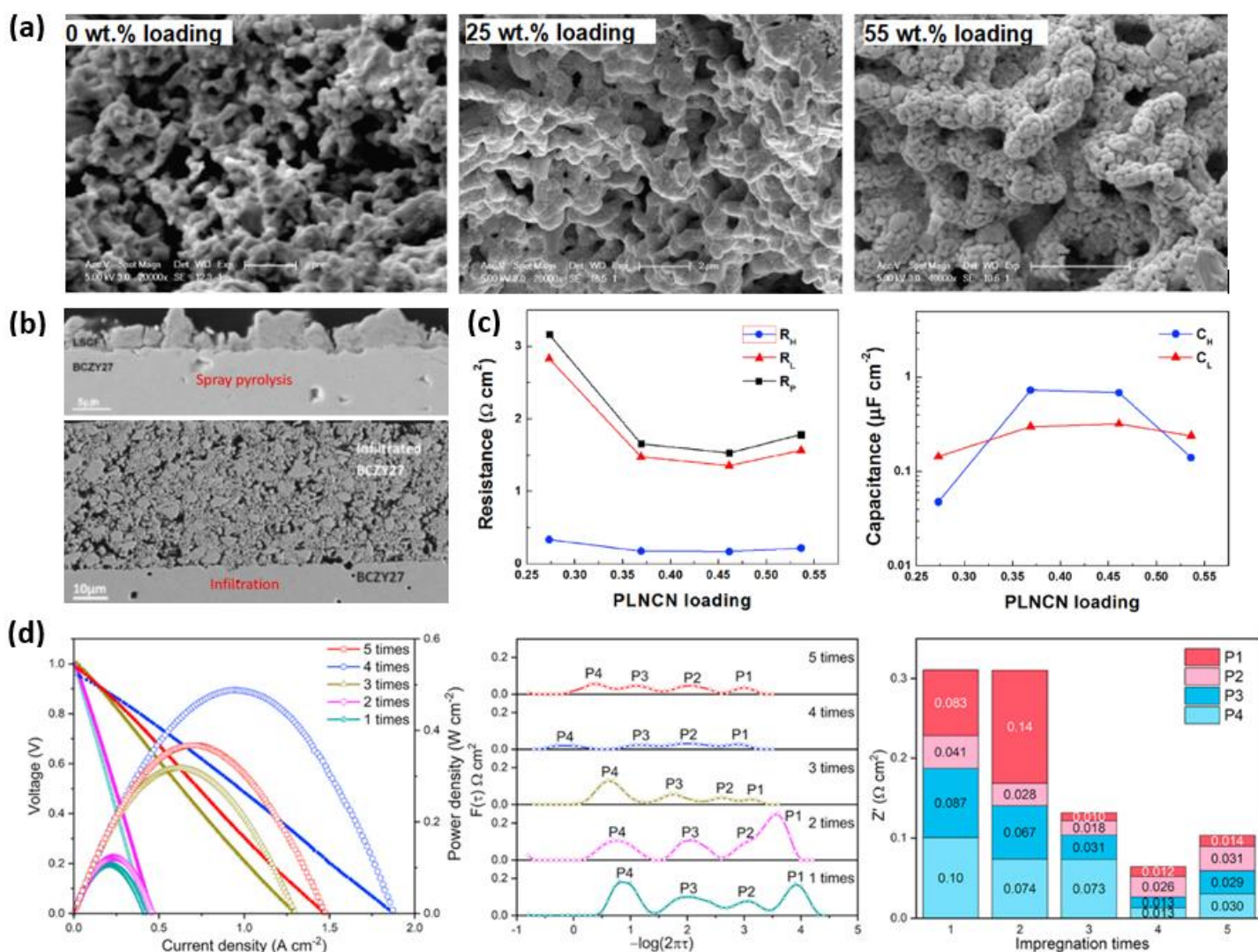


Figure 6 (a) SEM images of the infiltrated BCS-based electrode with 0, 25 and 55 wt. % of the SSC loading (Reconstructed using the data [125]); (b) Microstructure of LSFC electrode prepared by spray pyrolysis and 12 cycles infiltrated LSCF@BZCY electrode (constructed using the data [127]); (c) Polarization resistance (left) and characteristic capacitances (right), obtained for the PLNCN-infiltrated BZCY-based electrodes with various loading (at 600 °C) (Reconstructed using the data [130]); (d) Electrochemical performance and derived DRT of single-cells at 750 °C with PBC-BZCYYb composite cathodes made with varying number of times of PBC impregnation into BZCYYb backbone (from the left to the right): $I-V$ - P curves using humidified hydrogen; DRT of single-cells derived from EIS and (contributions of anode and cathode processes to polarization resistance of single-cells (Reconstructed using the data [131])).

of $200 \text{ mA} \cdot \text{cm}^{-2}$ at $600 \text{ }^\circ\text{C}$ showed excellent microstructural and performance stability of the infiltrated electrode.

Da'as et al. [128], using infiltration of a classical electron-conducting $\text{La}_{0.8}\text{Sr}_{0.2}\text{MnO}_{3-\delta}$ (LSM) to $\text{BaZr}_{0.8}\text{Y}_{0.2}\text{O}_{2.9}$ cathode backbone obtained promising performance 109, 154, and $200 \text{ mW} \cdot \text{cm}^{-2}$ at 500, 550, and $600 \text{ }^\circ\text{C}$, respectively, compared to 2, 6, and $14 \text{ mW} \cdot \text{cm}^{-2}$ at 500, 550, and $600 \text{ }^\circ\text{C}$ for the cell with the conventional LSM-BZY composite electrode, sintered at $1100 \text{ }^\circ\text{C}$. Such a drastic difference in the performance was due to some reasons. First, TPB for the infiltrated electrode was significantly enhanced, and second, decreasing the sintering temperature of the LSM@BZY electrode allowed elimination of the chemical interaction between the components, which is known to be significant at $1100 \text{ }^\circ\text{C}$ [107]. At 500 and $600 \text{ }^\circ\text{C}$, the R_{ohmic}/R_p of the cell with the impregnated electrode were 0.63/3.32 and 0.41/0.64 $\Omega \cdot \text{cm}^2$, respectively. It is also worth noting that to implement the infiltration process, the authors used an advanced scalable inject printing technique, widely used for infiltration YSZ-based cells [129].

Ricote et al. [127] initiated a comparative study of the microstructure and performance of $\text{La}_{0.58}\text{Sr}_{0.4}\text{Co}_{0.2}\text{Fe}_{0.8}\text{O}_{3-\delta}$ (LSCF) cathodes deposited on BZCY by infiltration in 4 (2.5 wt. % loading) and 12 infiltration cycles (~ 7 wt. % loading) and those obtained by spray pyrolysis. Single-phase LSCF was obtained after final sintering at $700 \text{ }^\circ\text{C}$ for 2 h for all the cells. The area specific resistances (ASR) of 0.61 $\Omega \cdot \text{cm}^2$ at $600 \text{ }^\circ\text{C}$, respectively, were obtained for the spray-pyrolyzed LSCF cathode on BZCY in dry and humidified air [127]. Corresponding polarization resistances of 0.63 $\Omega \cdot \text{cm}^2$ and 0.98 $\Omega \cdot \text{cm}^2$ were measured for 12 cycles infiltrated LSCF@BZCY. Analysis of the electrochemical impedance spectra collected between $450 \text{ }^\circ\text{C}$ and $600 \text{ }^\circ\text{C}$ in air with varying $p(\text{H}_2\text{O})$ revealed that the charge transfer contribution was the lowest for the backbone-infiltrated cathode while the oxygen dissociation/adsorption contribution was the lowest for the spray-pyrolyzed cathode. The electrochemical properties are correlated to the cathodes' microstructure (Figure 6(b)). The spray-pyrolyzed LSCF cathode was between 2 and 6 μm thick with the presence of ridges. LSCF@BZCY cathodes were 35–40 μm thick, however, as the infiltrated LSCF did not percolate through the entire thickness, therefore, only the LSCF in contact with the current collector acted as cathode, which explains its relatively low activity.

Shimada [132] enhanced the performance of the LSCF-based cathode for the anode-supported PCFC with a

$\text{BaZr}_{0.1}\text{Ce}_{0.7}\text{Y}_{0.1}\text{Yb}_{0.1}\text{O}_{3-\delta}$ (BZCYYb) electrolyte using a combined approach. First, a submicron porous BZCYYb electrolyte layer was formed on the surface of the dense electrolyte. Second, this layer was impregnated with LSCF-BZCYYb fine particulates, yielding a three-dimensionally extended TPB region. PPD at $700 \text{ }^\circ\text{C}$ exceeded $1 \text{ W} \cdot \text{cm}^{-2}$ and remained high even at lower operating temperatures, i.e., 1.05, 0.81, 0.57, 0.38, and $0.24 \text{ W} \cdot \text{cm}^{-2}$ at 700, 650, 600, 550, and $500 \text{ }^\circ\text{C}$, respectively.

Ye et al. [133], studying the performance of anode-supported tubular reversible cells with a thin-film $\text{CaZr}_{0.9}\text{In}_{0.1}\text{O}_{3-\delta}$ (CZI) electrolyte established the optimal loading level of $\text{La}_{0.6}\text{Sr}_{0.4}\text{CoO}_{3-\delta}$ (LSC)@CZI air electrode as 50 wt. %. At $800 \text{ }^\circ\text{C}$, the current density of $182 \text{ mA} \cdot \text{cm}^{-2}$ at 1.3 V was obtained, while the observed PPD value for the optimized cell was $110 \text{ mW} \cdot \text{cm}^{-2}$. Taking into account that the TEC of CZI materials is about $3 \times 10^{-6} \text{ K}^{-1}$, which is much lower than that of common air electrode materials, the infiltration technique to form a composite air electrode is a perspective (if not the only) way to avoid TEC mismatch. This strategy may be applied to construct cells with novel, recently developed proton-conducting electrolytes with relatively low TEC values [134–138].

The study performed by Ricote group revealed that the presence of ionic conduction in a catalyst material infiltrated into a proton-conducting backbone is not necessary for a good performance. Instead, high electronic conductivity is a critical factor [126]. They fabricated BZCY-based electrodes infiltrated with LaCoO_3 (LC) electronic conductor. Single phased LC was formed after annealing in air at $600 \text{ }^\circ\text{C}$ for 2 h, with a particle size of 60–80 nm covering the BZCY grains (200 nm – 1 μm). The LC@BZCY performed 0.39 and 0.11 $\Omega \cdot \text{cm}^2$ at 500 and $600 \text{ }^\circ\text{C}$ respectively, in air ($p\text{H}_2\text{O} = 0.01 \text{ atm}$) was the lowest value reported for the PCFC cathodes. Contrarily, for the electrode obtained by the BZCY backbone infiltration with $\text{La}_2\text{NiO}_{4+\delta}$ (LN) with the same loading [139], despite high ionic conductivity and fast ionic transport characteristic for this catalyst, ASR values of 161.8, 29.3 and 3.7 $\Omega \cdot \text{cm}^2$ were measured at 500, 600 and $700 \text{ }^\circ\text{C}$, respectively. The main reason for that was supposed to be significantly lower electronic conductivity LN compared to Co-containing electrode materials ($\sim 65 \text{ S} \cdot \text{cm}^{-1}$ at $600 \text{ }^\circ\text{C}$ [140]).

Infiltration of a multi-doped RP phase with increased electronic conductivity to the proton-conducting backbone was reported by Li et al. [130]. The authors obtained a complex $(\text{Pr}_{0.9}\text{La}_{0.1})_2(\text{Ni}_{0.74}\text{Cu}_{0.2}\text{Nb}_{0.05})\text{O}_{4+\delta}$ phase through the infiltration of a water-based nitrate solution (0.1 M) with the addition of glycine as a chelating

agent to the porous BZCY backbone, pre-sintered at 1200 °C. After each infiltration step, the sample was calcined at 900 °C and characterized. The addition of ethanol to the water-based precursor solution allowed loading of 27.3, 36.9, 46.1, and 53.6 wt. % to be obtained after 1, 2, 3 and 4 infiltration cycles. With increasing the PLNCN content, the nanocoating microstructure changed from separate particles with their growth with formation of the uniform network (46.1 wt. %), and then to the thin film (53.6 wt. %). The lowest polarization resistance was found for the composite with 46.1 wt. % loading (Figure 6(c)). Analysis of the spectra have shown that low-frequency resistance, R_L , made a major contribution to R_p . According to the characteristic capacitance values, the 46.1 wt. % loaded sample has the fastest ORR dynamics. PPD of the single cell with a thin-film BCZY electrolyte (~18 μm) as high as $0.77 \text{ W} \cdot \text{cm}^{-2}$ was achieved at 700 °C by using the optimized PLNCN@BZCY cathode, demonstrating excellent performance stability during the test for 200 h at 600 °C.

Recently, Sun et al. [141], reported on the infiltrated $\text{La}_{1.2}\text{Sr}_{0.8}\text{NiO}_{4-\delta}$ (LSN)@ $\text{BaCe}_{0.68}\text{Zr}_{0.1}\text{Y}_{0.1}\text{Yb}_{0.1}\text{Cu}_{0.02}\text{O}_{3-\delta}$ (BCZYYbCu) oxygen electrode with the 42.2 wt. % loading as optimal for the application in a fuel electrode-supported reversible cell with the BCZYYCu electrolyte of 13 μm in thickness. PPD of $1220 \text{ mW} \cdot \text{cm}^{-2}$ and an electrolysis current density of $-3.02 \text{ A} \cdot \text{cm}^{-2}$ (at 1.3 V) at 700 °C were obtained, which was approximately 3 times higher than those reported for the reversible cell with conventional LSN-BCZYYbCu composite electrodes ($460 \text{ mW} \cdot \text{cm}^{-2}$ and $1.37 \text{ A} \cdot \text{cm}^{-2}$ at 700 °C, respectively [97]). Polarization resistances of infiltrated and conventional electrodes were 0.04 and $0.15 \Omega \cdot \text{cm}^2$ at 700 °C [97, 141].

In the past decade, layered double perovskite materials $L_n\text{BaCo}_2\text{O}_{5+\delta}$ ($L_n = \text{Pr}, \text{Eu}, \text{Nd}, \text{Sm}, \text{Gd}$) have been considered as potential cathodes for SOFCs due to their superior oxygen diffusion capability and excellent surface exchange kinetics [142]. A number of studies was devoted to the application of $\text{PrBaCo}_2\text{O}_{5+\delta}$ (PBC) as an oxygen electrode due to the excellent conductivity of $2000 \text{ S} \cdot \text{cm}^{-1}$ at 25 °C and $\sim 800 \text{ S} \cdot \text{cm}^{-1}$ at 500 °C in air with the chemical surface exchange coefficient (k_{chem}) and diffusion coefficient (D_{chem}) equal to $10^{-2} \text{ cm} \cdot \text{s}^{-1}$ and $5 \cdot 10^{-5} \text{ cm}^2 \cdot \text{s}^{-1}$, respectively. Cathodes with PBC infiltrated on $\text{Ce}_{0.9}\text{Gd}_{0.1}\text{O}_{1.95}$ (GDC) backbones demonstrated even lower polarization resistance compared to that of SSC@GDC (0.031 and $0.042 \Omega \cdot \text{cm}^2$ at 600 °C in air for 50 wt. % PBC and 50 wt. % SSC infiltrated cathodes, respectively) on the GDC electrolyte.

Liu et al. [131] prepared by infiltration PBC@BZCYYb nanocomposite cathodes for an anode-supported PCFC with a BZCYYb electrolyte of 30 μm in thickness. The optimal PBC loading in the composite cathode of 36 wt. % was obtained by 4 infiltration cycles. The results of the analysis of partial anode and cathode contributions using a DRT technique are shown in Figure 6(d). According to Wang [143], P1 typically corresponds to proton diffusion from the anode into the electrolyte, P2 to hydrogen adsorption/dissociation/proton formation in the anode, P3 to oxygen adsorption/dissociation/diffusion in the cathode and oxygen bulk diffusion in the anode, which was negligible here as BZCYYb is basically a proton conductor, and P4 to hydrogen transportation in anode pores. It is seen that the contribution of the processes occurred in the cathode to the total R_p of all the single-cells, represented by P3, was smaller than that of the processes occurred in the anode (P1, P2 and P4). This is different from the behavior of conventional SOFCs, where R_{Pa} is typically much smaller than R_{Pc} [35]. It is also noted that as the PBC impregnation was increased from 1 time to 4 times, R_{Pc} was decreased from 0.087 to $0.013 \Omega \cdot \text{cm}^2$, while the time constant τ_c was gradually increased from 0.001 to 0.010 s , suggesting that the amount of charge involved in the cathode reaction was greatly increased. At 700 °C, the cell attained $0.36 \text{ W} \cdot \text{cm}^{-2}$ PPD.

Bi et al. [144] studied performances of the anode-supported cell with a thin-film $\text{BaZr}_{0.8}\text{Y}_{0.2}\text{O}_{3-\delta}$ (BZY) electrolyte (15 μm) and SSC@BZY and PBC@BZY nanocomposite cathodes. R_p value for the SSC@BZY electrode was measured as $0.08 \Omega \cdot \text{cm}^2$ at 600 °C, which was significantly lower than those for the conventional SSC-SDC composite electrodes used with BZY-based cells ($1.30 \Omega \cdot \text{cm}^2$ [145]). The R_{ohmic} value, in which the major contribution comes from electrolyte resistance and interfacial contact resistance, was as low as $0.22 \Omega \cdot \text{cm}^2$ at 600 °C. Lowering the impregnated electrode sintering temperature down to 800 °C prevented the formation of a low conductive $\text{Sm}_2\text{Zr}_2\text{O}_7$ phase [146], thus decreasing the R_{ohmic} value. Due to excellent cathode performance, the PPD values of 249, 389, and $602 \text{ mW} \cdot \text{cm}^{-2}$ at 500, 550, and 600 °C, which was 1.44-fold higher compared to the highest BZY cell performance previously reported [147]. Even higher performance was obtained using the PBC@BZY cathode (292, 425, and $650 \text{ mW} \cdot \text{cm}^{-2}$ at 500, 550, and 600 °C). The authors noted the importance of the sintering conditions on the composite microstructure and, consequently, on the cell power output. Increasing the sintering temperature of PBC@BZY from 800 to 1200 °C resulted in a drastic decrease of PPD down to $8 \text{ mW} \cdot \text{cm}^{-2}$ at 600 °C.

5.2. Influence of backbone microstructure and conductivity

The microstructure, thickness, and conductivity of the electrolyte backbone along with the loading level, catalytic activity, and electronic conductivity of the infiltrated catalyst will influence the electrode performance and determine the ability to utilize the extended surface area.

The microstructure of the electrolyte backbone determines both the distribution of the infiltration solution and the size of the resulting infiltrated particles. In addition, the network of backbone particles also controls the transport of protons from/to the electrolyte, and oxygen and water molecules in the porous electrode. Therefore, a higher porosity may facilitate deep penetration and uniform distribution of the infiltrated catalyst, thereby increasing the active surface area and the TPB density. However, excessive porosity leads to a decrease in ionic conductivity due to a reduction in electrolyte material volume and to degrade the mechanical integrity of the electrolyte backbone. Low porosity, contrarily, may deteriorate impede catalyst infiltration and gas diffusion which could potentially limit the electrode performance. Numerous studies on the influence of the backbone porosity obtained by introduction of various pore formers combined with the choice of optimal sintering conditions variation, as well as application such methods as free-casting and electrospinning were performed for the conventional YSZ electrolyte backbones [148–151]. However, there are a few studies concerning optimization of proton-conducting backbones.

Strandbakke et al. [152] studied the influence of the backbone content and microstructural parameters on the performance of the $\text{Ba}_{0.5}\text{Gd}_{0.8}\text{La}_{0.7}\text{Co}_2\text{O}_{6-\delta}$ infiltrated nanocomposite BGLC@BZCY electrodes on the $\text{BaZr}_{0.7}\text{Ce}_{0.2}\text{Y}_{0.1}\text{O}_3$ (BZCY72) electrolyte. The authors used various deposition methods (spray coating (BBI and BB3 samples) and painting (BB2 sample)). Along with it, they added to the BB3 sample suspension (based on BZCY72) 1 wt. % NiO as a sintering additive, and activated charcoal (14 wt. %) were prepared by wet milling at 300 rpm for 2 h in a planetary mill with ZrO_2 jars and balls. The BBI sample suspension based on $\text{BaZr}_{0.2}\text{Ce}_{0.7}\text{Y}_{0.1}\text{O}_3$ (BZCY27) also contained 14 wt. % of charcoal. The spray coated samples were sintered in air at 1500 °C for 10 h (BBI) and 8 h (BB3). For BB2, BZCY72 mixed with 1 wt. % NiO was pre-calcined at 1050 °C for 24 h, then mixed with 1 wt. % ZnO and 50 wt. % graphite (Sigma Aldrich) as the pore former. After deposition, it was sintered at 1400 °C for

10 h. The SEM images of the prepared backbones are shown in Figure 7(a).

It is seen that the BBI and BB3 structures are macroscopically more porous, additionally, BBI structure has larger and more well-sintered grains, probably due to the higher Ce to Zr ratio compared to the BB3 sample. The grain size, or more precisely, the width and number of necks between the grains, grain boundaries, will have an effect on the proton transport in the backbone, determining to which thickness the backbone is utilized. Thus, it was supposed that BBI will facilitate better proton transport than BB2 and BB3, while the two latter will provide a potentially larger electrode surface area and electrolyte/electrode interface for the mass transfer and charge transfer reactions, respectively. These three backbones were infiltrated with a BGLC nitrate solution with several complexing agents (ammonium EDTA and triethanolamine (TEA)). Additionally, BGLC electrodes with the addition of various electrode inks were deposited directly on the electrolyte substrates. Among the three backbone electrodes, BB3 gives the lowest R_p , reaching 10 and $0.03 \Omega \cdot \text{cm}^2$ at 300 °C and 700 °C, respectively, in agreement with modelled from the spectra partial R_p for protonic charge carriers (Figure 7(b)). The lower exchange resistance for all backbone-based electrodes compared to the single-phase electrodes indicates that this microstructural design is preferable for a distributed reaction zone even for a triple-conducting material.

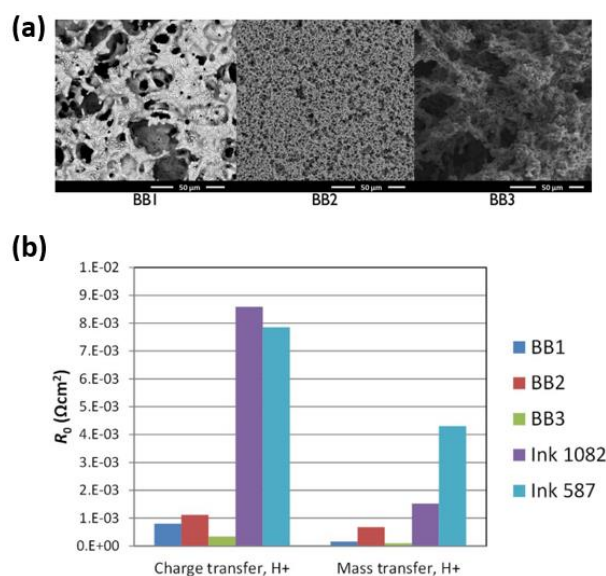


Figure 7 (a) SEM images of the BZCY27 (BBI) and BZCY72 (BB2, BB3) backbones formed on the BZCY72 electrolyte. Detailed description is provided in the text; (b) Exchange resistances for BBI–BB3 and for painted single-phase BGLC electrodes with various electrode inks (587 and 1082) (Reconstructed using the data [152]).

To determine the contribution of the properties of the protonic conductor to the composite electrode performance Shin et al. [153] used $\text{Ba}(\text{Ce}_{0.75}\text{Y}_{0.15})\text{O}_{3-\delta}$ (BCY), $\text{Ba}(\text{Ce}_{0.45}\text{Zr}_{0.30}\text{Y}_{0.15})\text{O}_{3-\delta}$ (BCZY), and $\text{Ba}(\text{Zr}_{0.75}\text{Y}_{0.15})\text{O}_{3-\delta}$ (BZY) porous backbones for the infiltrating active electrode materials such as $(\text{La}_{0.8}\text{Sr}_{0.2})\text{FeO}_{3-\delta}$ (LSF) for the cathode and $(\text{La}_{0.7}\text{Sr}_{0.3})\text{V}_{0.9}\text{O}_{3-\delta}$ (LSV) for the anode (15 vol. % of LSF or LSV loading, which was calculated using the loaded weight of component and the porosity of a porous backbone). Final sintering temperatures were 850 and 700 °C to produce single phases. The polarization resistance of LSF@BZY, LSF@BCZY, and LSF@BCY at 700 °C was 0.080, 0.055, and 0.049 $\Omega \cdot \text{cm}^2$. The BCY or BCZY backbone was shown to be more effective for enhancing the cathode performance, while BZY – for the anode. The cell with optimized electrodes, namely BCZY@LSF cathode and BZY@LSV anode, exhibited PPDs of 320 and 670 $\text{mW} \cdot \text{cm}^{-2}$ at 600 and 700 °C, respectively.

Despite the absence of any references to the infiltration of nanoscale structures based on proton-conducting electrolytes, the development of nanofibrous, freeze-casted electrodes for PCFC creates the base for their future appearance [154–156].

5.3. Triple conducting composite electrodes fabricated using infiltration. Stability issues

Li et al. [114] reported on the influence of GDC loading on the performance of the conventional PBC-BZCY composite cathode. The PBC-BZCY electrode without GDC loading showed R_p of 2.53 $\Omega \cdot \text{cm}^2$ at 600 °C, and then it was decreased on the dependence on the GDC loading as 1.23 $\Omega \cdot \text{cm}^2$ (19.4 wt. %) and 0.48 $\Omega \cdot \text{cm}^2$ (31.2 wt. %). Schematically, double and

triple conducting composites are shown in Figure 8. The TPB-O represents the place where ORR takes place (oxygen molecular, electron, and oxygen ion are available), such as the interface of PBC-GDC. The TPB-H densities denoted the place where water is created.

The elementary reactions for the $\text{H}^+/\text{O}^{2-}/\text{e}^-$ -conducting composite cathode are shown in Table 2. Compared with the double conducting (H^+/e^- or O^{2-}/e^-) cathode materials, intermediate species both H^+ and O^{2-} may transfer to the TPB-H for triple phase conducting cathode, which would accelerate the cathode reaction of H-SOFCs. As a result, Li et al. [114] reported for the anode-supported cell with the BZCY electrolyte (12 μm) and the 29.6 wt. % GDC@PBC-BZCY cathode the excellent power density of 1.02 $\text{W} \cdot \text{cm}^{-2}$ at 700 °C and extremely low polarization resistance of 0.051 $\Omega \cdot \text{cm}^2$ at 700 °C as well as good stability over 100 h at 600 °C.

Table 2 – Elementary reaction steps for $\text{H}^+/\text{O}^{2-}/\text{e}^-$ -conducting composite cathode in PCFC.

Step	Elementary reaction
1	$\text{O}_2(g) \rightarrow 2\text{O}_{ad}$
2	$\text{O}_{ad} + e^-_{cathode} \rightarrow \text{O}_{ad}^-$
3	$\text{O}_{ad}^- \rightarrow \text{O}_{TPB-O}^-$
4	$\text{O}_{TPB-O}^- + e^-_{cathode} \rightarrow \text{O}_{TPB-O}^{2-}$
5	$\text{O}_{TPB-O}^{2-} \rightarrow \text{O}_{TPB-H}^{2-}$
6	$\text{H}^+_{electrolyte} \rightarrow \text{H}^+_{TPB-H}$
7	$\text{H}^+_{TPB-H} + \text{O}_{TPB-H}^{2-} \rightarrow \text{OH}^-_{TPB-H}$
8	$\text{H}^+_{TPB-H} + \text{OH}^-_{TPB-H} \rightarrow \text{H}_2\text{O}_{TPB-H}$
9	$\text{H}_2\text{O}_{TPB-H} \rightarrow \text{H}_2\text{O}(g)$

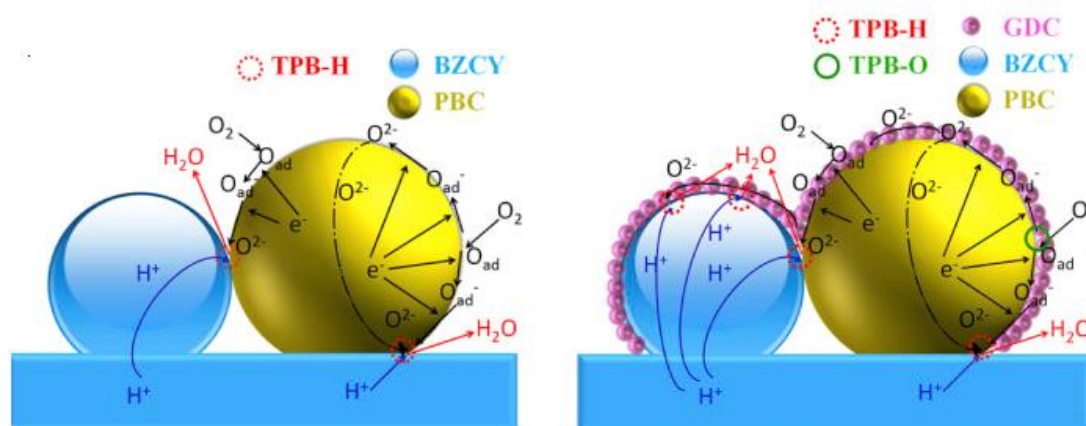


Figure 8 Schematic illustration of the cathode reaction of PCFCs (a) with PBC-BZCY conventional composite cathode and (b) with that modified by infiltration GDC@PBC-BZCY [114].

Saqib et al. [157] proposed a modified triple conducting air electrode for the reversible PCC with $\text{BaCe}_{0.7}\text{Zr}_{0.1}\text{Y}_{0.2-x}\text{Yb}_x\text{O}_{3-\delta}$ (BCZYYb) electrolyte (17 μm) via SDC infiltration to the composite $\text{BaCo}_{0.4}\text{Zr}_{0.1}\text{Fe}_{0.4}\text{Y}_{0.1}\text{O}_{3+\delta}$ (BCZFY)-BCZYYb electrode. After infiltration of 0.198 wt. % SDC, R_p decreased from 1.388 to 1.079 $\Omega \cdot \text{cm}^2$, due to the favorable extension of TPBs, while increasing the SDC loading amount to 0.225 wt. % caused severe agglomeration of SDC particles on the cathode surface, resulting in increasing R_p to 2.94 $\Omega \cdot \text{cm}^2$. The SDC-infiltrated cell reached the current density of 1.76 $\text{A} \cdot \text{cm}^{-2}$ at 700 °C at an applied voltage of 1.5 V compared to 1.17 $\text{A} \cdot \text{cm}^{-2}$ for the non-infiltrated cell indicating that well-distributed SDC nanoparticles, as an oxygen-ionic conductor, significantly improve the OER activity in the PCEC mode.

Solis et al. [158] observed 90 % improvement of the performance of the conventional $\text{La}_{5.5}\text{WO}_{11.25-\delta}$ (LWO)/LSM composite cathode in PCFC based on an LWO protonic conducting electrolyte by infiltration 20 wt. % SDC. Choi et al. [159] used sequential infiltration of an electron-conducting component (Sr-doped LaVO_3 , 35 wt. % loading), and small amounts of CeO_2 and Pd as catalysts to the porous $\text{Ba}(\text{Zr}_{0.75}\text{Y}_{0.15})\text{O}_{3-\delta}$ backbone to produce highly active electrodes for hydrogen pump, which demonstrated R_p of 0.15 $\Omega \cdot \text{cm}^2$ at 1 $\text{A} \cdot \text{cm}^{-2}$ at 700 °C. The overpotential at a large current density of 2 $\text{A} \cdot \text{cm}^{-2}$ was only about 1.1 V at 700 °C.

Triple ion-electron conducting (TIECs) cathode materials are the newest type of cathode materials in the PCFC application developed recently [8, 160]. Theoretically, this type of cathode materials is the best cathode materials to minimize R_p at intermediate-to-low operating temperature, as it provides the largest electrochemical reaction sites (Figure 2). Nevertheless, a few studies were performed to further enhancement of TIEC-based cathodes, particularly, using the infiltration technique.

Hwang et al. [161] reported on nanocomposite electrodes prepared by infiltration of $\text{Ba}(\text{Co}_{0.4}\text{Fe}_{0.4}\text{Zr}_{0.1}\text{Y}_{0.1})\text{O}_{3-\delta}$ (BCFZY) and $(\text{Ba}_{0.95}\text{La}_{0.05})(\text{Fe}_{0.8}\text{Zn}_{0.2})\text{O}_{3-\delta}$ (BLFZ) to a porous $\text{Ba}(\text{Ce}_{0.55}\text{Zr}_{0.3}\text{Y}_{0.15})\text{O}_{3-\delta}$ (BCZY) electrolyte backbone. The electrodes, infiltrated several times to achieve 15 vol. %, with final sintering temperature of 850 °C. Moreover, to construct a triple-component cathode, BCFZY precursor solution was infiltrated in five cycles into the BCZY-BLFZ nanocomposite cathode after the final calcination of BLFZ at 850 °C. It was determined that the BLFZ-based fuel cell had a lower R_{ohmic} compared to that based on BCFZY due

to higher BLFZ conductivity. However, it exhibited poor catalytic activity. The cell with a triple-component composite cathode, combining positive qualities of two electrode materials, demonstrated superior performance both for H_2 (880 $\text{mW} \cdot \text{cm}^{-2}$ compared to 620 $\text{mW} \cdot \text{cm}^{-2}$ at 600 °C) and for CH_4 (610 $\text{mW} \cdot \text{cm}^{-2}$ compared to 420 $\text{mW} \cdot \text{cm}^{-2}$) fuels. Based on these results, the authors suggested possible contributions of the cathode ORR activity to CH_4 reformation at the anode (Figure 9(a)). The oxygen ions generated by the ORR on the BCFZY surface react with the protons to form water. Some of the oxygen ions also move to the anode through the electrolyte, facilitating the reformation of CH_4 to produce hydrogen.

Jing et al. [162] achieved the reduction by approximately 59 % at 600 °C of the BLFZ-BCZYYb composite cathode resistance by introducing a nanostructured BLFZ@BCZYYb active layer (NAL). The single cell with the NAL showed an over 1.3-fold and 1.5-fold increase in PPD, 60I and 486 $\text{mW} \cdot \text{cm}^{-2}$ at 650 °C with H_2 and NH_3 fuel, respectively. In the recent study, the same group proposed additional activation of the developed NAL layer with PrO_x . The synergistic combination of oxygen-vacancy-rich PrO_x to enhance reaction kinetics and triple-conducting BLFZ to facilitate proton conduction and expand the reactive site (Figure 9(b)), which allowed a 72 % reduction in R_p at 600 °C in a symmetrical cell with NAL compared to the conventional BLFZ-BCZYYb. Consequently, hydrogen-electrode-supported full cells with NAL achieved a PPD of 460 $\text{W} \cdot \text{cm}^{-2}$ and a current density of 0.562 $\text{A} \cdot \text{cm}^{-2}$ at 1.3 V and 600 °C, showing 1.608-fold and 2.030-fold improvements compared to the characteristics of the cell without NAL, respectively.

Xia et al. [163] improved performance of the anode supported PCFC with a BZCY electrolyte and a $\text{BaFe}_{0.8}\text{Zn}_{0.1}\text{Bi}_{0.1}\text{O}_{3-\delta}$ (BFZB) cathode from 816 to 1138 $\text{mW} \cdot \text{cm}^{-2}$ at 700 °C using the infiltration technique to prepare BFZB@BZCY nanocomposite. A unique 3D triple-conducting electrode was in situ prepared by infiltration of a porous BZCY backbone with $\text{Co}(\text{NO}_3)_2$ (up to 35 wt. %) and high-temperature sintering.

The authors [163] established that the reaction between Co^{2+} and $\text{BaZr}_{0.4}\text{Ce}_{0.4}\text{Y}_{0.2}\text{O}_{3-\delta}$ (BZCY) after firing at temperatures ≥ 900 °C resulted in beneficial formation of oxide products, including $\text{Ba}(\text{Zr}_{0.4}\text{Ce}_{0.4}\text{Y}_{0.2})_{1-x}\text{Co}_x\text{O}_{3-\delta}$, $(\text{Ce,Zr,Y})\text{O}_2$, and Co_3O_4 . $\text{Ba}(\text{Zr}_{0.4}\text{Ce}_{0.4}\text{Y}_{0.2})_{1-x}\text{Co}_x\text{O}_{3-\delta}$ offers conducting pathways for proton, electron, and oxygen ion, $(\text{Ce,Zr,Y})\text{O}_2$ and Co_3O_4 additionally help conducting oxygen ion and electron, respectively. Due to an increased number of active sites, a typical symmetrical

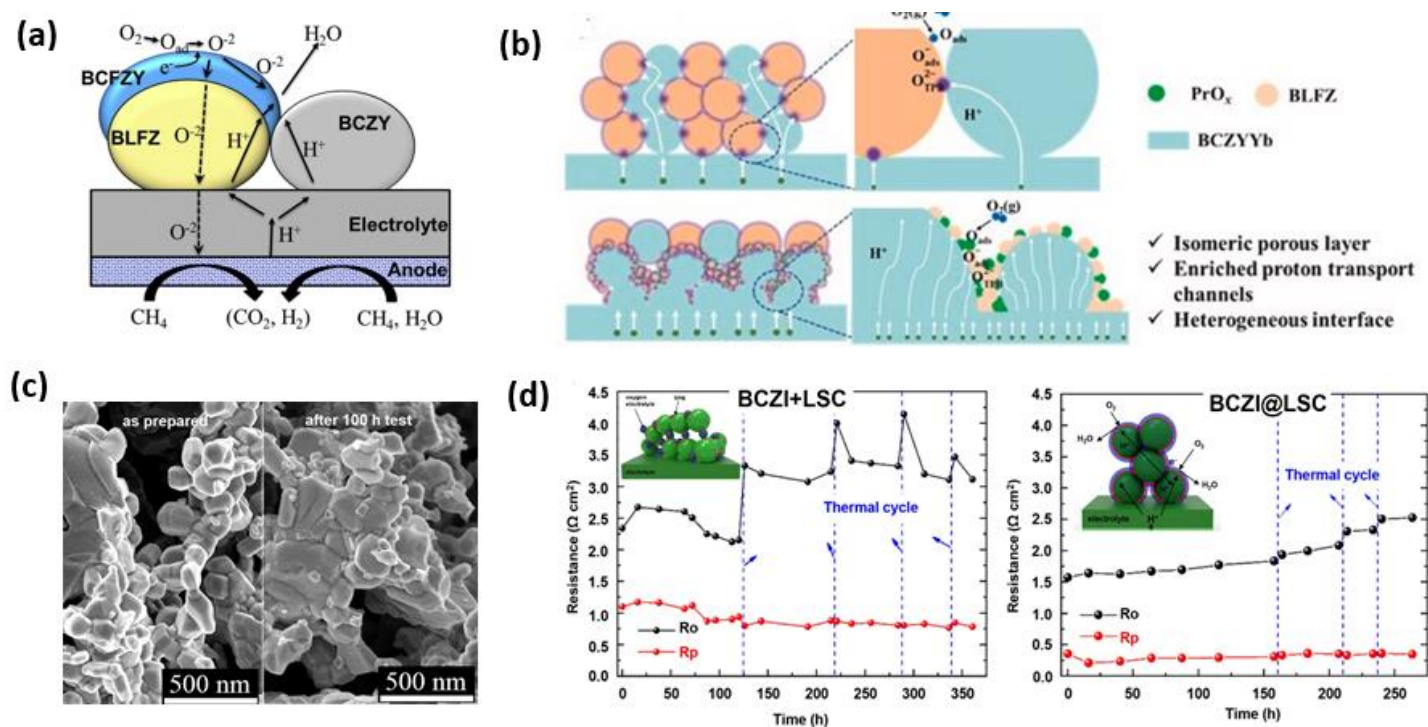


Figure 9 (a) Schematic presentation of the electrochemical reaction at the triple-component cathode in the CH_4 fuel [161]; (b) The mechanism of PrO_x/BLFZ nanoparticles synergy for concerted promotion of electrochemical reaction in the bilayer cathode comprising conventional BLFZ-BCZYYb porous layer and BCZYYb@ PrO_x/BLFZ nanocomposite active layer [19]; (c) SEM images the 42.2 wt. % LSN-infiltrated BCZYYbCu electrode (a) before and (b) after 100 h test at 700°C (Reconstructed using the data [141]); (d) Curves of ASR values as a function of time during cycling testing of BCZI + LSC (left) and BCZI@LSC (right) single cells (Reconstructed using the data [164]).

cell with the 3D cathode has demonstrated low polarization resistances of 0.058 and $0.198 \Omega \cdot \text{cm}^2$ at 700 and 600°C , respectively.

5.4. Stability issues

The long-term stability of infiltrated electrodes is a critical issue before the successful commercialization of the infiltration technology, even though significant progress has been made in the performance enhancement of cell electrodes.

Sun et al. observed no degradation of the current density of the reversible cell with Co-free LSN@BCZYYbCu electrode during the thermal cycles from 400 to 700°C (7 cycles for 14 hours). However, after a long-term test for 100 h at 700°C , current density declined by 19.4 %, the ohmic cell resistance, R_o , increased by 3.8 %, and R_p increased by 73.5 %, mainly due to the growth, agglomeration, and sintering of the LSN nano-particles (Figure 9(c)).

Chen et al. [164] conducted a cycling performance and interface stability tests of tubular protonic reversible solid oxide cells with the $\text{BaCe}_{0.5}\text{Zr}_{0.4}\text{In}_{0.1}\text{O}_3\text{-La}_{0.6}\text{Sr}_{0.4}\text{CoO}_3$ air electrodes formed by conventional mechanical mixing (BCZI + LSC) and by infiltration (BCZI@LSC). LSC solution was then impregnated into the porous BCZI

backbone, pre-sintered at 1300°C and calcined at 500°C to form the electrode with 40 wt. % loading, while BCZI + LSC was sintered at 1100°C . In the air electrode obtained by conventional mechanical mixing, BCZI proton conductor material and LSC oxygen electrode material are randomly stacked together, with the three-phase reaction interface at their junction (Figure 9(d), left). Conversely, in the impregnated electrode, LSC oxygen electrode material uniformly covered the surface of the BCZI proton conductor backbone, as confirmed by the SEM image (Figure 9(d), right). As a result, the cell with the BCZI@LSC electrode, representing a continuous catalytic thin film, exhibited electrochemical performance enhanced by 51 %. The cells endured 11–14 reversible cycles for 300–360 h, showing slight decreasing in R_p . The ohmic resistance degraded significantly for both cells. It was revealed that after long-term high-temperature operation and thermal cycling, the LSC film in the infiltrated electrode became discontinuous, leading to a reduced continuous area of the electron-conducting phase in BCZI@LSC and a time-dependent increase in the R_o value.

According to Wang et al. [165], the microstructural degradation of the infiltrated nanoparticles can be restrained by lowering the operation temperature. As for

example, BCY@LSC electrodes demonstrated good stability without significant performance degradation when tested at 600 °C in 10 vol. % humidified air for 900 h. The growth of cathode nanoparticles can be hindered with the co-impregnation of both catalyst and electrolyte nanoparticles [166].

The main principles formulated by Kiebach [167] on the basis of 5000 hours degradation study should be taken into account when constructing the cells with impregnated electrodes:

1) The introduction of a sufficient amount of electrocatalyst into the backbone is imperative to ensure percolation, even in the presence of particle coarsening or growth;

2) It is crucial to operate the SOFC at maximum exposure and operation temperatures as low as possible to avoid surface area loss due to surface wetting to ensure longer lifetime of infiltrated cells;

3) To optimize the performance in stacks, infiltrated electrodes should be utilized preferably with highly-conducting contact (collecting) layers to ensure the uniform distribution of current across the entire electrode surface area.

In summary, it is important to acknowledge that the infiltration technique may also be successfully applied to enhance the densification of proton-conducting electrolyte membranes [168] and to fabricate composite electrolytes [169–171].

6. Conclusions

In this review, the advances in utilization of infiltration technique to enhance the air electrode performance of ceramic fuel and electrolysis cells with proton-conducting electrolytes were considered. The controllable parameters of infiltration were shown to be of great importance for the sustainable implementation of this technique on both the laboratory and industrial scale. The use of electrolyte backbones was in the focus of this review as it eliminates issues related to the electrode/electrolyte mismatching, ensures excellent electrode adhesion to the electrolyte, allows controlling the size of infiltrated catalyst particles at a nanometer level and, consequently, the generation of numerous reactive zones due to low calcination temperatures. Moreover, specifically for the proton-conducting backbone, it allows the TPB to be extended to the electrode volume, which allows not only triple conducting materials, but various electron conductors and MIECs to be successfully used to obtain highly performed air electrodes for PCCs.

Typically, a catalyst loading of 35 to 55 wt. % is required to achieve minimal R_p and maximal PPD. For the

electrodes with the electrolyte backbone, the results obtained by different research groups can be compared using a polarization resistance enhancement factor, f_p , and a cell performance enhancement factor, f_{PPD} , which are defined as follows:

$$f_p = R_p(Cat - El)/R_p(Cat@El), \quad (1)$$

$$f_{PPD} = PPD(Cat@El)/PPD(Cat - El), \quad (2)$$

where R_p , $PPD(Cat@El)$ are characteristics of an infiltrated nanocomposite electrode, while R_p , $PPD(Cat - El)$ correspond to a conventional composite electrode of the same composition. Examples of the enhancement factors are shown in Figure 10. It is seen that typically $f_p > f_{PPD}$. Decreasing ohmic losses related to the electrolyte thickness and enhancing the anode performance will consequently further increase f_{PPD} .

The main limitation of using the electrolyte backbone is the need to load a significant amount of catalyst to achieve maximum enhancement. This process may require numerous infiltration cycles (4–8). However, using electrolyte backbones with optimized porosity, as well as introducing surfactants (Pluronic 123 and Triton X-100) and chelating agents, may decrease the number of cycles to one to three and ensure the uniform distribution of infiltrated particles sized in the low nanometer range (10–20 nm and below). This enhances both the catalytic activity and durability of the infiltrated electrodes.

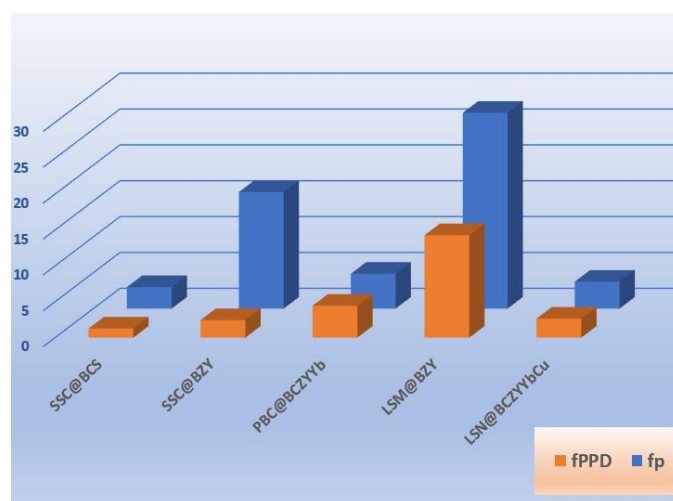


Figure 10 Enhancement factors for the polarization resistance, f_p , and for the cell performance, f_{PPD} , obtained for various nanocomposite air electrodes: SSC@BCS [125], SSC@BZY [64], PBC@BCZYYb [131], LSM@BZY [128], LSN@BCZYYbCu [141].

Supplementary materials

No supplementary materials are available.

Funding

This research had no external funding.

Acknowledgments

The authors are grateful to Dr. Elena Filonova (UrFU) and PhD student N. Pikalova (IMET UB RUS) for the valuable support in the literature search and the preparation of the illustrative materials for this review.

Author contributions

Elena Pikalova: Conceptualization; Writing – Original draft; Visualization; Writing – Review & Editing.

Conflict of interest

The authors declare no conflict of interest.

Additional information



Elena Yu. Pikalova received Ph. D degree in 2011 at the Institute of High Temperature Electrochemistry (IHTE UB RAS, Yekaterinburg, Russia) under the supervision of Corresponding Member of the Russian Academy of Sciences, Prof. Vitaliy G. Bamburov. Currently, she is the senior researcher of the

Laboratory of Kinetics the of IHTE UB RAS and the leader of the research group on the development of air electrodes for SOFCs and PCFCs, the author of 121 research papers (h-index 29), 12 patents and 5 book chapters and one monograph. Area of scientific interests and research includes but is not limited: alternative energy sources, SOFCs/PCFCs, solid state electrolytes, thin-film technologies, air electrode materials, MIEC membranes, electrode activation methods, impedance spectroscopy, DRT analysis.

References

- Kim D, Lee TK, Han S, Jung Y, et al., Advances and challenges in developing protonic ceramic cells, *Mater. Today Energy*, **36** (2023) 101365. <https://doi.org/10.1016/j.mtener.2023.101365>
- Wang Y, Ling Y, Wang B, Zhai G, et al., A review of progress in proton ceramic electrochemical cells: material and structural design, coupled with value-added chemical production, *Energy Environ. Sci.*, **16** (2023) 5721–5770. <https://doi.org/10.1039/D3EE03121G>
- Zvonareva I, Fu X-Z, Medvedev D, Shao Z, Electrochemistry and energy conversion features of protonic ceramic cells with mixed ionic-electronic electrolytes, *Energy*

- Environ. Sci.*, **15** (2022) 439–465. <https://doi.org/10.1039/D1EE03109K>
- Wang Q, Ricote S, Chen M, Oxygen electrodes for protonic ceramic cells, *Electrochimica Acta*, **446** (2023) 142101. <https://doi.org/10.1016/j.electacta.2023.142101>
- Zhang W, Zhang X, Song Y, Wang G, Recent progress on cathode materials for protonic ceramic fuel cells, *Sustain*, **3** (2024) 100028. <https://doi.org/10.1016/j.nxsust.2024.100028>
- Oh S, Kim H, Jeong I, Kim D, et al., Recent progress in oxygen electrodes for protonic ceramic electrochemical cells, *J. Korean Ceram. Soc.*, **61** (2024) 224–249. <https://doi.org/10.1007/s43207-023-00360-y>
- Kang H, Park YJ, Baek SY, Kim J, et al., Recent breakthroughs in cathode of protonic ceramic fuel cells: Materials, functionalization, and future perspectives, *InfoMat*, (2025) e70025. <https://doi.org/10.1002/inf2.70025>
- Kasyanova AV, Tarutina LR, Rudenko AO, Lyagaeva JG, Medvedev DA, Ba(Ce,Zr)O₃-based electrodes for protonic ceramic electrochemical cells: towards highly compatible functionality and triple-conducting behaviour, *Russ. Chem. Rev.*, **89** (2020) 667–692. <https://doi.org/10.1070/RCR4928>
- Medvedev D, Trends in research and development of protonic ceramic electrolysis cells, *Int. J. Hydrog. Energy*, **44** (2019) 26711–26740. <https://doi.org/10.1016/j.ijhydene.2019.08.130>
- Medvedev DA, Ricote S, Electrochemistry of proton-conducting ceramic materials and cells, *J. Solid State Electrochem.*, **24** (2020) 1445–1446. <https://doi.org/10.1007/s10008-020-04655-6>
- Inocencio CVM, Holade Y, Morais C, Kokoh KB, Napporn TW, Electrochemical hydrogen generation technology: Challenges in electrodes materials for a sustainable energy, *Electrochem. Sci. Adv.*, **3** (2023) e2100206. <https://doi.org/10.1002/elsa.202100206>
- Tarutin AP, Filonova EA, Ricote S, Medvedev DA, Shao Z, Chemical design of oxygen electrodes for solid oxide electrochemical cells: A guide, *Sustain. Energy Technol. Assess.*, **57** (2023) 103185. <https://doi.org/10.1016/j.seta.2023.103185>
- Pei K, Zhou Y, Xu K, Zhang H, et al., Surface restructuring of a perovskite-type air electrode for reversible protonic ceramic electrochemical cells, *Nat. Commun.*, **13** (2022) 2207. <https://doi.org/10.1038/s41467-022-29866-5>
- Liu Z, Bai Y, Sun H, Guan D, et al., Synergistic dual-phase air electrode enables high and durable performance of reversible proton ceramic electrochemical cells, *Nat. Commun.*, **15** (2024) 472. <https://doi.org/10.1038/s41467-024-44767-5>
- Wang Z, Jiang G, Zhang Y, Wang Y, et al., An active and durable perovskite electrode with reversibly phase transition-induced exsolution for protonic ceramic cells, *C Chem. Eng. J.*, **500** (2024) 157268. <https://doi.org/10.1016/j.cej.2024.157268>
- Tarutina LR, Kasyanova AV, Starostin GN, Vdovin GK, Medvedev DA, Electrochemical activity of original and infiltrated Fe-doped Ba(Ce,Zr,Y)O₃-based electrodes to be used for protonic ceramic fuel cells, *Catalysts*, **12** (2022) 1421. <https://doi.org/10.3390/catal1211421>
- Yao P, Zhang J, Qiu Q, Zhao Y, et al., Enhancing oxygen reduction kinetics and proton transfer of La_{0.6}Sr_{0.4}Co_{0.2}Fe_{0.8}O_{3-δ} cathode through Pr₂Ni_{0.5}Co_{0.5}O_{4-δ} impregnation for protonic ceramic fuel cells, *Adv. Energy*

- Mater., **15** (2025) 2403335.
<https://doi.org/10.1002/aenm.202403335>
18. Lu X, Yang Z, Zhang J, Zhao X, et al., A cobalt-free Pr_6O_{11} - $\text{BaCe}_{0.2}\text{Fe}_{0.8}\text{O}_{3-\delta}$ composite cathode for protonic ceramic fuel cells with promising oxygen reduction activity and hydration ability, *J. Power Sources*, **599** (2024) 234233.
<https://doi.org/10.1016/j.jpowsour.2024.234233>
19. Jing J, Lei Z, Zheng Z, Wang H, et al., Multifunctional nanocomposite active layers synergistically enhance the performance of reversible proton ceramic cell, *Renew. Energy*, **243** (2025) 122551.
<https://doi.org/10.1016/j.renene.2025.122551>
20. Li G, He B, Ling Y, Xu J, Zhao L, Highly active YSB infiltrated LSCF cathode for proton conducting solid oxide fuel cells, *Int. J. Hydrog. Energy*, **40** (2015) 13576–13582.
<https://doi.org/10.1016/j.ijhydene.2015.07.164>
21. Zhang Z, Wang J, Chen Y, Tan S, et al., In situ formation of a 3D core-shell and triple-conducting oxygen reduction reaction electrode for proton-conducting SOFCs, *J. Power Sources*, **385** (2018) 76–83.
<https://doi.org/10.1016/j.jpowsour.2018.03.029>
22. Tarutina LR, Kuznetsova PS, Skutina LS, Murashkina AA, Medvedev DA, Phase relationships and thermal behavior of one-pot synthesized dual-phase $\text{BaCe}_{0.5}\text{Fe}_{0.5}\text{O}_{3-\delta}$ composites, *Ceram. Int.*, **51** (2025) 3471–3481.
<https://doi.org/10.1016/j.ceramint.2024.11.324>
23. Skutina LS, Yang G, Medvedev DA, Engineering the one-pot synthesized $\text{Ba}(\text{Ce},\text{Fe})\text{O}_3$ -based composites as triple-conducting electrodes for solid oxide electrochemical cell applications, *Chem. Eng. J.*, **512** (2025) 162320.
<https://doi.org/10.1016/j.cej.2025.162320>
24. Liu Z, Chen Y, Yang G, Yang M, et al., One-pot derived thermodynamically quasi-stable triple conducting nanocomposite as robust bifunctional air electrode for reversible protonic ceramic cells, *Appl. Catal. B Environ.*, **319** (2022) 121929. <https://doi.org/10.1016/j.apcatb.2022.121929>
25. Kang EH, Choi HR, Park JS, Kim KH, et al., Protonic ceramic fuel cells with slurry-spin coated $\text{BaZr}_{0.2}\text{Ce}_{0.6}\text{Y}_{0.1}\text{Yb}_{0.1}\text{O}_{3-\delta}$ thin-film electrolytes, *J. Power Sources*, **465** (2020) 228254.
<https://doi.org/10.1016/j.jpowsour.2020.228254>
26. Lee S, Park S, Wee S, Baek HW, Shin D, One-dimensional structured $\text{La}_{0.6}\text{Sr}_{0.4}\text{Co}_{0.2}\text{Fe}_{0.8}\text{O}_{3-\delta}$ - $\text{BaCe}_{0.5}\text{Zr}_{0.35}\text{Y}_{0.15}\text{O}_{3-\delta}$ composite cathode for protonic ceramic fuel cells, *Solid State Ion.*, **320** (2018) 347–352.
<https://doi.org/10.1016/j.ssi.2018.03.010>
27. Park HS, Jeong HJ, Kim K, Chang W, et al., High-performance proton ceramic fuel cells using a perovskite oxide cathode surface decorated with CoO_x nanoparticles, *Appl. Surf. Sci.*, **612** (2023) 155812.
<https://doi.org/10.1016/j.apsusc.2022.155812>
28. Papac MC, Huang J, Zakutayev A, O'Hayre R, Combinatorial impedance spectroscopy with Bayesian analysis for triple ionic-electronic conducting perovskites, *J. Mater. Chem. A*, **11** (2023) 5267–5278.
<https://doi.org/10.1039/D2TA01736A>
29. Watanabe M, Uchida H, Shibata M, Mochizuki N, Amikura K, High performance catalyzed-reaction layer for medium temperature operating solid oxide fuel cells, *J. Electrochem. Soc.*, **141** (1994) 342–346.
<https://doi.org/10.1149/1.2054728>
30. Desta HG, Gebresslassie G, Zhang J, Lin B, Zheng Y, et al., Enhancing performance of lower-temperature solid oxide fuel cell cathodes through surface engineering, *Prog. Mater. Sci.*, **147** (2025) 101353.
<https://doi.org/10.1016/j.pmatsci.2024.101353>
31. Dai M, Li F, Fang S, He D, et al., Advances in nanostructured electrodes for solid oxide cells by infiltration or exsolution, *Materials*, **18** (2025) 1802.
<https://doi.org/10.3390/ma18081802>
32. Beresnev SM, Bobrenok OF, Kuzin BL, Bogdanovich NM, et al., Single fuel cell with supported LSM cathode, *Russ. J. Electrochem.*, **48** (2012) 969–975.
<https://doi.org/10.1134/S1023193512100035>
33. Pikalova EYu, Osinkin DA, Structural stability and features of electrical and electrochemical behavior under reducing conditions of $\text{Pr}_{0.4}\text{Sr}_{0.6}\text{Co}_{0.2}\text{Fe}_{0.7}\text{Nb}_{0.1}\text{O}_{3-\delta}$ material for the symmetrical SOFCs, *Electrochem. Mater. Technol.*, **3** (2024) 20243039. <https://doi.org/10.15826/elmattech.2024.3.039>
34. Osinkin DA, Beresnev SM, Bogdanovich NM, Influence of Pr_6O_{11} on oxygen electroreduction kinetics and electrochemical performance of $\text{Sr}_2\text{Fe}_{1.5}\text{Mo}_{0.5}\text{O}_{6-\delta}$ based cathode, *J. Power Sources*, **392** (2018) 41–47.
<https://doi.org/10.1016/j.jpowsour.2018.04.076>
35. Osinkin DA, An approach to the analysis of the impedance spectra of solid oxide fuel cell using the DRT technique, *Electrochimica Acta*, **372** (2021) 137858.
<https://doi.org/10.1016/j.electacta.2021.137858>
36. Osinkin DA, Precursor of $\text{Pr}_2\text{NiO}_{4+\delta}$ as a highly effective catalyst for the simultaneous promotion of oxygen reduction and hydrogen oxidation reactions in solid oxide electrochemical devices, *Int. J. Hydrog. Energy*, **46** (2021) 24546–24554. <https://doi.org/10.1016/j.ijhydene.2021.05.022>
37. Antonova EP, Khodimchuk AV, Tropin ES, Porotnikova NM, et al., Influence of modifying additives on electrochemical performance of $\text{La}_2\text{NiO}_{4+\delta}$ -based oxygen electrodes, *Solid State Ion.*, **346** (2020) 115215.
<https://doi.org/10.1016/j.ssi.2019.115215>
38. Yaroslavtsev IYu, Bronin DI, Vdovin GK, Isupova LA, Oxide cathodes for electrochemical devices made with the use of a nanostructured composition material, *Russ. J. Electrochem.*, **48** (2012) 981–985.
<https://doi.org/10.1134/S1023193512100138>
39. Meshcherskikh AN, Khaliullina ASH, Pikalova EYu, Dunyushkina LA, $\text{La}_2\text{NiO}_{4+\delta}$ -based oxygen electrodes for proton-conducting $\text{Sr}_{0.98}\text{Zr}_{0.95}\text{Yb}_{0.05}\text{O}_{3-\delta}$ electrolyte for application in IT-SOFCs, *Electrochem. Mater. Technol.*, **4** (2025) 20254047.
<https://doi.org/10.15826/elmattech.2025.4.047>
40. Antonova E, Tropin E, Composite $\text{LaNi}_{0.6}\text{Fe}_{0.4}\text{O}_{3-\delta}$ - $\text{La}_{0.9}\text{Sr}_{0.1}\text{Sc}_{0.9}\text{Co}_{0.1}\text{O}_{3-\delta}$ cathodes for proton conducting solid oxide fuel cells: Electrode kinetics study, *Ceram. Int.*, **50** (2024) 40492–40499.
<https://doi.org/10.1016/j.ceramint.2024.04.025>
41. Li X, Zhou L, Li Q, Kalu A, et al., Nanocomposite electrodes as a new opportunity to transform the performance of solid oxide cells, *J. Mater. Chem. A*, **11** (2023) 25803–25824.
<https://doi.org/10.1039/D3TA05430F>
42. Jiang Z, Xia C, Chen F, Nano-structured composite cathodes for intermediate-temperature solid oxide fuel cells via an infiltration/impregnation technique, *Electrochimica Acta*,

- 55 (2010) 3595–3605. <https://doi.org/10.1016/j.electacta.2010.02.019>
43. Vohs JM, Gorte RJ, High-performance SOFC cathodes prepared by infiltration, *Adv. Mater.*, **21** (2009) 943–956. <https://doi.org/10.1002/adma.200802428>
44. Shoklapper TZ, Jacobson CP, Visco SJ, De Jonghe LC, Synthesis of dispersed and contiguous nanoparticles in solid oxide fuel cell electrodes, *Fuel Cells*, **8** (2008) 303–312. <https://doi.org/10.1002/fuce.200800030>
45. Connor PA, Yue X, Savaniu CD, Price R, et al., Tailoring SOFC electrode microstructures for improved performance, *Adv. Energy Mater.*, **8** (2018) 1800120. <https://doi.org/10.1002/aenm.201800120>
46. Ding D, Li X, Lai SY, Gerdes K, Liu M, Enhancing SOFC cathode performance by surface modification through infiltration, *Energy Environ. Sci.*, **7** (2014) 552. <https://doi.org/10.1039/c3ee42926a>
47. Chen S, Zhang H, Yao C, Lou H, et al., Review of SOFC cathode performance enhancement by surface modifications: recent advances and future directions, *Energy Fuels*, **37** (2023) 3470–3487. <https://doi.org/10.1021/acs.energyfuels.2c03934>
48. Kim S, Kim G, Manthiram A, A review on infiltration techniques for energy conversion and storage devices: from fundamentals to applications, *Energy Fuels*, **5** (2021) 5024–5037. <https://doi.org/10.1039/D1SE00878A>
49. Niu Y, Huo W, Yu Y, Li W, et al., Cathode infiltration with enhanced catalytic activity and durability for intermediate-temperature solid oxide fuel cells, *Chin. Chem. Lett.*, **33** (2022) 674–682. <https://doi.org/10.1016/j.ccl.2021.07.037>
50. Tahir NNM, Baharuddin NA, Samat AA, Osman N, Somalu MR, A review on cathode materials for conventional and proton-conducting solid oxide fuel cells, *J. Alloys Compd.*, **894** (2022) 162458. <https://doi.org/10.1016/j.jallcom.2021.162458>
51. Tarutin AP, Lyagaeva JG, Medvedev DA, Bi L, Yaremchenko AA, Recent advances in layered $LmNiO_{4+\delta}$ nickelates: fundamentals and prospects of their applications in protonic ceramic fuel and electrolysis cells, *J. Mater. Chem. A*, **9** (2021) 154–195. <https://doi.org/10.1039/D1TA08132A>
52. Wang M, Su C, Zhu Z, Wang H, Ge L, Composite cathodes for protonic ceramic fuel cells: Rationales and materials, *Composites Part B: Engineering*, **238** (2022) 109881. <https://doi.org/10.1016/j.compositesb.2022.109881>
53. Mather GC, Muñoz-Gil D, Zamudio-García J, Porrás-Vázquez JM, et al., Perspectives on cathodes for protonic ceramic fuel cells, *Appl. Sci.*, **11** (2021) 5363. <https://doi.org/10.3390/app1125363>
54. Zhang W, Hu YH, Progress in proton-conducting oxides as electrolytes for low-temperature solid oxide fuel cells: From materials to devices, *Energy Sci. Eng.*, **9** (2021) 984–1011. <https://doi.org/10.1002/ese3.886>
55. Rehman J, Hanif MB, Khan MZ, Ullah M, et al., A review of proton-conducting electrolytes for efficient low-temperature solid oxide fuel cells: Progress, challenges, and perspectives, *Energy Fuels*, **38** (2024) 22637–22665. <https://doi.org/10.1021/acs.energyfuels.4c03683>
56. Chen X, Tan Y, Li Z, Liu T, et al., Advanced air electrodes for reversible protonic ceramic electrochemical cells: A comprehensive review, *Adv. Mater.*, (2025) 2418620. <https://doi.org/10.1002/adma.202418620>
57. Guo Z, Xu L, Ling Y, Wang P, et al., A perspective on cathode materials for proton-conducting solid oxide fuel cells, *Int. J. Hydrog. Energy*, **106** (2025) 52–64. <https://doi.org/10.1016/j.ijhydene.2025.01.461>
58. Iwahara H, Uchida H, Morimoto K, High temperature solid electrolyte fuel cells using perovskite-type oxide based on $BaCeO_3$, *J. Electrochem. Soc.*, **137** (1990) 462–465. <https://doi.org/10.1149/1.2086463>
59. Taniguchi N, Hatoh K, Niikura J, Gamo T, Iwahara H, Proton conductive properties of gadolinium-doped barium cerates at high temperatures, *Solid State Ion.*, **53–56** (1992) 998–1003. [https://doi.org/10.1016/0167-2738\(92\)90283-U](https://doi.org/10.1016/0167-2738(92)90283-U)
60. Maffei N, Pelletier L, Charland JP, McFarlan A, A direct ammonia fuel cell using barium cerate proton conducting electrolyte doped with gadolinium and praseodymium, *Fuel Cells*, **7** (2007) 323–328. <https://doi.org/10.1002/fuce.200600038>
61. Taherparvar H, Effect of humidification at anode and cathode in proton-conducting SOFCs, *Solid State Ion.*, **162–163** (2003) 297–303. [https://doi.org/10.1016/S0167-2738\(03\)00222-4](https://doi.org/10.1016/S0167-2738(03)00222-4)
62. Pikalova E, Medvedev D, Effect of anode gas mixture humidification on the electrochemical performance of the $BaCeO_3$ -based protonic ceramic fuel cell, *Int. J. Hydrog. Energy*, **41** (2016) 4016–4025. <https://doi.org/10.1016/j.ijhydene.2015.11.092>
63. Antonova EP, Bronin DI, Stroeve AYU, Polarization resistance of platinum electrodes in contact with proton-conducting $La_{0.9}Sr_{0.1}ScO_{3-\delta}$, *Russ. J. Electrochem.*, **50** (2014) 613–616. <https://doi.org/10.1134/S1023193514070027>
64. Bi L, Traversa E, Tailoring electrode materials for proton-conducting solid oxide fuel/electrolysis cells with chemically stable $BaZrO_3$ electrolyte, *ECS Meet. Abstr.*, **MA2016-01** (2016) 1360–1360. <https://doi.org/10.1149/MA2016-01/28/1360>
65. Lim D-K, Im H-N, Singh B, Song S-J, Investigations on electrochemical performance of a proton-conducting ceramic-electrolyte fuel cell with $La_{0.8}Sr_{0.2}MnO_3$ cathode, *J. Electrochem. Soc.*, **162** (2015) F547–F554. <https://doi.org/10.1149/2.0551506jes>
66. Hu H, Liu M, Interfacial polarization characteristics of $Pt|BaCe_{0.8}Gd_{0.2}O_3|Pt$ cells at intermediate temperatures, *J. Electrochem. Soc.*, **144** (1997) 3561–3567. <https://doi.org/10.1149/1.1838048>
67. Antonova EP, Bronin DI, Electrical transport and kinetics of electrode processes in the system of $(H_2 + H_2O + Ar)$, $Pt|La_{0.9}Sr_{0.1}ScO_{3-\delta}$, *Russ. J. Electrochem.*, **52** (2016) 595–599. <https://doi.org/10.1134/S102319351607003X>
68. Wu S, Xu X, Li X, Bi L, High-performance proton-conducting solid oxide fuel cells using the first-generation Sr-doped $LaMnO_3$ cathode tailored with Zn ions, *Sci. China Mater.*, **65** (2022) 675–682. <https://doi.org/10.1007/s40843-021-1821-4>
69. Dai H, Xu X, Liu C, Ma C, et al., Tailoring a $LaMnO_3$ cathode for proton-conducting solid oxide fuel cells: integration of high performance and excellent stability, *J. Mater. Chem. A*, **9** (2021) 12553–12559. <https://doi.org/10.1039/D1TA01221E>
70. Sun K, Yu Z, Ni Q, Li Y, et al., Highly durable Sr-doped $LaMnO_3$ -based cathode modified with Pr_6O_{11} nano-catalyst for protonic ceramic fuel cells based on Y-doped $BaZrO_3$

electrolyte, *J. Eur. Ceram. Soc.*, **42** (2022) 4266–4274. <https://doi.org/10.1016/j.jeurceramsoc.2022.04.008>

71. Ahmad MZ, Ahmad SH, Chen RS, Ismail AF, et al., Review on recent advancement in cathode material for lower and intermediate temperature solid oxide fuel cells application, *Int. J. Hydrog. Energy*, **47** (2022) 1103–1120. <https://doi.org/10.1016/j.ijhydene.2021.10.094>

72. Filonova E, Gilev A, Maksimchuk T, Pikalova N, et al., Development of $\text{La}_{1.7}\text{Ca}_{0.3}\text{Ni}_{1-y}\text{Cu}_y\text{O}_{4+\delta}$ materials for oxygen permeation membranes and cathodes for intermediate-temperature solid oxide fuel cells, *Membranes*, **12** (2022) 1222. <https://doi.org/10.3390/membranes12121222>

73. He T, Zhou Q, Jin F. *Cathodes for Solid Oxide Fuel Cell*. 1st ed. John Wiley & Sons: New York, USA; 2020. p. 79–112. <https://doi.org/10.1002/9783527812790.ch3>

74. Lai Y-W, Lee K-R, Yang S-Y, Tseng C-J, et al., Production of $\text{La}_{0.6}\text{Sr}_{0.4}\text{Co}_{0.2}\text{Fe}_{0.8}\text{O}_{3-\delta}$ cathode with graded porosity for improving proton-conducting solid oxide fuel cells, *Ceram. Int.*, **45** (2019) 22479–22485. <https://doi.org/10.1016/j.ceramint.2019.07.270>

75. Ma J, Pan Y, Wang Y, Chen Y, A Sr and Ni doped Ruddlesden–Popper perovskite oxide $\text{La}_{1.6}\text{Sr}_{0.4}\text{Cu}_{0.6}\text{Ni}_{0.4}\text{O}_{4+\delta}$ as a promising cathode for protonic ceramic fuel cells, *J. Power Sources*, **509** (2021) 230369. <https://doi.org/10.1016/j.jpowsour.2021.230369>

76. Medvedev DA, Pikalova EYu. Development of the cathode materials for intermediate-temperature SOFCs based on proton-conducting electrolytes. Springer International Publishing: Cham, Switzerland; 2018. p. 173–80. https://doi.org/10.1007/978-3-319-75702-5_20

77. Antonova EP, Stroeve AYU, Tropin ES, Electrode performance of $\text{La}_2\text{NiO}_{4+\delta}$ cathodes in contact with $\text{La}_{0.9}\text{Sr}_{0.1}\text{ScO}_{3-\delta}$ proton-conducting oxide, *J. Solid State Electrochem.*, **24** (2020) 1447–1451. <https://doi.org/10.1007/s10008-020-04535-z>

78. Pikalova E, Zhulanova T, Ivanova A, Tarutin A, et al., Optimized $\text{Pr}_{1.6}\text{Ca}_{0.4}\text{Ni}_{1-y}\text{Cu}_y\text{O}_{4+\delta}$ phases as promising electrode materials for CeO_2 - and $\text{BaCe}(\text{Zr})\text{O}_3$ -based electrochemical cells, *Ceram. Int.*, **50** (2024) 40476–40491. <https://doi.org/10.1016/j.ceramint.2024.06.048>

79. Fabbri E, Markus I, Bi L, Pergolesi D, Traversa E, Tailoring mixed proton-electronic conductivity of BaZrO_3 by Y and Pr co-doping for cathode application in protonic SOFCs, *Solid State Ion.*, **202** (2011) 30–35. <https://doi.org/10.1016/j.ssi.2011.08.019>

80. Chen Y, Liu H, Zhuang L, Wei Y, Wang H, Hydrogen permeability through $\text{Nd}_{5.5}\text{W}_{0.35}\text{Mo}_{0.5}\text{Nb}_{0.15}\text{O}_{11.25-\delta}$ mixed protonic-electronic conducting membrane, *J. Membr. Sci.*, **579** (2019) 33–39. <https://doi.org/10.1016/j.memsci.2019.02.057>

81. Vøllestad E, Strandbakke R, Tarach M, Catalán-Martínez D, et al., Mixed proton and electron conducting double perovskite anodes for stable and efficient tubular proton ceramic electrolyzers, *Nat. Mater.*, **18** (2019) 752–759. <https://doi.org/10.1038/s41563-019-0388-2>

82. Plekhanov MS, Kuzmin AV, Tropin ES, Korolev DA, Ananyev MV, New mixed ionic and electronic conductors based on LaScO_3 : Protonic ceramic fuel cells electrodes, *J. Power Sources*, **449** (2020) 227476. <https://doi.org/10.1016/j.jpowsour.2019.227476>

83. Stroeve AYU, Gorelov VP, Kuz'min AV, Conductivity of perovskites $\text{La}_{0.9}\text{Sr}_{0.1}\text{Sc}_{1-x}\text{Fe}_x\text{O}_{3-\alpha}$ ($x = 0.003\text{--}0.47$) in

oxidizing and reducing atmospheres, *Phys. Solid State*, **58** (2016) 1521–1527. <https://doi.org/10.1134/S1063783416080278>

84. Kim J, Sengodan S, Kwon G, Ding D, et al., Triple-conducting layered perovskites as cathode materials for proton-conducting solid oxide fuel cells, *ChemSusChem*, **7** (2014) 2811–2815. <https://doi.org/10.1002/cssc.201402351>

85. Strandbakke R, Cherepanov VA, Zuev AYU, Tsvetkov DS, et al., Gd- and Pr-based double perovskite cobaltites as oxygen electrodes for proton ceramic fuel cells and electrolyser cells, *Solid State Ion.*, **278** (2015) 120–132. <https://doi.org/10.1016/j.ssi.2015.05.014>

86. Samat AA, Darus M, Osman N, Baharuddin NA, Anwar M, A short review on triple conducting oxide cathode materials for proton conducting solid oxide fuel cell, *AIP Conf. Proc.*, **2339(1)** (2021) 020233. <https://doi.org/10.1063/5.0044224>

87. Rasaki SA, Liu C, Lao C, Chen Z, A review of current performance of rare earth metal-doped barium zirconate perovskite: The promising electrode and electrolyte material for the protonic ceramic fuel cells, *Prog. Solid State Chem.*, **63** (2021) 100325. <https://doi.org/10.1016/j.progsolidstchem.2021.100325>

88. Yue Y, Yu S, Gu Y, Bi L, A new Fe-doped $\text{Ca}_3\text{Co}_4\text{O}_9$ cathode for protonic ceramic fuel cells, *Ceram. Int.*, **50** (2024) 40436–40444. <https://doi.org/10.1016/j.ceramint.2024.06.237>

89. Tarutina LR, Vdovin GK, Lyagaeva JG, Medvedev DA, $\text{BaCe}_{0.7-x}\text{Zr}_{0.2}\text{Y}_{0.1}\text{Fe}_x\text{O}_{3-\delta}$ derived from proton-conducting electrolytes: A way of designing chemically compatible cathodes for solid oxide fuel cells, *J. Alloys Compd.*, **831** (2020) 154895. <https://doi.org/10.1016/j.jallcom.2020.154895>

90. Lee J-I, Park K-Y, Park H, Bae H, et al., Triple perovskite structured $\text{Nd}_{1.5}\text{Ba}_{1.5}\text{CoFeMnO}_{9-\delta}$ oxygen electrode materials for highly efficient and stable reversible protonic ceramic cells, *J. Power Sources*, **510** (2021) 230409. <https://doi.org/10.1016/j.jpowsour.2021.230409>

91. Lu L, Liu Y, Zhang H, Xu Y, Chen H, Exploring the potential of triple conducting perovskite cathodes for high-performance solid oxide fuel cells: a comprehensive review, *J. Mater. Chem. A*, **11** (2023) 23613–23639. <https://doi.org/10.1039/D3TA05035A>

92. Choi S, Kucharczyk CJ, Liang Y, Zhang X, et al., Exceptional power density and stability at intermediate temperatures in protonic ceramic fuel cells, *Nat. Energy*, **3** (2018) 202–210. <https://doi.org/10.1038/s41560-017-0085-9>

93. Chen K, Dai H, He S, Bi L, $\text{LaNi}_{0.6}\text{Fe}_{0.4}\text{O}_{3-\delta}$ as a promising cathode for stable proton-conducting solid oxide fuel cells, *Fuel Cells*, **18** (2018) 561–565. <https://doi.org/10.1002/face.201700224>

94. Ding H, Xue X, Liu X, Meng G, High performance protonic ceramic membrane fuel cells (PCMFCs) with $\text{Sm}_{0.5}\text{Sr}_{0.5}\text{CoO}_{3-\delta}$ perovskite cathode, *J. Alloys Compd.*, **494** (2010) 233–235. <https://doi.org/10.1016/j.jallcom.2009.11.180>

95. Yang L, Liu Z, Wang S, Choi Y, et al., A mixed proton, oxygen ion, and electron conducting cathode for SOFCs based on oxide proton conductors, *J. Power Sources*, **195** (2010) 471–474. <https://doi.org/10.1016/j.jpowsour.2009.07.057>

96. Lin Y, Ran R, Zheng Y, Shao Z, et al., Evaluation of $\text{Ba}_{0.5}\text{Sr}_{0.5}\text{Co}_{0.8}\text{Fe}_{0.2}\text{O}_{3-\delta}$ as a potential cathode for anode-supported proton-conducting solid-oxide fuel cell, *J. Power*

- Sources, **180** (2008) 15–22. <https://doi.org/10.1016/j.jpowsour.2008.02.044>
97. Yang S, Wen Y, Zhang J, Lu Y, et al., Electrochemical performance and stability of cobalt-free $Ln_{1.2}Sr_{0.8}NiO_4$ ($Ln = La$ and Pr) air electrodes for proton-conducting reversible solid oxide cells, *Electrochimica Acta*, **267** (2018) 269–277. <https://doi.org/10.1016/j.electacta.2018.02.053>
98. Pikalova E, Kolchugin A, Koroleva M, Vdovin G, et al., Functionality of an oxygen $Ca_3Co_4O_{9+\delta}$ electrode for reversible solid oxide electrochemical cells based on proton-conducting electrolytes, *J. Power Sources*, **438** (2019) 226996. <https://doi.org/10.1016/j.jpowsour.2019.226996>
99. Zhu Z, Tao Z, Bi L, Liu W, Investigation of $SrBaCuCoO_{5+\delta}$ double-perovskite as cathode for proton-conducting solid oxide fuel cells, *Mater. Res. Bull.*, **45** (2010) 1771–1774. <https://doi.org/10.1016/j.materresbull.2010.06.059>
100. He W, Yuan R, Dong F, Wu X, Ni M, High performance of protonic solid oxide fuel cell with $BaCo_{0.7}Fe_{0.22}Sc_{0.08}O_{3-\delta}$ electrode, *Int. J. Hydrog. Energy*, **42** (2017) 25021–25025. <https://doi.org/10.1016/j.ijhydene.2017.08.107>
101. Shan D, Gong Z, Wu Y, Miao L, et al., A novel $BaCe_{0.5}Fe_{0.3}Bi_{0.2}O_{3-\delta}$ perovskite-type cathode for proton-conducting solid oxide fuel cells, *Ceram. Int.*, **43** (2017) 3660–3663. <https://doi.org/10.1016/j.ceramint.2016.11.206>
102. Ren R, Wang Z, Xu C, Sun W, et al., Tuning the defects of the triple conducting oxide $BaCo_{0.4}Fe_{0.4}Zr_{0.1}Y_{0.1}O_{3-\delta}$ perovskite toward enhanced cathode activity of protonic ceramic fuel cells, *J. Mater. Chem. A*, **7** (2019) 18365–18372. <https://doi.org/10.1039/C9TA04335G>
103. Wu Y, Li K, Yang Y, Song W, et al., Investigation of Fe-substituted in $BaZr_{0.8}Y_{0.2}O_{3-\delta}$ proton conducting oxides as cathode materials for protonic ceramics fuel cells, *J. Alloys Compd.*, **814** (2020) 152220. <https://doi.org/10.1016/j.jallcom.2019.152220>
104. Osinkin D, Tropin E, Hydrogen production from methane and carbon dioxide mixture using all-solid-state electrochemical cell based on a proton-conducting membrane and redox-robust composite electrodes, *J. Energy Chem.*, **69** (2022) 576–584. <https://doi.org/10.1016/j.jechem.2022.02.019>
105. Loureiro FJA, Ramasamy D, Mikhalev SM, Shaula AL, et al., $La_4Ni_3O_{10\pm\delta}$ - $BaCe_{0.9}Y_{0.1}O_{3-\delta}$ cathodes for proton ceramic fuel cells; short-circuiting analysis using $BaCe_{0.9}Y_{0.1}O_{3-\delta}$ symmetric cells, *Int. J. Hydrog. Energy*, **46** (2021) 13594–13605. <https://doi.org/10.1016/j.ijhydene.2020.06.243>
106. Jing J, Lei Z, Zheng Z, Wang H, et al., Tuning the oxygen vacancy of the $Ba_{0.95}La_{0.05}FeO_{3-\delta}$ perovskite toward enhanced cathode activity for protonic ceramic fuel cells, *International Journal of Hydrogen Energy*, **47(83)** (2022) 35449–35457. <https://doi.org/10.1016/j.ijhydene.2022.08.118>
107. Lyagaeva J, Medvedev D, Pikalova E, Plaksin S, et al., A detailed analysis of thermal and chemical compatibility of cathode materials suitable for $BaCe_{0.8}Y_{0.2}O_{3-\delta}$ and $BaZr_{0.8}Y_{0.2}O_{3-\delta}$ proton electrolytes for solid oxide fuel cell application, *Int. J. Hydrog. Energy*, **42** (2017) 1715–1723. <https://doi.org/10.1016/j.ijhydene.2016.07.248>
108. Sun W, Shi Z, Fang S, Yan L, et al., A high performance $BaZr_{0.1}Ce_{0.7}Y_{0.2}O_{3-\delta}$ -based solid oxide fuel cell with a cobalt-free $Ba_{0.5}Sr_{0.5}FeO_{3-\delta}$ - $Ce_{0.8}Sm_{0.2}O_{2-\delta}$ composite cathode, *Int. J. Hydrog. Energy*, **35** (2010) 7925–7929. <https://doi.org/10.1016/j.ijhydene.2010.05.084>
109. Xie D, Ling A, Yan D, Jia L, et al., A comparative study on the composite cathodes with proton conductor and oxygen ion conductor for proton-conducting solid oxide fuel cell, *Electrochimica Acta*, **344** (2020) 136143. <https://doi.org/10.1016/j.electacta.2020.136143>
110. Antonova EP, Kolchugin AA, Pikalova EYu, Medvedev DA, Bogdanovich NM, Development of electrochemically active electrodes for $BaCe_{0.89}Gd_{0.1}Cu_{0.01}O_{3-\delta}$ proton conducting electrolyte, *Solid State Ion.*, **306** (2017) 55–61. <https://doi.org/10.1016/j.ssi.2017.02.001>
111. Pikalova EYu, Bogdanovich NM, Kuz'min AV, Composite electrodes for proton conducting electrolyte of $CaZr_{0.95}Sc_{0.05}O_{3-\delta}$, *Russ. J. Electrochem.*, **53** (2017) 752–760. <https://doi.org/10.1134/S1023193517070096>
112. Osinkin DA, Electrochemical behaviour of redox-robust electrode in contact with protonic electrolyte: Case of double-layered $Sr_2Fe_{1.5}Mo_{0.5}O_{6-\delta}$ - $Ce_{0.8}Sm_{0.2}O_{2-\delta}$ composite, *Int. J. Hydrog. Energy*, **77** (2024) 1066–1073. <https://doi.org/10.1016/j.ijhydene.2024.06.266>
113. Chen D, Zhang Q, Lu L, Periasamy V, et al., Multi scale and physics models for intermediate and low temperatures H^+ -solid oxide fuel cells with $H^+/e^-/O^{2-}$ mixed conducting properties: Part A, generalized percolation theory for LSCF-SDC-BZCY 3-component cathodes, *J. Power Sources*, **303** (2016) 305–316. <https://doi.org/10.1016/j.jpowsour.2015.10.090>
114. Li G, Zhang Y, Ling Y, He B, et al., Probing novel triple phase conducting composite cathode for high performance protonic ceramic fuel cells, *J. Hydrog. Energy*, **41** (2016) 5074–5083. <https://doi.org/10.1016/j.ijhydene.2016.01.068>
115. Bu Y, Joo S, Zhang Y, Wang Y, et al., A highly efficient composite cathode for proton-conducting solid oxide fuel cells, *J. Power Sources*, **451** (2020) 227812. <https://doi.org/10.1016/j.jpowsour.2020.227812>
116. Kalinina EG, Pikalova EYu, New trends in the development of electrophoretic deposition method in the solid oxide fuel cell technology: theoretical approaches, experimental solutions and development prospects, *Russ. Chem. Rev.*, **88** (2019) 1179–1219. <https://doi.org/10.1070/RCR4889>
117. Dos Santos-Gómez L, Zamudio-García J, Caizán-Juanarena L, Porrás-Vázquez JM, Marrero-López D, Design and optimization of self-assembled nanocomposite electrodes for SOFCs, *J. Power Sources*, **613** (2024) 234866. <https://doi.org/10.1016/j.jpowsour.2024.234866>
118. Shimada H, Yamaguchi T, Kishimoto H, Sumi H, et al., Nanocomposite electrodes for high current density over $3 A \cdot cm^{-2}$ in solid oxide electrolysis cells, *Nat. Commun.*, **10** (2019) 5432. <https://doi.org/10.1038/s41467-019-13426-5>
119. Stangl A, Riaz A, Rapenne L, Caicedo JM, et al., Tailored nano-columnar La_2NiO_4 cathodes for improved electrode performance, *J. Mater. Chem. A*, **10** (2022) 2528–2540. <https://doi.org/10.1039/D1TA09110G>
120. Pikalova EYu, Kalinina EG, Solid oxide fuel cells based on ceramic membranes with mixed conductivity: improving efficiency, *Russ. Chem. Rev.*, **90** (2021) 703–749. <https://doi.org/10.1070/RCR4966>
121. Bieberle-Hütter A, Tuller HL, Fabrication and structural characterization of interdigitated thin film $La_{1-x}Sr_xCoO_3$ (LSCO) electrodes, *J. Electroceramics*, **16** (2006) 151–157. <https://doi.org/10.1007/s10832-006-5945-9>
122. Kan WH, Samson AJ, Thangadurai V, Trends in electrode development for next generation solid oxide fuel cells,

- J. Mater. Chem. A, **4** (2016) 17913–17932. <https://doi.org/10.1039/C6TA06757C>
123. Lei L, Tao Z, Hong T, Wang X, Chen F, A highly active hybrid catalyst modified $(La_{0.60}Sr_{0.40})_{0.95}Co_{0.20}Fe_{0.80}O_{3-\delta}$ cathode for proton conducting solid oxide fuel cells, J. Power Sources, **389** (2018) 1–7. <https://doi.org/10.1016/j.jpowsour.2018.03.058>
124. Zhao F, Liu Q, Wang S, Chen F, Infiltrated multiscale porous cathode for proton-conducting solid oxide fuel cells, J. Power Sources, **196** (2011) 8544–8548. <https://doi.org/10.1016/j.jpowsour.2011.06.029>
125. Wu T, Zhao Y, Peng R, Xia C, Nano-sized $Sr_{0.5}Co_{0.5}O_{3-\delta}$ as the cathode for solid oxide fuel cells with proton-conducting electrolytes of $BaCe_{0.8}Sm_{0.2}O_{2.9}$, Electrochimica Acta, **54** (2009) 4888–4892. <https://doi.org/10.1016/j.electacta.2009.04.013>
126. Ricote S, Bonanos N, Lenrick F, Wallenberg R, $LaCoO_3$: Promising cathode material for protonic ceramic fuel cells based on a $BaCe_{0.2}Zr_{0.7}Y_{0.1}O_{3-\delta}$ electrolyte, J. Power Sources, **218** (2012) 313–319. <https://doi.org/10.1016/j.jpowsour.2012.06.098>
127. Ricote S, Bonanos N, Rørvik PM, Haavik C, Microstructure and performance of $La_{0.58}Sr_{0.4}Co_{0.2}Fe_{0.8}O_{3-\delta}$ cathodes deposited on $BaCe_{0.2}Zr_{0.7}Y_{0.1}O_{3-\delta}$ by infiltration and spray pyrolysis, J. Power Sources, **209** (2012) 172–179. <https://doi.org/10.1016/j.jpowsour.2012.02.090>
128. Da'as EH, Bi L, Bouffrad S, Traversa E, Nanostructuring the electronic conducting $La_{0.8}Sr_{0.2}MnO_{3-\delta}$ cathode for high-performance in proton-conducting solid oxide fuel cells below 600 °C, Sci. China Mater., **61** (2018) 57–64. <https://doi.org/10.1007/s40843-017-9125-1>
129. Tomov RI, Duncan R, Krauz M, Vasant Kumar R, Glowacki BA. Inkjet printing and inkjet infiltration of functional coatings for SOFCs fabrication. 3rd International Congress on Energy Efficiency and Energy Related Materials (ENEFM2015). Springer Proceedings in Energy. Springer: Cham; **10** (2016). <https://doi.org/10.1051/e3sconf/20161000098>
130. Li G, Jin H, Cui Y, Gui L, et al., Application of a novel $(Pr_{0.9}La_{0.1})_2(Ni_{0.74}Cu_{0.2}Nb_{0.05})O_{4+\delta}$ -infiltrated $BaZr_{0.1}Ce_{0.7}Y_{0.2}O_{3-\delta}$ cathode for high performance protonic ceramic fuel cells, J. Power Sources, **341** (2017) 192–198. <https://doi.org/10.1016/j.jpowsour.2016.11.008>
131. Liu B, Jia L, Chi B, Pu J, Li J, A novel $PrBaCo_2O_{5+\delta}$ - $BaZr_{0.1}Ce_{0.7}Y_{0.1}Yb_{0.1}O_3$ composite cathode for proton-conducting solid oxide fuel cells, Compos. Part B Eng., **191** (2020) 107936. <https://doi.org/10.1016/j.compositesb.2020.107936>
132. Shimada H, Yamaguchi Y, Sumi H, Mizutani Y, Enhanced $La_{0.8}Sr_{0.4}Co_{0.2}Fe_{0.8}O_{3-\delta}$ -based cathode performance by modification of $BaZr_{0.1}Ce_{0.7}Y_{0.1}Yb_{0.1}O_{3-\delta}$ electrolyte surface in protonic ceramic fuel cells, Ceram. Int., **47** (2021) 16358–16362. <https://doi.org/10.1016/j.ceramint.2021.02.123>
133. Ye X-F, Wen YB, Yang SJ, Lu Y, et al., Study of $CaZr_{0.9}In_{0.1}O_{3-\delta}$ based reversible solid oxide cells with tubular electrode supported structure, Int. J. Hydrog. Energy, **42** (2017) 23189–23197. <https://doi.org/10.1016/j.ijhydene.2017.07.195>
134. Zvonareva IA, Starostin GN, Akopian MT, Murashkina AA, et al., Thermal and chemical expansion behavior of hydrated barium stannate materials, Ceram. Int., **49** (2023) 21923–21931. <https://doi.org/10.1016/j.ceramint.2023.04.016>
135. Starostin GN, Tsvetkov DS, Starostina IA, Sereda VV, et al., Fundamental and technological aspects of thermochemical expansion of proton-conducting oxides: a case study of $BaSn_{1-x}Sc_xO_{3-\delta}$, J. Mater. Chem. A, **12** (2024) 14022–14034. <https://doi.org/10.1039/D4TA02402H>
136. Lyagaeva J, Antonov B, Dunyushkina L, Kuimov V, et al., Acceptor doping effects on microstructure, thermal and electrical properties of proton-conducting $BaCe_{0.5}Zr_{0.3}Ln_{0.2}O_{3-\delta}$ ($Ln = Yb, Gd, Sm, Nd, La$ or Y) ceramics for solid oxide fuel cell applications, Electrochimica Acta, **192** (2016) 80–88. <https://doi.org/10.1016/j.electacta.2016.01.144>
137. Dunyushkina LA, Belyakov SA, Filatov NM, Proton-conducting alkaline earth hafnates: A review of manufacturing technologies, physicochemical properties and electrochemical performance, J. Eur. Ceram. Soc., **43** (2023) 6681–6698. <https://doi.org/10.1016/j.jeurceramsoc.2023.07.011>
138. Dayaghi AM, Haugrud R, Stange M, Larring Y, et al., Increasing the thermal expansion of proton conducting Y-doped $BaZrO_3$ by Sr and Ce substitution, Solid State Ion., **359** (2021) 115534. <https://doi.org/10.1016/j.ssi.2020.115534>
139. Babiniec SM, Ricote S, Sullivan NP, Infiltrated lanthanum nickelate cathodes for use with $BaCe_{0.2}Zr_{0.7}Y_{0.1}O_{3-\delta}$ proton conducting electrolytes, J. Electrochem. Soc., **161** (2014) F717–F723. <https://doi.org/10.1149/2.037406jes>
140. Sadykov VA, Pikalova EYu, Kolchugin AA, Fetisov AV, et al., Transport properties of Ca-doped $LmNiO_4$ for intermediate temperature solid oxide fuel cells cathodes and catalytic membranes for hydrogen production, Int. J. Hydrog. Energy, **45** (2020) 13625–13642. <https://doi.org/10.1016/j.ijhydene.2018.03.039>
141. Sun C, Yang S, Lu Y, Wen J, et al., Tailoring a micro-nanostructured electrolyte-oxygen electrode interface for proton-conducting reversible solid oxide cells, J. Power Sources, **449** (2020) 227498. <https://doi.org/10.1016/j.jpowsour.2019.227498>
142. Kim J-H, Manthiram A, Layered $LmBaCo_2O_{5+\delta}$ perovskite cathodes for solid oxide fuel cells: an overview and perspective, J. Mater. Chem. A, **3** (2015) 24195–24210. <https://doi.org/10.1039/C5TA06212H>
143. Wang X, Ma Z, Zhang T, Kang J, et al., Charge-transfer modeling and polarization DRT analysis of proton ceramics fuel cells based on mixed conductive electrolyte with the modified anode–electrolyte interface, ACS Appl. Mater. Interfaces, **10** (2018) 35047–35059. <https://doi.org/10.1021/acsami.8b10429>
144. Bi L, Shafi SP, Da'as EH, Traversa E, Tailoring the cathode–electrolyte interface with nanoparticles for boosting the solid oxide fuel cell performance of chemically stable proton-conducting electrolytes, Small, **14** (2018) 1801231. <https://doi.org/10.1002/smll.201801231>
145. Sun W, Yan L, Shi Z, Zhu Z, Liu W, Fabrication and performance of a proton-conducting solid oxide fuel cell based on a thin $BaZr_{0.8}Y_{0.2}O_{3-\delta}$ electrolyte membrane, J. Power Sources, **195** (2010) 4727–4730. <https://doi.org/10.1016/j.jpowsour.2010.02.012>
146. Yang L, Zuo C, Wang S, Cheng Z, Liu M, A novel composite cathode for low-temperature SOFCs based on oxide proton conductors, Adv. Mater., **20** (2008) 3280–3283. <https://doi.org/10.1002/adma.200702762>
147. Bae H, Choi GM, Novel modification of anode microstructure for proton-conducting solid oxide fuel cells with

- BaZr_{0.8}Y_{0.2}O_{3-δ} electrolytes, *J. Power Sources*, **285** (2015) 431–438. <https://doi.org/10.1016/j.jpowsour.2015.03.090>
148. Torabi A, Hanifi AR, Etsell TH, Sarkar P, Effects of porous support microstructure on performance of infiltrated electrodes in solid oxide fuel cells, *Electrochem. Soc.*, **159** (2011) B201–B210. <https://doi.org/10.1149/2.068202jes>
149. Yildirim F, Timurkutluk C, Timurkutluk B, Investigation and optimization of infiltration parameters for nanostructured cathode electrodes in solid oxide fuel cells, *Int. J. Hydrog. Energy*, **114** (2025) 172–185. <https://doi.org/10.1016/j.ijhydene.2025.03.013>
150. Cable TL, Sofie SW, A symmetrical, planar SOFC design for NASA's high specific power density requirements, *J. Power Sources*, **174** (2007) 221–227. <https://doi.org/10.1016/j.jpowsour.2007.08.110>
151. Zhi M, Mariani N, Gemmen R, Gerdes K, Wu N, Nanofiber scaffold for cathode of solid oxide fuel cell, *Energy Env. Sci*, **4** (2011) 417–420. <https://doi.org/10.1039/COEE00358A>
152. Strandbakke R, Vøllestad E, Robinson SA, Fontaine M-L, Norby T, Ba_{0.5}Gd_{0.8}La_{0.7}Co₂O_{6-δ} infiltrated in porous BaZr_{0.7}Ce_{0.2}Y_{0.1}O₃ backbones as electrode material for proton ceramic electrolytes, *J. Electrochem. Soc.*, **164** (2017) F196–F202. <https://doi.org/10.1149/2.0141704jes>
153. Shin E-K, Anggia E, Parveen AS, Park J-S, Optimization of the protonic ceramic composition in composite electrodes for high-performance protonic ceramic fuel cells, *Int. J. Hydrog. Energy*, **44** (2019) 31323–31332. <https://doi.org/10.1016/j.ijhydene.2019.09.247>
154. Tang H, Jin Z, Wu Y, Liu W, Bi L, Cobalt-free nanofiber cathodes for proton conducting solid oxide fuel cells, *Electrochem. Commun.*, **100** (2019) 108–112. <https://doi.org/10.1016/j.elecom.2019.01.022>
155. Ding H, Wu W, Jiang C, Ding Y, et al., Self-sustainable protonic ceramic electrochemical cells using a triple conducting electrode for hydrogen and power production, *Nat. Commun.*, **11** (2020) 1907. <https://doi.org/10.1038/s41467-020-15677-z>
156. Gondolini A, Mercadelli E, Casadio S, Sanson A, Freeze cast support for hydrogen separation membrane, *J. Eur. Ceram. Soc.*, **42** (2022) 1053–1060. <https://doi.org/10.1016/j.jeurceramsoc.2021.10.063>
157. Saqib M, Lee J-I, Shin J-S, Park K, et al., Modification of oxygen-ionic transport barrier of BaCo_{0.4}Zr_{0.1}Fe_{0.4}Y_{0.1}O₃ steam (air) electrode by impregnating samarium-doped ceria nanoparticles for proton-conducting reversible solid oxide cells, *J. Electrochem. Soc.*, **166** (2019) F746–F754. <https://doi.org/10.1149/2.0461912jes>
158. Solís C, Navarrete L, Bozza F, Bonanos N, Serra JM, Catalytic surface promotion of composite cathodes in protonic ceramic fuel cells, *ChemElectroChem*, **2** (2015) 1106–1110. <https://doi.org/10.1002/celec.201500068>
159. Choi J, Shin M, Kim B, Park J-S, High-performance ceramic composite electrodes for electrochemical hydrogen pump using protonic ceramics, *Int. J. Hydrog. Energy*, **42** (2017) 13092–13098. <https://doi.org/10.1016/j.ijhydene.2017.04.061>
160. Papac M, Stevanović V, Zakutayev A, O'Hayre R, Triple ionic–electronic conducting oxides for next-generation electrochemical devices, *Nat. Mater.*, **20** (2021) 301–313. <https://doi.org/10.1038/s41563-020-00854-8>
161. Hwang SH, Kim SK, Nam J-T, Park J-S, Triple-component composite cathode for performance optimization of protonic ceramic fuel cells, *Int. J. Hydrog. Energy*, **46** (2021) 33551–33560. <https://doi.org/10.1016/j.ijhydene.2021.07.179>
162. Jing J, Lei Z, Wang C, Zheng Z, et al., Boosting performance of a protonic ceramic fuel cell by the incorporation of active nano-structured layers, *Chem. Eng.*, **11** (2023) 10303–10310. <https://doi.org/10.1021/acssuschemeng.3c00706>
163. Xia Y, Xu X, Teng Y, Lv H, et al., A novel BaFe_{0.8}Zn_{0.1}Bi_{0.1}O_{3-δ} cathode for proton conducting solid oxide fuel cells, *Ceram. Int.*, **46** (2020) 25453–25459. <https://doi.org/10.1016/j.ceramint.2020.07.015>
164. Chen C, Wang Z, Miao X, Sun C, et al., Cycling performance and interface stability research of tubular protonic reversible solid oxide cells with air electrodes by different manufacturing processes, *Electrochem. Commun.*, **151** (2023) 107507. <https://doi.org/10.1016/j.elecom.2023.107507>
165. Wang Q, Tong X, Ricote S, Sažinas R, et al., Nano-LaCoO₃ infiltrated BaZr_{0.8}Y_{0.2}O_{3-δ} electrodes for steam splitting in protonic ceramic electrolysis cells, *Adv. Powder Mater.*, **1** (2022) 100003. <https://doi.org/10.1016/j.apmate.2021.09.003>
166. Kiebach R, Knöfel C, Bozza F, Klemensø T, Chatzichristodoulou C, Infiltration of ionic-, electronic- and mixed-conducting nano particles into La_{0.75}Sr_{0.25}MnO_{3-δ}-Y_{0.16}Zr_{0.84}O₂ cathodes – A comparative study of performance enhancement and stability at different temperatures, *J. Power Sources*, **228** (2013) 170–177. <https://doi.org/10.1016/j.jpowsour.2012.11.070>
167. Kiebach R, Zielke P, Veltzé S, Ovtar S, et al., On the properties and long-term stability of infiltrated lanthanum cobalt nickelates (LCN) in solid oxide fuel cell cathodes, *J. Electrochem. Soc.*, **164** (2017) F748–F758. <https://doi.org/10.1149/2.0361707jes>
168. Liu Y, Guo Y, Ran R, Shao Z, A novel approach for substantially improving the sinterability of BaZr_{0.4}Ce_{0.4}Y_{0.2}O_{3-δ} electrolyte for fuel cells by impregnating the green membrane with zinc nitrate as a sintering aid, *J. Membr. Sci.*, **437** (2013) 189–195. <https://doi.org/10.1016/j.memsci.2013.03.002>
169. Lacz A, Pasierb P, Electrical properties and chemical stability of BaCe_{0.9}Y_{0.1}O₃-BaWO₄ composites synthesized by co-sintering and impregnation method, *Solid State Ion.*, **302** (2017) 152–157. <https://doi.org/10.1016/j.ssi.2016.12.006>
170. Huang W-C, Chen T-C, Chang H-Y, Single composite electrolyte prepared by infiltration and characterization, *Int. J. Hydrog. Energy*, **107** (2025) 666–678. <https://doi.org/10.1016/j.ijhydene.2024.04.090>
171. Amiri S, Paydar MH, Effect of pore formers characteristics and melt infiltration parameters on microstructure and electrical properties of BaCe_{0.7}Zr_{0.1}Y_{0.2}O_{3-δ}-carbonate composite electrolyte, *J. Alloys Compd.*, **735** (2018) 172–183. <https://doi.org/10.1016/j.jallcom.2017.11.067>